University of Alberta

The influence of mantle metasomatism on the oxidation state of the lithospheric mantle

by

Steven Creighton

A thesis submitted to the Faculty of Graduate Studies and Research
in partial fulfillment of the requirements for the degree of

Doctor of Philosopy
in
Geology

Department of Earth and Atmospheric Sciences

©Steven Creighton
Fall 2009
Edmonton, Alberta

Permission is hereby granted to the University of Alberta Libraries to reproduce single copies of this thesis and to lend or sell such copies for private, scholarly or scientific research purposes only. Where the thesis is converted to, or otherwise made available in digital form, the University of Alberta will advise potential users of the thesis of these terms.

The author reserves all other publication and other rights in association with the copyright in the thesis and, except as herein before provided, neither the thesis nor any substantial portion thereof may be printed or otherwise reproduced in any material form whatsoever without the author's prior written permission.

Examining Committee

Thomas Stachel, Earth and Atmospheric Sciences

Robert W. Luth, Earth and Atmospheric Sciences

Thomas Chacko, Earth and Atmospheric Sciences

Sergei Matveev, Earth and Atmospheric Sciences

Christopher D. Herd, Earth and Atmospheric Sciences

Ron Cavell, Chemistry

Cliff Shaw, Geology, University of New Brunswick

Dedication

For Kelvin, Jordan, Tove and Kadi. This is what I was doing all those years in school.

Abstract

The oxidation state, reflected in the oxygen fugacity (fO_2), of the lithospheric mantle is both laterally and vertically heterogeneous. Depth-fO_2 profiles from kimberlite-borne peridotitic mantle xenoliths from the Bultfontein kimberlite, Kimberley, South Africa and the A154-N and A154-S kimberlites of the Diavik Mine, NWT, Canada were constructed by measuring ferric iron concentrations in garnets using the flank method. These data demonstrate that mantle metasomatic re-enrichment processes had a significant effect on fO_2. In the garnet stability field, the Kaapvaal lithospheric mantle becomes progressively more reducing with increasing depth from $\Delta\log fO_2$ (FMQ) of -2 at 110 km to -4 at 210 km. The lithospheric mantle beneath Diavik is vertically layered with respect to its bulk and trace-element composition. The shallow 'ultradepleted' layer is oxidized, to the point that carbonate rather than graphite is the anticipated carbon host. The deeper layer is more fertile and has fO_2 conditions extending down to $\Delta\log fO_2$ (FMQ) -3.8.

Deviations from predicted depth-fO_2 trends in both xenolith localities result from metasomatic re-enrichment caused by transient fluids and melts. Diamond formation in the Kaapvaal lithospheric mantle may have occurred through the infiltration of reduced fluids into relatively more oxidized mantle. Trace-element concentrations in garnets preserve evidence of two distinct melt metasomatic enrichment events. One was a craton-wide event that is commonly observed in garnet peridotite xenoliths and xenocrysts worldwide; the other was melt infiltration event, preserved as MARID xenoliths, related to the eruption of the Group 2 kimberlites in the western portion of the Kaapvaal craton. The effect of the former melt metasomatism on fO_2 is unclear ambiguous whereas the MARID event was clearly oxidizing.

Diavik xenoliths preserve evidence for events similar to the fluid and 'common' melt metasomatism seen in the Bultfontein samples. Fluid metasomatism affected the entire depth range of xenoliths sampled from Diavik and was oxidizing. A stage of melt metasomatism affected only the deeper (>140 km) portion of the lithospheric mantle and

had an overall reducing effect. The observation of sharp-edged octahedral diamonds in microxenoliths affected by the fluid metasomatic event may indicate that this was a major diamond-forming event in the mantle beneath Diavik.

Acknowledgements

I wish to thank my supervisors Thomas Stachel and Bob Luth for the many years of friendship, advice and guidance. I am grateful to Ralf Tappert, Anetta Banas, Lucy Hunt, Greg Melton and my other collegues in diamond research at the U of A for many, many hours of discussion, some of which was about our research projects. I also would like to acknowledge Heidi Höfer for her pioneering work developing the flank method and for her encouragment to modify it for truly quantitative measurements in mantle minerals. Sergei Matveev is also gratefully acknowledged for his considerable help with all things related to the electron microprobe beginning with teaching me how to operate it as an undergraduate student. My thanks to Tony Simonetti and GuangCheng Chen for assistance with LA-ICPMS analyses.

The project outlined in Chapter 2 would not have been possible without the careful collection of diamondiferous microxenoliths by Ray (Ramon) Ferraris and Delene Daniels (Production Splitting Facility of Diavik Diamond Mines). Samples for the other two projects were kindly provided with assistance of Dr. Jock Robey and De Beers Consolidated Mines (Chapter 3) and Sean Whiteford, Dave Eichenberg, Hayley McLean and the geology team at Diavik (Chapter 4).

Financial support for research costs was jointly provided by NSERC and Diavik Diamond Mines in the form of a CRD grant. I was the grateful recipient of NSERC PGS-M and PGS-D scholarships and financial support from the EAS department as a teaching assistant and other scholarships including the C.M. Scarfe award. Other scholarships and awards from the University of Alberta and other organizations are also gratefully acknowledged.

Finally, I would like to acknowledge the patience of my wife, Leah, who discovered that marrying a student is akin to taking a vow of poverty.

Table of Contents

List of Tables

List of Figures

List of Symbols and Abbreviations

%B	Expresses the proportion of nitrogen aggregated into B centres in diamond
°C	Degrees Celsius
cf.	Confer (offer for comparison)
CITZAF	A matrix correction program for electron microprobe data
cm	Centimetre
Cr-number	Molar ratio of Cr/(Cr+Al)
$\Delta \log fO_2$ (FMQ)	Oxygen fugacity expressed relative to the fayalite-magnetite-quartz buffering reaction
$\delta^{13}C$	Carbon isotope composition expressed relative to a known standard
EMOD/G	The enstatite-magnesite-olivine-diamond/graphite oxygen buffer
EPMA	Electron probe microanalysis
$Fe^{3+}/\Sigma Fe$	Ratio of ferric to total iron (molar basis)
fO_2	Oxygen fugacity
FTIR	Fourier transform infrared spectroscopy
G9	Classification for mantle-derived, Mg- and Ca-rich garnets
G10	Classification for mantle-derived, Mg-rich and Ca-poor garnets.
G10D	Subtype of G10 garnet where "D" denotes derivation a stronger probability of the garnet originating from the diamond stability field based primarily on higher Cr_2O_3 concentrations.
G11	Classifcation for mantle-derived, high-Ti, Mg- and Ca-rich garnets
Ga	Billions of years ago
GPa	Gigapascal
HFSE	High field strength elements
HREE	Heavy rare earth elements
ICP-MS	Inductively coupled plasma mass spectrometer
IW	The iron-wüstite oxygen buffering reaction
km	Kilometres
kV	Kilovolt
LREE	Light rare earth elements
Lα	X-Ray emission arising from electron transfer from M to L shells
Lβ	X-Ray emission arising from electron transfer from N to L shells
Ma	Millions of years ago
MARID	A type of melt metasomatic overprint observed in some xenoliths from South African kimberlites. The acronym refers to Mica (phlogopite), Amphibole (K-richterite), Rutile, Ilmenite, Diopside (not refering strictly to the end-member composition).
Mg-Number	Molar ratio of Mg/(Mg+Fe)
MREE	Middle rare earth elements
μm	Micron
mW/m^2	Milliwatts per metre-squared (unit of heat flow)
nA	Nanoampere
NNO	The nickel-nickel oxide oxygen buffering reaction
NWT	Northwest Territories

ppm	Concentration expressed in parts per million
R^2	Correlation coefficient
REE	Rare earth elements (subscript 'N' indicates normalized values)
σ	(Lower case Greek sigma) error expressed as 1 standard deviation from the mean
Type IaA	Nitrogen aggregated in diamond in A centres
Type IaAB	Nitrogen aggregated in diamond in both A and B centres
Type IaB	Nitrogen aggregated in diamond in B centres
V-PDB	Vienna PeeDee Belemnite carbon isotope standard
wt%	Concentration in weight percent
X_a	Mole fraction of component *a* in phase *X*

Chapter 1: Introduction

Decades of research have led to a detailed understanding of the source composition and crystal growth mechanisms of diamonds. However, the chemical process of natural diamond formation is still unresolved. Studies on mineral and fluid inclusions in diamonds point towards diamond precipitation from mantle-derived fluids or melts percolating upwards through the mantle lithosphere (e.g. Haggerty 1986; Navon et al. 1988). But what is the redox character of these fluids? Is diamond formed through oxidation of methane bearing fluids that penetrate into a more oxidizing lithosphere or does the opposite take place, reduction of carbonate-bearing fluids in contact with reducing lithospheric peridotite? A clear understanding of the oxidation state of mantle peridotite brought to the Earth's surface in kimberlites as xenoliths will allow constraint of the redox conditions of the lithospheric mantle both during diamond formation and at the time of kimberlite eruption.

The term 'lithosphere' refers to the outermost layer of the Earth including the crust and the rigid portion of the upper mantle characterized by conductive heat flow. The lithosphere is a thermal, chemical and mechanical boundary layer within the Earth. The lithospheric mantle acts as an effective insulating layer protecting the crust from the hotter convecting asthenospheric mantle and filters melts and other fluids rising from deeper within the mantle. Geophysical and petrological studies suggest that the lithosphere beneath the continental crust is thicker and colder than the lithosphere beneath the oceanic crust (Jordan 1978; Boyd 1989). The subcratonic lithospheric mantle is that portion of the lithosphere that underlies the ancient (>2.5 Ga) nuclei of continents called cratons.

Previous studies of spinel-bearing peridotite xenoliths have shown that the shallow lithospheric mantle is heterogeneous in oxidation state with variations related to tectonic setting, differing degrees of depletion caused by melt extraction, and metasomatism (e.g. Ballhaus et al. 1993; Woodland et al. 2006). Studies on garnet-bearing xenoliths from kimberlites have shown that similar levels of heterogeneity exist within the deeper portions

of the lithsopheric mantle (e.g. Luth et al. 1990; Woodland and Koch 2003; McCammon and Kopylova 2004). A single study of samples from the Wesselton kimberlite (Kimberley area, South Africa) has shown that some of this heterogeneity is the result of interaction with metasomatic melts (McCammon et al. 2001). Application of the flank method (Höfer and Brey 2007) modified specifically for measuring ferric iron in mantle-derived pyropic garnets (Appendix A) and LA-ICPMS provide the first ever coupled in situ ferric iron and trace-element measurements from the same garnet. The trace-element composition of the garnets reveals the type of metasomatism that affected their host rocks and the ferric iron measurements constrain the redox effects of the metasomatic fluids and melts. With constraint on the redox effect of infiltrating fluids and melts, we can better understand the processes that formed and destroyed diamond in the lithospheric mantle.

This study focuses mantle-derived xenoliths from two key diamond mining centres: the Kimberley region of the Kaapvaal craton (Bultfontein mine), South Africa and the central Slave craton (Diavik mine), in northern Canada. A brief overview of the crustal geology and mantle petrology of the Kaapvaal and Slave cratons follows in the next two sections.

1.1. Kaapvaal craton

1.1.1. Crustal geology

The Kaapvaal craton is one of the best preserved Archean granite-greenstone terranes worldwide. The exposed crustal geology and lithospheric mantle – sampled as xenoliths in kimberlites – have been the focus of extensive study. In many respects, the Kaapvaal craton has been considered the "type" Archean craton. The following brief overview of the geological history of the Kaapvaal craton is not comprehensive but attempts to highlight key events that may relate to the overall formation of the craton. de Wit et al. (1992) and Poujol et al. (2003) have provided comprehensive reviews of the geochronological data related to the formation and evolution of the Kaapvaal craton. Much of the following

overview comes from their compilations.

The oldest rocks known from the Kaapvaal craton are found in the Ancient Gneiss Complex (3644 Ma) in the eastern portion of the craton (see the appendices of Poujol et al. 2003 for references on age data) and the Barberton greenstone belt (3570 Ma) in the eastern terrane (the terranes referred to here are the geographical boundaries defined by Poujol et al. 2003 and are not meant to imply tectonic boundaries). Zircon xenocrysts as old as 3.7 Ga have been found, indicating an input from old source rocks that may have become completely eroded. Between ~3200 and 3170 Ma, there was significant emplacement of granitoid rocks in the western, central and northern terranes. Subsequent to this was the first period of craton-wide igneous activity between 3110 and 2970 Ma, including initiation of volcanism of the Murchison greenstone belt in the northern terrane. This period of widespread igneous activity may indicate the time of consolidation of separate proto-continental and arc fragments into the Kaapvaal craton. Subsequently, the north and west terranes had numerous plutons emplaced between 2880 and 2820 Ma whereas the east and central terranes are marked by a period of relative quiescence. Finally, there was another pulse of craton-wide magmatic activity at 2750 to 2700 Ma.

1.1.2. Petrology of the Kaapvaal lithospheric mantle

Samples of the mantle are available as mineral inclusions in diamonds, xenoliths and xenocrysts. The relative scarcity of silicate inclusions in diamonds and of mantle-derived xenoliths limit their usefulness in providing overviews of the lithospheric mantle from large geographical regions. Garnet xenocrysts are much more abundant and available from more kimberlites than xenoliths. Although the equilibrium pressure and temperature of garnet xenocrysts cannot be constained as precisely as for xenoliths, the composition of xenocryst garnets can provide information about the mantle over a wider geographical range and on a statistically sounder basis than what is available from xenoliths studies alone (e.g. Griffin et al. 1999). The majority of well studied xenolith localities in the Kaapvaal craton are in the south-west whereas garnet xenocrysts are available from the entire craton.

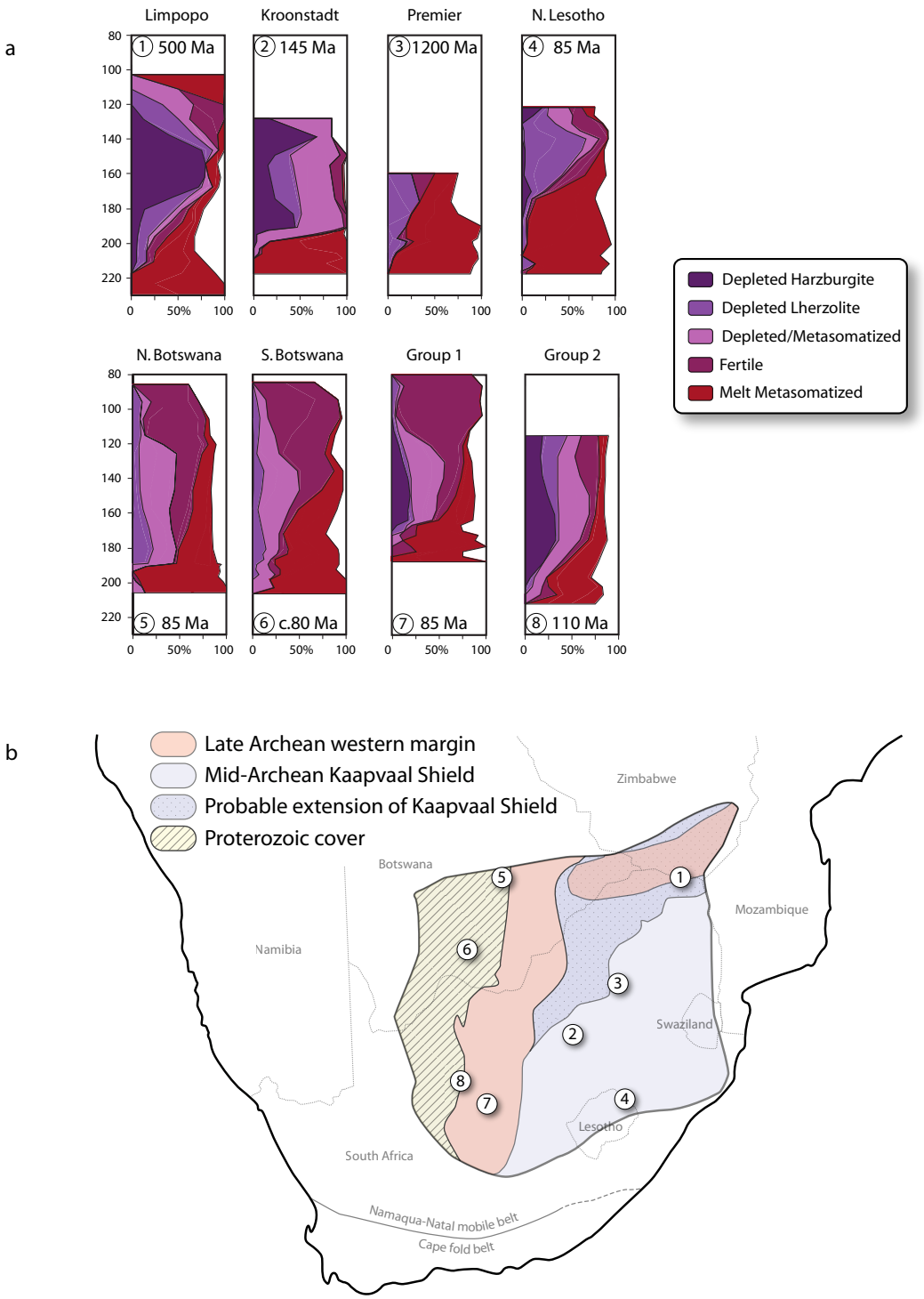

Figure 1.1: **a**. Depth-composition profiles of portions of the Kaapvaal craton reconstructed from garnet xenocrysts (Griffin et al. 2003). The numbers correspond to locations on the map in the lower half of the figure. **b**. Simplified map of the Kaapvaal craton in southern Africa showing the locations of major xenolith/xenocryst hosting kimberlites. Craton boundaries and divisions are from de Wit et al. (1992).

Griffin et al. (2003) presented major- and trace-element data for a database of >3400 garnet xenocrysts from 50 localities in the Kalahari craton. From which they indentified five categories with compositional ranges related to the depletion/metasomatism history of the peridotite from which the garnets are derived. These categories include: (i) depleted harzburgitic or (ii) lherzolitic sources having low HFSE and HREE concentrations, (iii) depleted/metasomatized lherzolites that are depleted in HREE and Y but enriched in LREE and Zr indicating a two-stage history of depletion and metasomatic re-enrichment, (iv) fertile[1] lherzolites that have high HREE concentrations and do not retain a history of previous depletion, (v) melt-metasomatized peridotites that are enriched in Ti, Zr, and Y. The relative proportion of these five categories varies across the Kaapvaal craton (Figure 1.1a).

The mantle represented by garnet xenocrysts in the western half of the craton is largely fertile with subordinate amounts of depleted/metasomatized lherzolites and melt metasomatized peridotites (Figure 1.1a, b). From 95-185 km depth, the mantle section in northern Botswana has approximately equal proportions of depleted/metasomatized lherzolites, fertile lherzolites and melt metasomatized peridotites with fertile peridotites predominating the shallower portion and becoming less abundant with depth. At approximately 190 km depth, the mantle lithosphere is completely composed of metasomatized peridotites with melt metasomatized peridotites making up 85-90% of the section. The lithospheric mantle sections sampled by kimberlites in southern Botswana and, during the Group 1 event, in the Kimberley area of South Africa are similar; both are dominated by fertile lherzolites with subordinate amounts of depleted/metasomatized and melt metasomatized peridotites. At a depth of ~130 km in the Kimberley profile and 150 km depth in the southern Botswana section, the proportion of metasomatized peridiotite dramatically increases to comprise 75 to 100% of the deepest portions of the lithosphere. An increase in melt metasomatized peridotites towards the base of the lithosphere is a

[1] i.e. having a greater relative concentration of elements (e.g. Fe, Ca, Ti, Al) capable of forming basaltic melts upon partial melting

feature common to all the mantle sections described by Griffin et al. (2003), suggesting that melt metasomatism affected the entire craton. The extent to which the lithospheric mantle was changed by metasomatizing melts varies considerably among kimberlites across the craton but it is apparent that melts rising from the asthenosphere are a significant and ubiquitous cause of changing lithospheric mantle composition.

The southwest portion of the craton includes kimberlites that erupted in two distinct time slices. Group 2 kimberlites are generally older than 110 Ma whereas Goup 1 kimberlites are generally younger than 95 Ma (see Gurney et al. 2005). This provides the opportunity to examine temporal changes in the composition of the lithospheric mantle. The lithospheric mantle sampled by the older Group 2 kimberlites retains evidence of the original, more depleted nature of the subcratonic lithospheric mantle. The proportion of depleted harzburgite and lherzolite is greater in the chemical profile determined for the garnet xenocrysts from Group 2 kimberlites; garnets from fertile and melt-metasomatized lithologies are subordinate (Griffin et al. 2003). The depth section of lithospheric mantle represented by garnet xenocrysts from Group 1 kimberlites, in contrast, is dominated by fertile lithologies to approximately 120 km depth. Between ~120 km and ~170 km, the Group 1 kimberlites sampled mantle similar to that found in the Group 2 kimberlites (Figure 5 of Griffin et al. 2003). Garnet xenocrysts from the deepest portions – 190 to 210 km for Group 2 kimberlites and 175 to 190 km depth for Group 1 kimberlites – indicate that melts rising from the asthenosphere had a significant metasomatizing effect on the cratonic lithospheric mantle.

The overall greater depletion preserved by garnet xenocrysts in the Group 2 kimberlites compared with the later erupted Group 1 kimberlites is evident in the higher molar Mg-number of olivine, calculated from garnet xenocryst compositions (Griffin et al. 2003). Consistent with the increasing proportion of melt metasomatized garnets with depth, there is a strong decrease in olivine Mg-number with increasing depth in sections from both the Group 1 and Group 2 kimberlites. The calculated mean olivine Mg-number

for Group 2 kimberlites decreases from 93.2 at 150 km to 91.6 at 200 km depth (Griffin et al. 2003). The decrease in olivine Mg-number for Group 1 kimberlites is even more pronounced– dropping from 92.7 at 150 km to 88.2 at 180 km depth (Griffin et al. 2003). It is clear from the garnet xenocryst data that the 110 Ma metasomatic event linked to eruption of the Group 2 kimberlites (e.g. Konzett et al. 1998) re-enriched and refertilized the lithospheric mantle beneath the Kaapvaal craton.

1.2. Slave Craton

1.2.1. Crustal geology

The Archean Slave Craton in northern Canada is a relatively small component of the larger North American craton. It is bounded on the east by the Wopmay fault zone and Wopmay orogen, to the west by the Bathurst fault and Thelon front, and to the south by the Great Slave Lake shear zone. The Slave craton has an exposed aerial extent of approximately 350,000 km^2. The central and western portions of the craton are underlain by the Central Slave Basement Complex comprised of tonalitic to dioritic gneisses and other foliated granitoids. Some of the Acasta gneisses in the western boundary of the central Slave craton have protolith ages older than 4.0 Ga, and are among the oldest rocks thus far found (Bowring and Williams 1999). The basement gneisses are overlain by thin but widespread quartzites and iron formations. These thin metasedimentary units are in turn overlain by thick sequences of tholeiitic basalts with subordinate amounts of komatiite and rhyolite tuffs. Precise age dates place the upper limit of this volcanism at 2720 to 2700 Ma (Isachsen and Bowring 1997). Granitic plutons of the Defeat and Concession suites were emplaced in the northwest and southeast portions of the craton at ~2630 Ma (Davis and Bleeker 1999). A major regional shortening was accompanied by the emplacement of evolved, K-feldspar-rich granitic plutons throughout the craton at 2590 to 2580 Ma (Davis and Bleeker 1999) the exact cause of which is still speculative. For a more comprehensive overview of the geology of the Slave craton, the reader is referred to Davis et al. (2003).

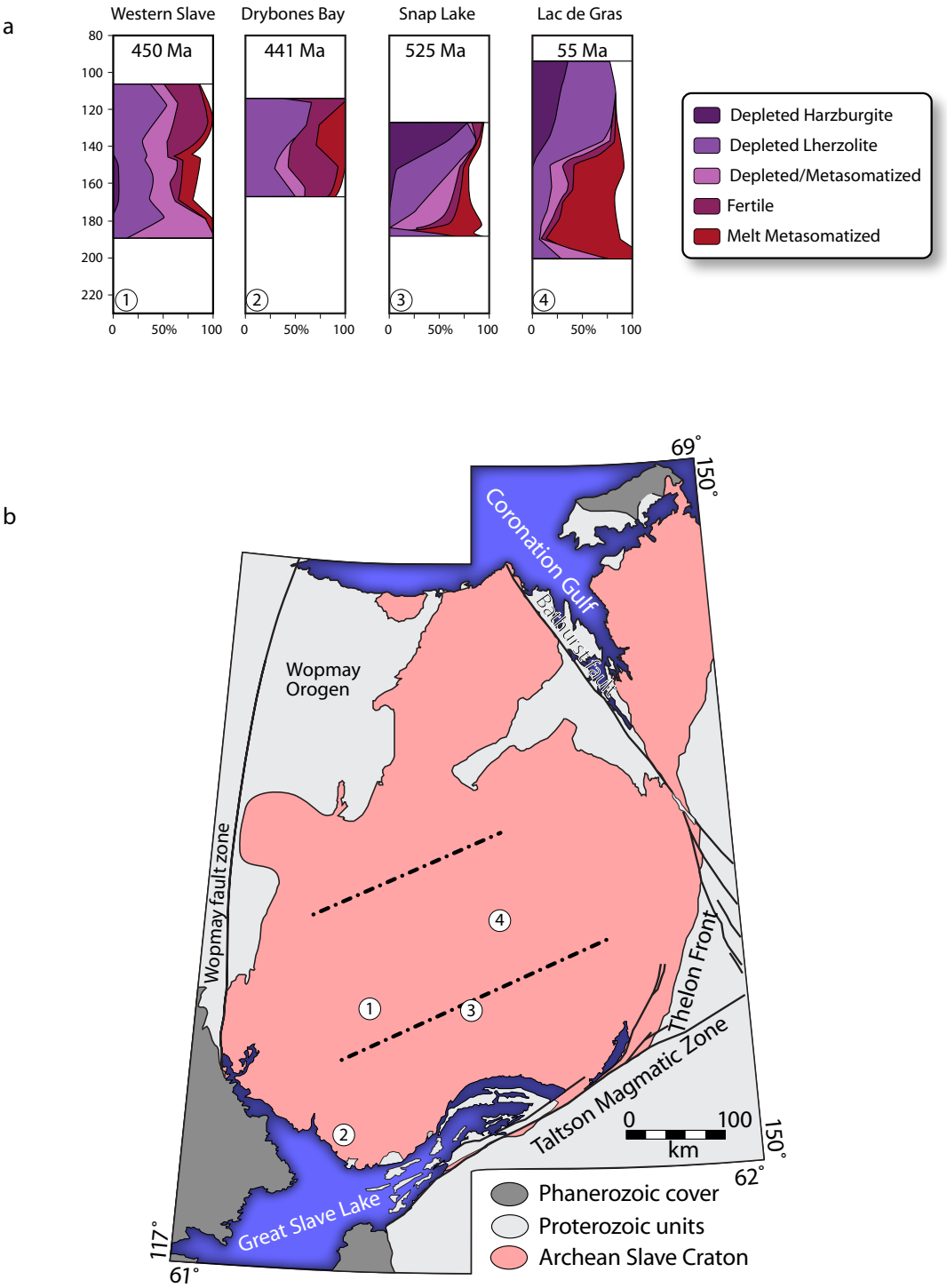

Figure 1.2: **a**. Depth-composition profiles reconstructed from garnet xenocrysts from localities in Slave craton, northern Canada (Griffin et al. 2004). Age dates are from Heaman et al. (2004). **b**. Simplified map of the Slave craton (modified after Bleeker and Davis 1999) showing the xenocryst locations in part **a**. The dashed lines show the lithospheric mantle divisions of Grütter et al. (1999) based on the composition of garnet xenocrysts.

1.2.2. Petrology of the Slave lithospheric mantle

Despite fewer studies of mantle-derived xenoliths and xenocrysts from the Slave Craton compared with the Kaapvaal Craton, sufficient data are available to compare the composition and evolution of the lithospheric mantle beneath these two cratons. The following overview of the subcratonic lithospheric mantle beneath the Slave craton focuses on the garnet xenocryst data published by Griffin et al. (2004).

The lithospheric mantle beneath the Slave craton is divided by Grütter et al. (1999) into three north-east trending domains based on Cr_2O_3-CaO compositions of garnet xenocrysts (Figure 1.2b). Garnets in the northern domain are predominantly eclogitic and lherzolitic; harzburgitic garnets are rare. The central domain includes a significant population of strongly subcalcic harzburgitic (CaO < 1.8 wt%) garnets, which may indicate the presence of ultradepleted dunitic peridotites in the lithospheric mantle beneath the central Slave craton. The southern domain mantle lithosphere is dominated by eclogite and lherzolite but also contains a distinct population of high-Cr_2O_3 harzburgitic garnets with CaO concentrations > 1.8 wt% (Grütter et al. 1999). The chemical characteristics of the lithospheric mantle in the southern domain are based primarily on garnet xenocrysts from the eastern portion of the domain. Carbno and Canil (2002) subdivided the southern domain into south-eastern and south-western subdomains based on the absence of high-Cr garnets in the Drybones Bay kimberlite situated in the southwest part of the craton (Figure 1.2).

Like the Kaapvaal craton, there are several time slices of mantle compositions represented in the garnet xenocryst data, thus the lateral compositional heterogeneity indicated for the Slave lithospheric mantle is difficult to separate from temporal changes caused by repeated phases of metasomatism. Kimberlites erupted in the southern Slave craton earlier (Cambrian ages) than in the northern Slave craton (Jurassic ages); kimberlites in the Lac de Gras field in the central Slave have Cretaceous-Eocene eruption ages (Heaman et al. 2004; Figure 1.2a,b).

Overall, the Slave lithospheric mantle shallower than 160 km depth is dominated by depleted lherzolite with melt metasomatized peridotite forming a large proportion of the lithospheric mantle at greater depths. Depleted harzburgite is only observed in significant abundance in the Snap Lake and Lac de Gras depth profiles. Fertile lithologies form a significant portion of the lithospheric mantle in the Drybones Bay kimberlite (southwestern portion of the craton), and from kimberlites in the western central and northern Slave craton (Griffin et al. 2004). More fertile mantle is a minor part of the mantle lithosphere at Snap Lake and Lac de Gras.

References

Ballhaus C (1993) Redox states of lithospheric and asthenospheric upper mantle. Contrib Mineral Petrol 114:331-348

Bowring S, Williams I (1999) Priscoan (4.00-4.03 Ga) orthogneisses from northwestern Canada. Contrib Mineral Petrol 134:3-16

Boyd FR (1989) Compositional distinction between oceanic and cratonic lithosphere. Earth Planet Sci Lett 96:15-26

Carbno G, Canil D (2002) Mantle Structure Beneath the SW Slave Craton, Canada: Constraints from Garnet Geochemistry in the Drybones Bay Kimberlite. J Petrol 43:129-142

Davis WJ, Bleeker W (1999) Timing of plutonism, deformation, and metamorphism in the Yellowknife Domain, Slave Province, Canada. Can J Earth Sci 36:1167-1187

Davis WJ, Jones AG, Bleeker W, Grutter H (2003) Lithosphere development in the Slave craton: a linked crustal and mantle perspective. Lithos 71:575-589

de Wit MJ, Roering C, Hart RJ, Armstrong RA, de Ronde CEJ, Green RWE, Tredoux M, Peberdy E, Hart RA (1992) Formation of an Archean continent. Nature 357:553-562

Griffin WL, O'Reilly SY, Ryan CG (1999) The composition and origin of sub-continental lithospheric mantle. In: Boyd FR, Fei Y, Bertka CM, Mysen BO (eds) Mantle petrology : field observations and high-pressure experimentation: a tribute to Francis R. (Joe) Boyd, Geochemical Society, Houston. pp 13-45

Griffin WL, O'Reilly SY, Natapov LM, Ryan CG (2003) The evolution of lithospheric mantle beneath the Kalahari Craton and its margins. Lithos 71:215-241

Griffin WL, O'Reilly SY, Doyle BJ, Pearson NJ, Coopersmith H, Kivi K, Malkovets V, Pokhilenko N (2004) Lithosphere mapping beneath the North American plate. Lithos 77:873-922

Grütter H, Apter DB, Kong J (1999) Crust-Mantle Coupling: Evidence from Mantle-Derived Xenocrystic Garnets. In: Gurney JJ, Gurney JL, Pascoe MD, Richardson SH (eds) Proceedings of the 7th International Kimberlite Conference. Red Roof Design, Cape Town, South Africa, pp 307-313

Gurney JJ, Helmstaedt H, Le Roex AP, Nowicki T, Richardson SH, Westerlund K (2005) Diamonds: Crustal distribution and formation processes in time and space and an integrated deposit model. Econ Geol 100th Anniversary Volume:143-177

Haggerty SE (1986) Diamond genesis in a multiply-constrained model. Nature 320:34-38

Isachsen C, Bowring S (1997) The Bell Lake Group and Anton Complex. A basement-cover sequence beneath the Archean Yellowknife greenstone belt revealed and implicated in greenstone belt formation. Can J Earth Sci 34:169-189

Jordan TH (1978) Composition and development of the continental tectosphere. Nature 274:544-548

Konzett J, Armstrong RA, Sweeney RJ, Compston W (1998) The timing of MARID metasomatism in the Kaapvaal mantle: An ion probe study of zircons from MARID xenoliths. Earth Planet Sci Lett 160:133-145

Luth RW, Virgo D, Boyd FR, Wood BJ (1990) Ferric iron in mantle-derived garnets: Implications for thermobarometry and for the oxidation state of the mantle. Contrib Mineral Petrol 104:56-72

McCammon CA, Griffin WL, Shee SR, O'Neill HSC (2001) Oxidation during metasomatism in ultramafic xenoliths from the Wesselton kimberlite, South Africa: implications for the survival of diamond. Contrib Mineral Petrol 141:287-296

McCammon CA, Kopylova MG (2004) A redox profile of the Slave mantle and oxygen fugacity control in the cratonic mantle. Contrib Mineral Petrol 148:55-68

Navon O, Hutcheon ID, Rossman GR, Wasserburg GJ (1988) Mantle-derived fluids in diamond micro-inclusions. Nature 335:784-789

Poujol M, Robb L, Anhaeusser C, Gericke B (2003) A review of the geochronological constraints on the evolution of the Kaapvaal Craton, South Africa. Precambrain Res 127:181-213

Woodland AB, Koch M (2003) Variation in oxygen fugacity with depth in the upper mantle beneath the Kaapvaal craton, southern Africa. Earth Planet Sci Lett 214:295-310

Woodland A, Kornprobst J, Tabit A (2006) Ferric iron in orogenic lherzolite massifs and controls of oxygen fugacity in the upper mantle. Lithos 89:222-241

Chapter 2: Diamondiferous peridotitic microxenoliths from the Diavik Diamond Mine, NWT[1]

2.1. Introduction

Our knowledge of the primary sources of diamonds in the lithospheric upper mantle is mainly derived from studies of mantle xenoliths in kimberlites and of mineral inclusions in diamonds themselves. Inclusions in diamonds preserve evidence of the physical and chemical environment at the time of diamond formation, presumed to have occurred early in Earth's history (e.g. Richardson et al. 1984). Mantle xenoliths, in contrast, integrate a more protracted history that may have involved multiple stages of melt extraction, thermal re-equilibration in response to short lived thermal pulses or to secular cooling, and metasomatic re-enrichment. Rare diamond-bearing peridotite xenoliths provide unique opportunities to study the principal source of diamonds in the Earth's mantle directly and to obtain information on the evolution of cratonic lithosphere spanning the time from diamond formation to kimberlite eruption. Based on inclusion studies, peridotitic diamonds largely formed in depleted harzburgitic sources (Gurney and Switzer 1973; Gurney 1984). Evidence for changes in the composition of peridotitic subcratonic lithospheric mantle over time, involving a decreasing ratio of harzburgite to lherzolite (Griffin et al. 2003), raises the possibility that diamonds are stored in mantle rocks that are compositionally quite distinct from the rocks in which the diamonds originally formed. This would have important implications for diamond exploration, because indicator mineral assessment - evaluating the state of mantle lithosphere at the time of kimberlite eruption - is strongly based on chemical criteria derived from inclusion studies depicting the environment of diamond formation. One of the key questions for our study of diamondiferous peridotite xenoliths from Diavik, therefore, is verifying the extent to which the originally highly depleted signature at the time of diamond formation has been preserved or modified during

1 A version of this chapter is published as Creighton S, Stachel T, McLean H, Muehlenbachs K, Simonetti A, Eichenberg D, Luth R (2008) Diamondiferous peridotitic microxenoliths from the Diavik Diamond Mine, NT. Contributions to Mineralogy and Petrology 155:541-554

subsequent metasomatic events.

2.1.1. Mantle sample at Diavik

The Diavik diamond mine is located within Lac de Gras, approximately 300 km northeast of Yellowknife, NWT, in the central portion of the Archean Slave craton northern Canada (Figure 2.1). Based on the composition of xenoliths and garnet xenocrysts, Griffin et al. (1999a) inferred that the mantle beneath the Lac de Gras area is chemically and thermally stratified. They suggested that an 'ultradepleted,' predominantly harzburgitic layer overlies a less depleted, predominantly lherzolitic layer with the transition being located at ~145 km depth. Griffin et al. (1999a) proposed the shallower 'ultradepleted' layer to represent Mesoarchean oceanic or sub-arc mantle lithosphere and the lower layer to be the frozen head of a Neoarchean plume derived from the lower mantle. Aulbach et al. (2007) suggested that the deeper portions of the lower layer experienced secondary re-enrichment in FeO. An alternative model for the formation of subcratonic lithospheric mantle involves stacking of highly depleted Archean oceanic lithospheric mantle beneath early continents (e.g. Schulze 1986; Helmstaedt and Schulze 1989; Bulatov et al. 1991; de Wit 1998; Stachel et al. 1998). In this model, the observed increase in fertility with depth in the central Slave craton may relate to metasomatism by infiltrating fluids/melts ascending from the asthenosphere (Stachel et al. 2003).

2.2. Samples and Analytical Methods

We studied twenty-one diamond-bearing microxenoliths, ranging from 0.5 to 1.5 cm in diameter, that were recovered at the Production Splitting Facility of Diavik Diamond Mines in Yellowknife, NWT. The diamondiferous microxenoliths are usually bimineralic, consisting of diamond partially or completely included within garnet (Figure 2.2). The diamonds were separated from the host garnets by gentle tapping using a steel breaker resulting in fragmentation of the garnet and preservation of the diamond. Following extraction of the diamonds, their overall morphology, colour and surface features were

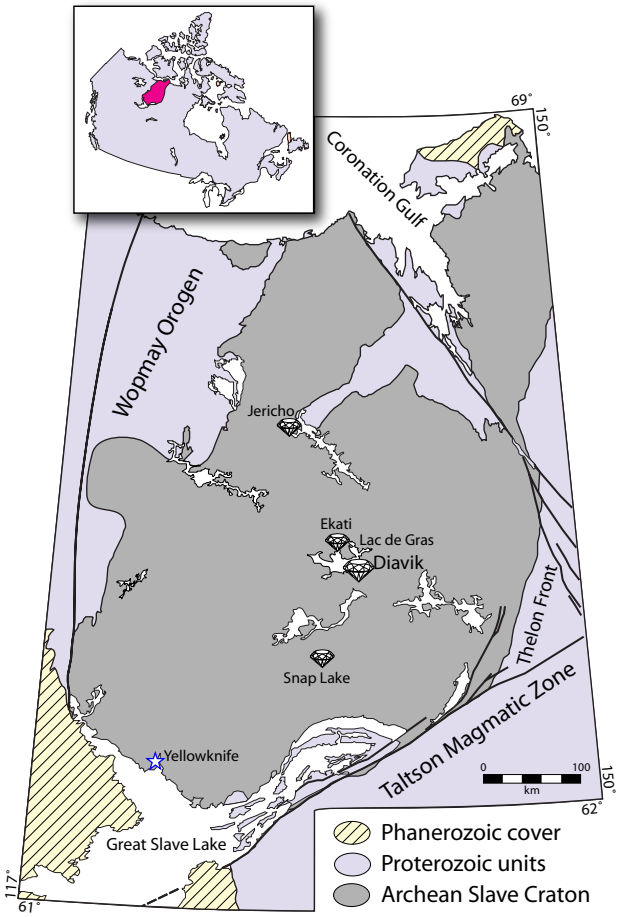

Figure 2.1: Map of the Slave craton in northern Canada showing the location of the Diavik, Ekati, Snap Lake and Jericho diamond mines. Modified after Bleeker and Davis (1999).

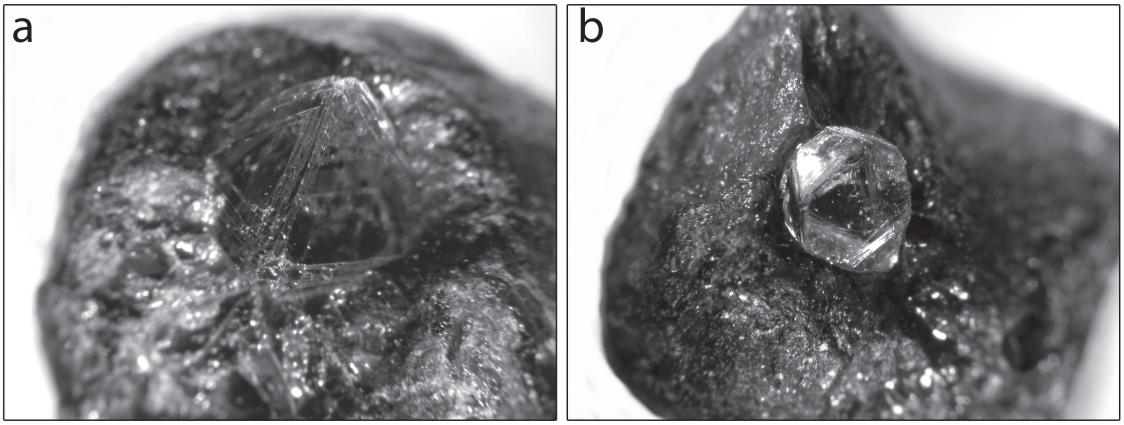

Figure 2.2: Two diamondiferous microxenoliths showing diamonds with octahedral morphologies included within garnets. A: DGD05; B: DGD02. The diameter of each garnet is approximately 1 cm.

documented and tabulated (Table 2.1). During examination of the garnet fragments, seven garnets were found to contain inclusions of minerals other than diamond and one of the diamonds contained an olivine inclusion (Table 2.1). The diamonds were then crushed and fragments were analyzed for nitrogen content and aggregation state, and carbon isotope composition.

Nitrogen concentration and aggregation characteristics of the diamonds were determined on transparent, graphite-free cleavage chips by Fourier transform infrared (FTIR) spectroscopy using a Thermo Nicolet Nexus 470 Spectrometer fitted with a Continuum infrared microscope. Sample spectra (650 to 4000 cm^{-1}) were collected for 200 seconds and, after subtraction of a pure Type II diamond spectrum, converted to absorption coefficient. The diamond spectra were deconvoluted into A, B and D components using software provided by David Fischer (Research Laboratories of the Diamond Trading Company, Maidenhead, UK). The nitrogen concentration, in atomic ppm, was calculated from absorption values at 1282 cm^{-1} for the A- and B-center (Boyd et al. 1994; and 1995). Detection limits are 10-20 ppm and largely depend on the quality of the sample. Accuracy of the reported nitrogen concentrations and aggregation states is generally within 10-20% relative (1σ).

The carbon isotope composition of the diamonds was determined by combusting graphite-free diamond fragments with CuO in an evacuated and sealed silica glass tube for 10 hours at 950ºC. Carbon isotope ratios were measured using a Finnigan Mat 252 mass spectrometer. The data are reported in standard per mille notation relative to the V-PDB standard. Repeat analyses of a single diamond indicate a 1σ analytical precision of better than 0.1‰ (Donnelly et al. 2007).

Garnet fragments, silicate and chromite inclusions recovered from the garnets, and the olivine inclusion from the diamond in sample DGD12 were embedded in Araldite® epoxy resin and prepared to a final polish using 0.05 μm alumina suspension. Major and minor element compositions were obtained by electron probe microanalysis (EPMA) using

Table 2.1: Physical and chemical characteristics of diamonds recovered from the peridotite microxenoliths. Minerals other than diamond recovered as inclusions in the garnets are listed under the heading 'Additional phases.'

Sample	Shape	Colour	N (at. ppm)	%B	Type	T-N (°C)	δ13C (‰)	Additional phases
DGD01	o/a	colourless	178	71	IaAB	1173	-2.63	
DGD02	o	colourless	640	14	IaAB	1077	-4.70	ol, opx
DGD03	o/a	grey	17	55	IaAB	1217	-5.51	opx
DGD05	o	colourless	145	26	IaAB	1130	-6.22	ol, chr
DGD06(a)	ps o	brown	137	47	IaAB	1154	-4.83	
DGD06(b)	f*	colourless	119	13	IaAB	1114	-5.13	
DGD08	o/a	pale grey	54	32	IaAB	1161	-4.44	
DGD10	o/f*	grey	148	32	IaAB	1136	-5.10	chr
DGD11	o/t	colourless	79	3	IaA	1087	-	
DGD12	ps/o	pale brown	370	98	IaB	1234	-5.43	
DGD13(a)	ps o	brown	64	69	IaAB	1197	-5.55	ol
DGD13(b)	f	colourless	32	9	IaA	1136	-4.99	
DGD14	o/t	colourless	468	73	IaAB	1151	-3.77	chr
DGD16	ps o/a	grey	522	88	IaAB	1174	-4.58	
DGD18(a)	ps o/a	brown	85	2	IaA	1076	-5.58	chr
DGD18(b)	ps o/a	colourless	384	85	IaAB	1175	-5.72	
DGD19	o/a	grey	120	41	IaAB	1151	-5.46	
DGD20	o	colourless	575	83	IaAB	1161	-4.53	
DGD21	ps o/a	brown	17	5	IaA	1136	-5.62	
DGD22	o	colourless	123	2	IaA	1068	-4.96	
DGD24	o	colourless	66	33	IaAB	1157	-5.36	
DGD25	o	colourless	544	65	IaAB	1138	-3.46	
DGD26	ps o/a, t	colourless	333	37	IaAB	1122	-4.58	
DGD27(a)	o/ps	brown	226	22	IaAB	1179	-5.32	
DGD27(b)	o	brown	96	62	IaAB	1114	-5.35	

a *aggregate*
f* *broken during extraction*
f *fragment*
o *octahedral*
ps *pseudohemimorphic*
t *twinned*

ol *olivine*
opx *orthopyroxene*
chr *chromite*

a JEOL JXA-8900 Superprobe operating at 20 kV gun potential and 20 nA beam current. Natural and synthetic mineral, oxide and metal standards were used to convert raw counts to weight percent using the online CITZAF correction method. Count times (peak) ranged from 30 to 60 seconds and half the peak count time on each background; detection limits based on the average of 5 spots are less than 100 ppm for all reported oxides except for P_2O_5 (250 ppm). Concentrations at or below the minimum limit of detection are indicated in analytical tables where appropriate.

Trace-element compositions of the garnets were measured using a Merchantek

UP 213 UV laser ablation system connected to a Perkin Elmer Elan 6000 quadrupole inductively coupled plasma mass spectrometer (ICP-MS). The analysis spot size was 160 μm in diameter and an average of at least three spots is reported. Concentrations at or below the minimum detection limits are indicated in the tables.

2.3. Database

For comparison purposes, we have compiled a database of all accessible mineral analyses of diamondiferous garnet peridotite xenoliths from localities worldwide. This dataset includes 28 xenoliths from southern Africa – 14 from Newlands (Daniels et al. 1995; Menzies et al. 1999), eight from Roberts Victor (Viljoen et al. 1994), four samples from Finsch (Shee et al. 1982; Viljoen et al. 1992), one from Premier (Viljoen et al. 2004), and one from Mothae (Dawson and Smith 1975); 20 from Siberia – 15 from the Udachnaya pipe (Sobolev et al. 1984) and five from the Aikhal kimberlite (Sobolev 1974); and one from Wyoming, USA (McCallum and Eggler 1976). Several diamondiferous peridotite xenoliths have been described from the Argyle lamproite in western Australia (Jaques et al. 1990) but garnet in these samples is not preserved, therefore, these data are not included in the database.

2.4. Diamonds

2.4.1. Physical characteristics

Twenty-five diamonds were recovered for analysis from the 21 peridotitic microxenoliths examined. Fourteen out of 25 of the diamonds are octahedra including intergrowths of octahedral crystals. Nine of the diamonds have some development toward dodecahedral forms on surfaces exposed outside of their garnet hosts resulting in pseudohemimorphism (Robinson 1979). Two diamonds are unresorbed fragments (Table 2.1). Three of the crystals are twinned with herringbone patterns marking the composition planes. Surface features on octahedral faces are stacked growth layers (observed on all of

the diamonds) and negatively oriented trigons (eight diamonds). Narrow hillocks occur on dodecahedral faces. Eighteen of the diamonds recovered are colourless or pale grey, seven have pale to intense brown body colours. Plastic deformation lines, only observable on resorbed dodecahedral surfaces, are absent. But, taking the brown body colour of the diamonds as evidence for plastic deformation (Harris 1992), approximately one third of the diamonds show evidence of strain.

Multiple diamonds were observed in four of the microxenolith samples. DGD06 contained a brown pseudohemimorphic and a colourless diamond that was broken during extraction from the garnet host. DGD13 contained one large brown diamond and a smaller colourless irregularly shaped crystal; DGD18 contained an aggregate of a brown and four colourless pseudohemimorphic diamonds (only one of the colourless diamonds was analysed); DGD27 contained an intergrowth of two brown diamonds – one sharp-edged octahedron and one pseudohemimorphic octahedron (Figure 2.3a). In each case, the

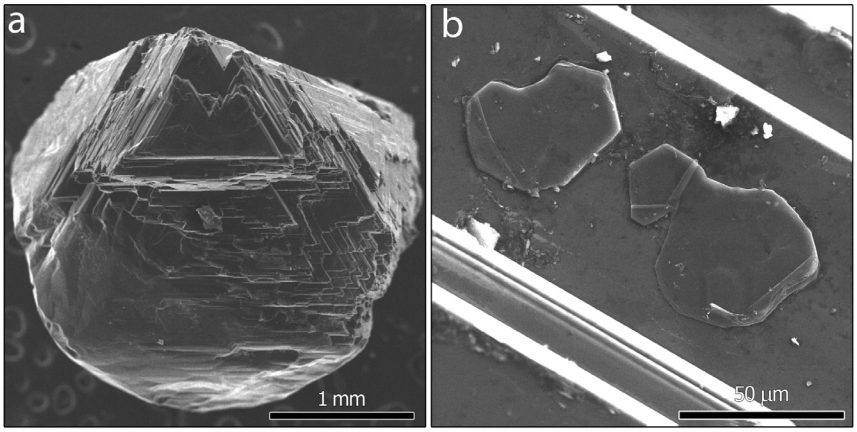

Figure 2.3: Left: Secondary electron image of a brown pseudohemimorphic diamond from sample DGD27. Note the stacking of octahedral growth layers on the upper portion of the diamond and the gradual resorption to a rounded dodecahedral morphology towards the base. The octahedral portion of the diamond was completely encapsulated within the host garnet and was protected from interaction with the kimberlite. Right: Secondary electron image of thin, roughly hexagonal graphite platelets on a growth plane of the diamond from DGD05. Graphitization of this type was observed on 13 of the diamonds studied and in every case was restricted to the surface of the diamond enclosed in garnet.

diamonds were separated before being crushed for FTIR and isotopic analysis, in order to determine if variability exists between multiple diamonds from the same microxenolith.

Graphite is associated with the diamonds both as inclusions and as thin hexagonal platelets in shallow, flat-bottomed depressions (Figure 2.3b). Graphite on diamond surfaces is restricted to portions of the diamond completely encapsulated inside the host garnet, which presumably shielded the diamond surface from interaction with the transporting kimberlitic melt. Graphite inclusions occur as small, thin flakes.

2.4.2. Nitrogen content and aggregation state, and carbon isotope composition

The nitrogen concentrations in the diamonds range from 17 to 640 atomic ppm. Assuming that all nitrogen is located in the infrared active A and B centers, nitrogen aggregation is commonly expressed as the relative percentage of the fully aggregated B-center (%B). Type IaA diamonds have >90% of their nitrogen in the form of poorly aggregated A-centers; Type IaB diamonds have >90% of their nitrogen located in B-centers. Diamonds with nitrogen aggregation states falling between these two end-members are classified as Type IaAB. The diamonds from the Diavik microxenoliths are mostly Type IaAB having between 2 and 98 %B (Table 2.1), overlapping with other diamonds from the Slave craton (Figure 2.4).

Diamonds from the four samples that contained two types (colour or shape) of diamond have different nitrogen contents and aggregations states (Table 2.1; shown connected with tie-lines on Figure 2.4). Within the analytical precision, the two diamonds from DGD06 have the same total nitrogen concentrations but the brown diamond has nitrogen more aggregated than the colourless diamond. The brown diamond from sample DGD13 has a higher total nitrogen concentration and higher levels of nitrogen aggregation than the associated colourless diamond. The diamonds in sample DGD18 have the opposite relationship; the brown diamond has a lower total nitrogen concentration and is poorly aggregated (85 ppm, 2 %B) relative to the colourless diamond (384 ppm, 85 %B). The

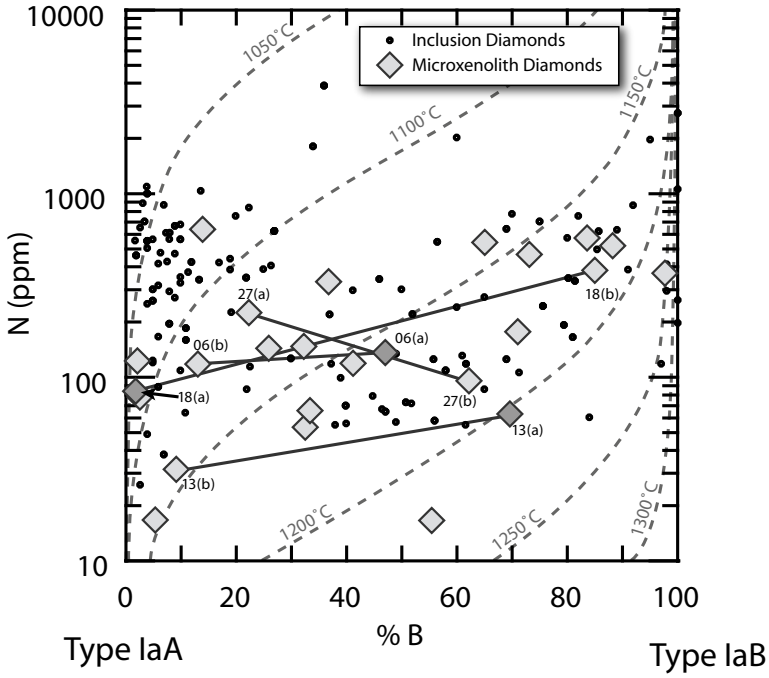

Figure 2.4: Total nitrogen concentration (atomic ppm) versus aggregation state (relative proportion of nitrogen in the higher aggregated B-center). Isotherms for time averaged (3.5 Ga; Westerlund et al. 2006) residence temperatures calculated after Taylor, et al. (1990) and Leahy and Taylor (1997). Diamonds from the microxenoliths are shown as diamond shapes and inclusion-bearing diamonds from the Diavik mine are shown as dots. Tie lines connect diamonds from the same garnet.

octahedral diamond in sample DGD27 has 96 atomic ppm N with 62 %B whereas the psuedohemimorphic diamond has 226 ppm nitrogen with 22 %B.

The microxenolith diamonds have a narrow range of carbon isotope compositions, from -6.2 to -2.6‰ (Figure 2.5a). The measured carbon isotope compositions for the microxenolith diamonds spans the entire range seen in the peridotitic inclusion-bearing diamonds from Diavik (Donnelly et al. 2007; see Figure 2.5b). Both sub-populations, the inclusion-bearing Diavik production and the microxenolith diamonds, have a mode at approximately -5‰ (Figure 2.5a,b) consistent with the accepted mantle value (e.g. Deines 2002). Three microxenolith diamonds (from DGD01, DGD14, and DGD25) extend the distribution to isotopically heavier values than observed for the inclusion-bearing diamonds, suggesting the presence of an additional peridotitic diamond sub-population that either was

not sampled in the inclusion study of Donnelly et al. (2007) or is not present as inclusion-bearing diamonds.

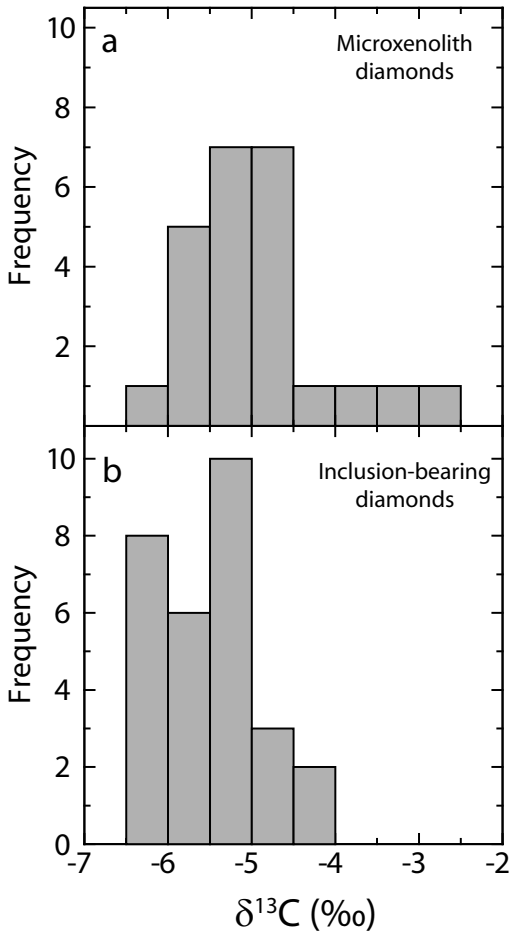

Figure 2.5: Carbon isotope composition of Diavik peridotitic diamonds. Both sample suites, the inclusion-bearing diamonds (Donnelly et al. 2007, bottom) and the microxenolith diamonds (top), have similar modes near the accepted mantle value of -5‰ (Deines 2002).

There is no correlation observed between the carbon isotope composition and the nitrogen content or aggregation state.

2.5. Silicate and oxide minerals

2.5.1. Host Garnets

Molar Mg-numbers (100*Mg/[Mg+Fe]) of the garnets are between 82.3 and 86.3, and Cr_2O_3 concentrations vary from 3.2 to 14.7 wt% (Table 2.2). CaO concentrations range

from 3.5 to 7.6 wt%. In the classification scheme of Grütter et al. (2004), eight garnets are classified as G10 (harzburgitic), twelve are G9 (lherzolitic) and one is a G11 (high-Ti peridotitic). Five of the G10 garnets fall just to the low CaO side of the G9/G10 division line (Figure 2.6); the other three G10 garnets are lower in CaO and plot clearly in the G10 field. The one G11 garnet (DGD14) falls into the G9 field (Figure 2.6) but has a higher TiO_2 concentration: 0.55 wt% compared to an average of ~0.11 wt% for the other microxenoliths

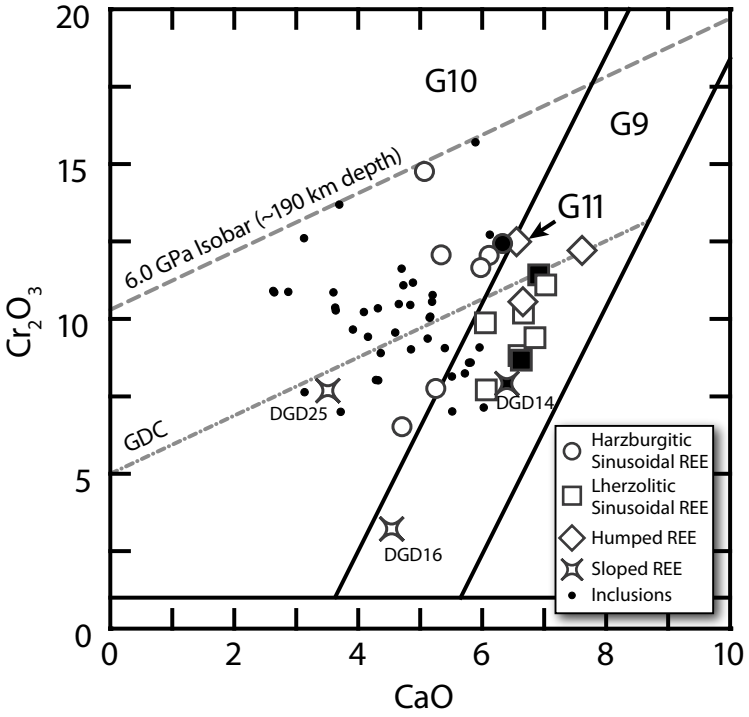

Figure 2.6: CaO-Cr_2O_3 plot (compositional fields after Grütter et al. 2004) of peridotitic garnets associated with diamonds from the Diavik Diamond Mine. Garnet inclusions in diamonds (Donnelly et al. 2007) are shown as black dots; the microxenolith garnets are shown with the larger symbols corresponding to the shape of their respective REE_N pattern (see Figure 2.7). Solid symbols are garnets that contained chromite. Note the dominance of high-Cr_2O_3 G9 garnets in the microxenolith garnets compared with a predominance of G10 garnets and 'low' Cr in G9 garnets as inclusions in diamonds. The 6.0 GPa isobar, marking the minimum depth to the base of the lithosphere defined by these samples, and the position of the graphite-diamond constraint (GDC) are from Grütter et al. (2006).

Table 2.2 (following page): Average major- and trace-element concentrations of the garnets measured using EPMA and LA-ICPMS, respectively. Garnet classification after Grütter et al. (2004); pressure estimates (P_{38}) are calculated for a 38 mW/m^2 geotherm after Grütter et al. (2006); T_{Ni} after Canil (1999).

Sample	DGD01	DGD02	DGD03	DGD05	DGD06	DGD08	DGD10	DGD11	DGD12	DGD13	DGD14	DGD16	DGD18	DGD19	DGD20	DGD21	DGD22	DGD24	DGD25	DGD26	DGD27
P_2O_5	b.d.	0.04	b.d.	0.04	b.d.	b.d.	b.d.	b.d.	b.d.	b.d.	b.d.	b.d.	0.03	0.03	b.d.	0.03	0.03	0.03	b.d.	b.d.	0.04
SiO_2	41.10	40.92	40.85	40.66	41.03	40.71	40.95	40.73	40.66	40.24	40.89	41.92	40.48	40.67	40.58	40.54	41.48	40.75	41.54	40.58	40.38
TiO_2	0.12	0.02	0.13	0.12	0.05	0.09	0.08	0.10	0.11	0.55	0.16	0.13	0.12	0.17	0.08	0.31	0.07	0.14	0.08	0.05	0.10
Al_2O_3	18.02	18.49	15.80	14.46	17.29	14.54	17.28	16.53	14.98	13.95	17.90	21.68	15.21	15.98	16.86	14.33	19.36	14.97	18.56	15.78	12.83
Cr_2O_3	7.71	7.73	10.19	12.41	8.81	12.02	8.67	9.87	11.63	12.49	7.91	3.23	11.42	10.55	9.39	12.21	6.49	12.04	7.68	11.09	14.73
V_2O_3	0.05	0.05	0.08	0.05	0.07	0.06	0.07	0.05	0.06	0.05	0.05	0.03	0.05	0.05	0.06	0.07	0.04	0.04	0.05	0.07	0.06
FeO	6.64	6.68	7.03	6.27	6.73	7.22	6.57	6.73	6.77	6.52	6.51	6.49	6.38	6.15	6.68	6.36	6.32	6.08	6.16	6.27	6.49
MnO	0.40	0.41	0.39	0.39	0.41	0.40	0.37	0.43	0.43	0.39	0.40	0.33	0.40	0.38	0.41	0.40	0.37	0.38	0.36	0.39	0.44
MgO	19.45	20.08	18.69	19.18	18.90	18.79	19.06	19.16	19.22	18.67	19.22	21.33	18.64	19.13	18.65	18.12	20.79	20.03	21.81	18.68	19.77
CaO	6.07	5.27	6.67	6.34	6.60	6.13	6.63	6.05	5.99	6.56	6.40	4.54	6.91	6.66	6.85	7.61	4.72	5.35	3.50	7.03	5.08
Na_2O	0.03	0.02	0.03	0.03	0.02	0.04	0.02	0.03	0.02	0.08	0.02	0.04	0.02	0.03	0.03	0.04	0.02	0.05	0.03	0.02	0.02
K_2O	b.d.	b.d.	b.d.	b.d.	b.d.	b.d.	b.d.	b.d.	b.d.	b.d.	b.d.	b.d.	b.d.	b.d.	b.d.	b.d.	b.d.	b.d.	b.d.	b.d.	b.d.
Total	99.59	99.66	99.85	99.92	99.92	100.00	99.69	99.67	99.86	99.49	99.47	99.71	99.63	99.76	99.60	100.00	99.66	99.84	99.76	99.95	99.91
Sc	142	128	172	154	154	183	139	157	166	135	148	98	153	161	151	153	110	140	149	180	231
Ti	713	148	857	820	325	580	557	609	690	3363	1051	914	763	1116	565	1919	457	966	515	307	699
V	238	247	346	262	341	267	323	265	311	243	240	159	309	251	318	317	221	218	244	335	344
Ni	36.6	31.0	44.5	39.2	35.2	38.4	46.9	36.5	45.5	44.2	34.2	43.9	42.5	45.8	46.9	49.5	47.1	46.7	44.2	47.3	53.3
Zn	10.6	11.1	12.0	11.5	10.4	11.8	11.1	11.9	12.3	12.1	10.0	11.6	12.0	12.3	13.4	13.9	12.0	13.0	12.1	12.9	14.0
Ga	3.34	2.29	5.73	3.65	3.60	4.31	3.38	4.87	4.81	4.51	3.63	5.06	3.51	3.03	4.50	5.67	3.30	5.55	4.53	5.17	2.70
Rb	0.80	b.d.	b.d.	b.d.	0.02	b.d.	b.d.	0.05	0.04	b.d.	0.05	0.28	b.d.	0.03	0.07	0.06	0.04	0.07	0.88	0.03	b.d.
Sr	0.66	0.42	0.34	1.16	0.80	0.77	0.75	2.81	1.47	0.70	0.68	0.96	0.97	0.76	1.34	2.99	0.42	1.13	1.13	0.97	0.75
Y	1.70	1.50	1.88	2.98	0.92	0.60	1.71	1.90	1.38	14.26	5.02	8.68	1.99	10.72	1.78	18.02	1.70	3.20	6.35	1.28	3.69
Zr	6.98	15.57	9.90	30.91	3.51	4.13	10.13	7.04	7.63	57.94	11.11	6.18	29.74	28.25	8.70	43.66	11.95	21.95	7.32	6.39	60.35
Nb	1.12	0.83	1.13	1.13	1.19	1.95	0.93	1.54	1.31	0.92	1.03	0.66	1.25	1.31	1.48	1.94	0.74	1.46	0.70	1.39	1.78
Cs	b.d.	b.d.	b.d.	b.d.	b.d.	b.d.	b.d.	0.02	b.d.	b.d.	b.d.	b.d.	0.02	0.02	b.d.	b.d.	b.d.	b.d.	0.04	b.d.	b.d.
La	0.07	0.09	0.10	0.17	0.10	0.12	0.13	0.67	0.33	0.25	0.12	0.38	0.15	0.14	0.21	0.67	0.06	0.22	0.28	0.14	0.23
Ce	0.80	0.68	0.83	1.42	1.07	0.79	1.46	1.92	2.65	1.77	0.85	0.52	1.34	1.21	1.46	2.56	0.44	1.50	0.86	1.29	2.02
Pr	0.28	0.41	0.28	0.55	0.42	0.24	0.54	0.47	0.95	0.53	0.24	0.11	0.52	0.43	0.45	0.74	0.19	0.49	0.21	0.51	0.78
Nd	2.10	5.03	1.84	5.18	3.69	2.37	3.17	3.57	6.98	4.01	2.27	0.77	4.85	3.78	2.93	6.89	2.01	4.85	1.38	4.82	6.41
Sm	0.74	1.38	0.65	2.59	0.74	0.90	0.65	1.09	1.24	2.23	0.90	b.d.	1.76	1.83	0.81	2.93	1.19	1.52	0.70	0.86	2.09
Eu	0.15	0.38	0.14	0.70	0.12	0.23	0.19	0.26	0.26	0.87	0.17	0.11	0.51	0.51	0.17	0.96	0.22	0.49	0.11	0.16	0.60
Gd	0.51	0.79	0.37	2.00	0.24	0.38	0.65	0.57	0.47	3.58	0.63	0.58	1.37	2.18	0.44	3.78	0.59	1.28	0.44	0.37	1.44
Tb	0.05	0.08	0.06	0.21	0.02	0.04	0.08	0.06	0.06	0.62	0.12	0.13	0.14	0.38	0.05	0.59	0.06	0.18	0.09	0.04	0.17
Dy	0.42	0.45	0.40	0.91	0.16	0.18	0.55	0.31	0.24	3.66	0.77	1.08	0.48	2.42	0.30	3.71	0.33	0.83	0.84	0.29	0.83
Ho	0.08	0.07	0.07	0.09	0.04	0.02	0.10	0.07	0.06	0.62	0.19	0.31	0.08	0.39	0.05	0.68	0.08	0.13	0.23	0.06	0.14
Er	0.20	0.20	0.21	0.26	0.14	0.08	0.18	0.22	0.20	1.15	0.60	1.20	0.18	0.91	0.19	1.73	0.21	0.33	0.90	0.15	0.35
Tm	0.06	0.05	0.04	0.02	0.04	0.03	0.05	0.05	0.05	0.14	0.09	0.23	0.05	0.09	0.05	0.20	b.d.	0.05	0.15	0.04	0.04
Yb	0.56	0.25	0.41	0.18	0.30	0.20	0.33	0.48	0.32	0.80	0.82	1.92	0.30	0.61	0.37	1.32	0.33	0.38	1.08	0.28	0.30
Lu	0.12	0.07	0.09	0.08	0.07	0.06	0.07	0.11	0.09	0.13	0.16	0.37	0.06	0.13	0.10	0.20	0.10	0.06	0.22	0.06	0.05
Hf	0.26	0.35	0.30	0.81	0.14	0.11	0.22	0.22	0.16	1.54	0.32	0.28	0.70	0.84	0.20	1.07	0.37	0.57	0.23	0.20	1.52
Ta	0.12	0.07	0.10	0.09	0.11	0.22	0.09	0.11	0.13	0.05	0.11	0.07	0.11	0.13	0.11	0.18	0.08	0.18	0.06	0.15	0.07
Classification	G9	G10	G9	G10D	G9	G10D	G9	G9	G10D	G11	G9	G9	G9	G9	G9	G9	G10	G10D	G10D	G9	G10D
T-Ni (°C)	998	968	1035	1011	991	1007	1045	997	1039	1033	985	1032	1026	1040	1045	1056	1046	1044	1034	1047	1071
P38 (GPa)	3.48	3.65	4.02	4.76	3.67	4.70	3.63	4.08	4.62	4.72	3.47	2.42	4.28	4.12	3.77	4.31	3.40	4.95	4.09	4.17	5.89

garnets (Table 2.2). In the following discussion it will be included in the lherzolitic (G9) group.

Compositional zoning is not observed in any of the garnets.

2.5.2. Silicate and oxide inclusions

Seven of the 21 garnets were found to enclose minerals other than diamond. Olivine was found in three of the garnets; two of the olivine-bearing garnets also contained a third phase (DGD02 – orthopyroxene, and DGD05 – Mg-chromite). The composition of the olivines is Fo_{89} for sample DGD05 and Fo_{93} for the other two olivines. Orthopyroxene recovered from samples DGD02 and DGD03, has Mg-numbers of 93.7 and 92.8 respectively (Table 2.3).

Qualitative energy dispersive spectrometry confirmed that small (30-100 μm) octahedral crystals recovered from four of the microxenoliths (DGD05, 10, 14, and 18) are Mg-chromite. Mg-Chromite from DGD05 was recovered and analyzed using EPMA; the other chromites were lost during sample preparation. The chromite is zoned, with the

Table 2.3: Average major-element composition of silicate and oxide minerals recovered from the garnet fragments. Sample DGD12i is an olivine inclusion recovered from the diamond in sample DGD12.

Sample	**DGD02**	**DGD05**	**DGD13**	**DGD12i**	**DGD02**	**DGD03**	**DGD05**	**DGD05**
Mineral	olivine	olivine	olivine	olivine	opx	opx	chr-core	chr-rim
P_2O_5	b.d.	b.d.	b.d.	b.d	b.d.	b.d.	b.d.	b.d.
SiO_2	40.76	40.15	40.62	41.51	57.22	57.58	0.20	0.18
TiO_2	0.01	0.03	0.01	b.d	0.00	0.01	0.22	0.24
Al_2O_3	0.02	0.02	0.03	0.02	0.51	0.58	8.98	8.42
Cr_2O_3	0.04	0.03	0.07	0.03	0.33	0.32	63.69	62.40
V_2O_3	b.d.	b.d.	b.d.	b.d	b.d.	b.d.	0.18	0.22
FeO	7.89	10.21	7.57	4.70	4.35	4.96	14.17	17.73
MnO	0.11	0.15	0.12	b.d	0.13	0.13	0.38	0.50
NiO	0.37	0.24	0.39	0.31	0.10	0.11	0.11	0.03
MgO	51.65	49.88	51.66	53.57	36.15	35.61	13.90	11.87
CaO	0.03	0.04	0.04	b.d	0.42	0.75	b.d.	b.d.
Na_2O	0.02	0.02	0.03	b.d	0.09	0.13	0.02	0.02
K_2O	b.d.	b.d.	b.d.	b.d	b.d.	b.d.	b.d.	b.d.
Total	100.91	100.78	100.52	100.27	99.30	100.20	101.85	101.61
Mg-Num	92.1	89.7	92.4	95.3	93.7	92.8	63.6	54.4

core being higher in Cr_2O_3, MgO and NiO and the rim higher in FeO. The Al_2O_3 and TiO_2 concentrations are constant from core to rim.

Clinopyroxene was not observed in any of the garnets.

2.5.3. Inclusions in diamond

Two inclusions were recovered from diamonds DGD03 and DGD12. The inclusion from DGD03 decomposed under the electron beam and, therefore, is likely of epigenetic origin. From the diamond in sample DGD12, a single olivine crystal was recovered and analyzed. It is highly magnesian (Mg-number of 95.3), has 3100 ppm NiO and a CaO concentration below the minimum detection limit (<100 ppm; Table 2.3).

2.6. Garnet trace-element chemistry

2.6.1. Rare-earth element patterns

Three distinct C1-chondrite (McDonough and Sun 1995) normalized rare-earth element patterns (REE_N) of the host garnets are observed: (i) sinusoidal with a peak at Nd or Sm; (ii) humped patterns with broad maxima in the $MREE_N$; and (iii) patterns with positive $MREE_N$-$HREE_N$ slopes.

2.6.1.1. Sinusoidal patterns

Sinusoidal REE_N patterns are observed in 17 of the 21 microxenolith garnets. These patterns have positive slopes in $LREE_N$ increasing from subchondritic La to a peak at ~10 times chondritic abundance in either Nd or Sm followed by negative slopes to a trough at approximately chondritic concentrations at Er. The $HREE_N$ have positive slopes from Er to about 5 times chondritic concentrations at Lu (Figure 2.7a,b).

2.6.1.2. Humped patterns

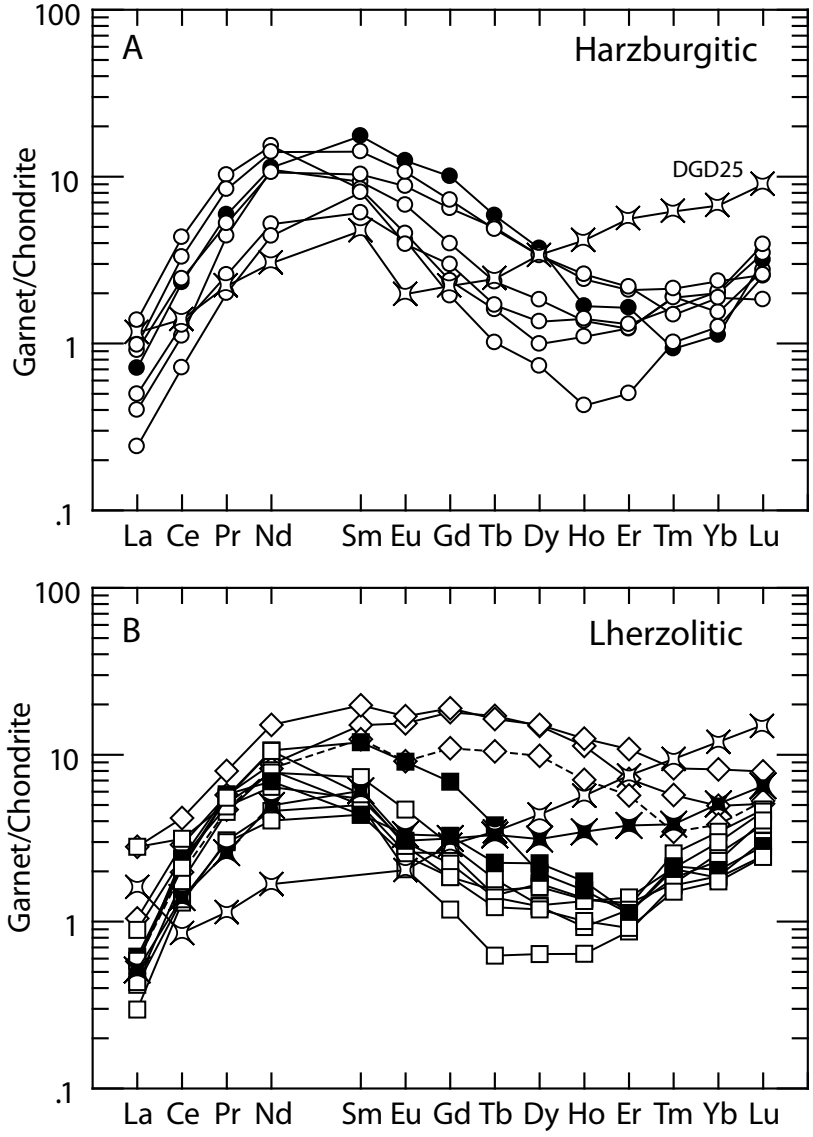

Figure 2.7: C1 chondrite normalized REE plots for the microxenolith garnets. A: Harzburgitic microxenoliths (except for DGD25) have sinusoidal REE_N patterns characteristic of harzburgitic garnet inclusions in diamonds worldwide (see Stachel et al. 2004 for review). B: Lherzolitic garnets have three different patterns. The most commonly occurring pattern is sinusoidal, overlapping with the harzburgitic garnets in shape and REE_N concentration. Three lherzolitic garnets have humped patterns shown with diamond-shaped symbols. One of these garnets (DGD19) has a positive slope in the $HREE_N$ and is shown with a dotted line. The garnets with humped patterns are also enriched in Ti, Zr, and Y suggestive of high-temperature (melt) metasomatism. One harzburgitic and two lherzolitic garnets ('x' shaped symbols) have a near linear increase in REE_N from Eu to Lu. C1 chondrite composition after McDonough and Sun (1995).

This group consists of three lherzolitic garnets (including the high-TiO_2 sample DGD13). The patterns have positive slopes in the $LREE_N$ to Nd followed by a plateau from Sm to Dy and overall negative slopes in the $HREE_N$ (Figure 2.7b). For garnet DGD19, a positive slope is observed in the $HREE_N$ (Tm-Lu).

2.6.1.3. Sloped pattern

This pattern is observed for one harzburgitic (DGD25) and two lherzolitic garnets (DGD14 and DGD16). Samples DGD14 and DGD25 have positive slopes peaking at Sm (4x chondritic) followed by a drop to Eu (2x chondritic) and a positive slope through the $MREE_N$ and $HREE_N$ to Lu (10x chondritic abundance). Sample DGD16 has approximately La at twice the chondritic abundance and a negative slope to Ce followed by a positive slope through the $MREE_N$ and $HREE_N$ (Figure 2.7a,b).

2.7. Geothermobarometry

2.7.1. Mineral exchange thermobarometry

The coexistence of orthopyroxene with two of the host garnets allows for the calculation of equilibrium temperatures based on Fe-Mg exchange (Harley 1984) and pressures based on the Al concentration in coexisting orthopyroxene (Brey and Köhler 1990). Iterative calculations using these formulations on five analytical pairs gives an average of 940ºC and 3.9 GPa and 950ºC and 3.6 GPa for DGD02 and DGD03, respectively. Conditions for both samples are in the graphite stability field (Kennedy and Kennedy 1976), which is inconsistent with the presence of octahedral diamonds in both garnets.

Sample DGD02 also contained olivine; the pressure-temperature conditions for this sample calculated using Fe-Mg exchange between garnet and olivine (thermometer of O'Neill and Wood 1979; with corrections by O'Neill 1980) in combination with the Al-exchange barometer gives conditions within the diamond stability field (1090ºC and 4.8 GPa) and may indicate disequilibrium between the host garnet and the inclusions.

2.7.2. Single mineral thermobarometry

The equilibration temperature of a garnet peridotite xenolith can also be calculated using the Ni concentration of garnet (T_{Ni}), assuming that Ni in the mantle source was buffered by coexisting olivine. Two calibrations of the Ni-in-garnet thermometer have been proposed: an empirical calibration based on equilibration temperatures of natural peridotite samples calculated using conventional mineral exchange thermometers (Ryan et al. 1996; Griffin et al. 1998) and an experimental calibration (Canil 1999). Based on the experimental calibration, the samples equilibrated at 970 to 1070ºC. Assuming an average 38 mW/m^2 surface heat flow paleogeotherm for the central Slave craton (Grütter et al. 1999), the depth range sampled by the microxenoliths is between 145 to 170 km.

The Cr concentration of mantle garnet is a function of both the bulk rock Cr/Al ratio and the pressure at which the rock has equilibrated. Using the empirical Cr-in-garnet barometer of Grütter et al. (2006), the equilibration pressure of garnets coexisting with Mg-chromite can be calculated if the local geothermal gradient is known. Again assuming a 38 mW/m^2 model geotherm, the pressure of origin of four garnets with observed chromite inclusions can be calculated; pressure estimates for samples without observed spinel represent minimum values. The four chromite-bearing samples have equilibration pressures of 4.8, 3.6, 3.5, and 4.3 GPa (samples DGD05, 10, 14 and 18, respectively) equivalent to depths of 110-150 km. The minimum estimates for chromite-free garnets range from 2.4 to 5.9 GPa (Table 2.2). The equivalent range in minimum depth represented by all of the microxenoliths spans from 76 to 185 km with the majority falling between 100 to 150 km minimum depth.

2.8. Discussion

Peridotitic garnets recovered as inclusions in diamonds from the Central Slave craton, similar to other cratonic regions, are overwhelmingly of harzburgitic paragenesis (Chinn et al. 1998; Stachel et al. 2003; Donnelly et al. 2007). Comparing the composition

of inclusion and microxenolith garnets reveals a striking mismatch between predominantly harzburgitic environments of diamond formation (indicated by inclusions) and the predominantly lherzolitic diamond sources at the time of kimberlite eruption (indicated by the diamondiferous microxenoliths). This apparent contradiction could be reconciled in two ways. The first possibility is that the predominance of lherzolitic diamondiferous microxenoliths is fortuitous. The second possibility is that the diamonds originally formed in harzburgitic sources that have subsequently been modified by metasomatic processes. The lherzolitic microxenoliths would therefore represent the end products of metasomatic conversion of harzburgite into lherzolite (Stachel et al. 1998; Griffin et al. 1999c). To assess if the diamondiferous microxenoliths at Diavik represent the peridotitic diamond sources at this mine or if they are just a highly biased sample, the question of whether the diamonds in the microxenoliths are representative of the overall production at Diavik must be addressed first. If the diamonds are indeed are representative sample of the overall population, then the composition of the garnets in the microxenoliths becomes an important record of past depletion/re-enrichment events affecting the diamondiferous lithospheric mantle beneath the central Slave craton.

2.8.1. Origin of diamonds in the microxenoliths

Donnelly et al. (2007) noted that whereas the overall diamond population at Diavik is dominanted by sharp-edged octahedra, the smaller size fractions (<1.6 mm diameter) are dominated by dodecahedral morphologies. The high proportion of octahedral diamonds in our sample set is related to shielding against resorption in the kimberlitic magma by their garnet hosts. The observed restriction of dodecahedral resorption to exposed diamond surfaces (pseudohemimorphism) is evidence for such a shielding effect. Colourless crystals dominate the Diavik production (comprising 63% of the diamonds examined); brown colours are the next most common (23%) and yellow and pink diamonds are rare (Donnelly et al. 2007). Although not from a similarly large sample-set, the proportion of colourless and brown diamonds recovered from the microxenoliths is similar: 52% (13 diamonds)

are colourless and 28% (7 diamonds) are brown. In terms of their morphology and colour distribution, the diamonds from the microxenoliths are thus indistinguishable from the main diamond population at the Diavik mine.

There is complete overlap in nitrogen contents and aggregation states between the microxenolith diamonds and the Diavik production (Figure 2.4). The majority of Diavik diamonds studied have nitrogen contents between ~10 to 1000 atomic ppm and span the entire range of aggregation states from type IaA (poorly aggregated) to type IaB (fully aggregated) (Donnelly et al. 2007). The nitrogen aggregation state can be used as a geothermometer assuming that the crystallization age of the diamonds is known (Taylor et al. 1990; Leahy and Taylor 1997). If the Re-Os age of ~3.5 Ga measured for peridotitic sulphide inclusions in diamonds from the nearby Panda kimberlite (Ekati mine, Westerlund et al. 2006) equally applies to Diavik peridotitic diamonds, then the time-averaged mantle storage temperatures of the microxenolith diamonds can be calculated. The overlap in temperatures calculated for the Diavik inclusion-bearing diamonds (1040 to 1255ºC) and the microxenolith diamonds (1070 to 1230ºC) demonstrates that both sample sets were stored at a similar temperature range and hence are derived from a comparable depth range. Additionally, the carbon isotope compositions of the microxenolith diamonds largely fall within the narrow range as other peridotitic diamonds from Diavik. Therefore, we conclude that these two diamond subpopulations are derived from the same sources. Hence, the chemical composition of the diamondiferous microxenolith garnets is considered to represent the peridotitic diamond sources in the lithospheric mantle beneath the Diavik diamond mine.

Thomassot et al. (2007) described a suite of 59 diamonds from a single lherzolite xenolith (DO40) from the Cullinan (formerly Premier) mine. The diamonds show a range in $\delta^{13}C$ from -4.2 to -0.1‰ and a have nitrogen concentrations from 40 to 1430 ppm with aggregation states of 10 to 85 %B. The observed covariation in nitrogen concentration and aggregation state of these diamonds is consistent with a single stage of diamond formation

at essentially isothermal conditions of 1200 to 1225ºC (Thomassot et al. 2007). The lack of a systematic covariations in N content and aggregation state in the diamonds from Diavik microxenolith samples DGD06, DGD13, DGD18 and DGD27 suggests multiple diamond formation events either over an extended time period (billions of years) or during relaxation back to a local geotherm following a thermal perturbation. The difference in nitrogen aggregation characteristics for the two diamonds in DGD17, for example, may be modelled (after Taylor et al. 1990; Leahy and Taylor 1997) as one of the diamonds forming earlier, during a thermal pulse, and residing for about 30 Ma at temperatures of 1300°C (or 170 Ma at 1250°C) before formation of the second diamond occurred after which both resided for another 3.4 Ga at constant temperature of about 1110-1120°C. Assuming that no thermal pulse occurred, the more highly aggregated nitrogen poor diamond could have resided in the mantle for 3.4 Ga at 1180°C, with the second diamond being rather young, requiring only 250 Ma mantle residence time at 1180°C.

2.8.2. Origin of high-Cr lherzolitic microxenoliths

The extraction of partial melts in the spinel stability field produces residues with a high Cr/Al ratio expressed as high Cr_2O_3 concentration in garnet (the major host of Cr in a harzburgite) when such residues are brought to high pressures into the garnet stability field (Stachel et al. 1998). Although the absolute Cr_2O_3 concentration (or Cr/Al ratio) of a garnet cannot be directly related to the percent of melt extraction from the protolith, garnets from relatively less depleted peridotite sources (lherzolites) generally will have lower Cr-numbers than garnets from sources that have been depleted to a greater degree (i.e. clinopyroxene-free residues – harzburgite; Grütter et al. 1999). Griffin et al. (1999b) showed that Cr in garnet may be successfully employed to predict the major-element composition of cratonic peridotite xenoliths, despite the inherent inaccuracy introduced through the pressure dependence of Cr in garnet in spinel bearing garnet peridotites. The association of high garnet Cr-numbers and greater relative degree of depletion is unaffected by the choice of model for the origin of subcratonic lithospheric mantle. Because bulk rock Cr-numbers are

considered to be relatively robust against secondary modification and generally expected to be lowered rather than raised during metasomatic overprint (introduction of Al rather than Cr), a comparison of garnet Cr-numbers from metasomatized and unmodified lherzolites and harzburgites can be used to assess the overall degree of initial depletion.

The lherzolitic microxenolith garnets, in general, have higher Cr-numbers than lherzolitic garnet inclusions in Diavik diamonds (Figure 2.8a and b) but overlap with the harzburgitic inclusions (Figure 2.8c). Because diamond isolates its inclusions from the surroundings, the composition of lherzolitic and harzburgitic garnet inclusions is representative of the original diamond source rocks without the effects of later metasomatic re-enrichment. The higher Cr-number of the lherzolitic microxenolith garnets compared with the lherzolitic inclusion garnets, therefore, indicates a greater degree of initial depletion for the residual peridotite represented by the microxenoliths. This is consistent with the observed overlap in Cr-number between harzburgitic garnets from microxenoliths and diamonds. Thus, we suggest that the lherzolitic microxenolith originally formed as residual harzburgites that only subsequently, following diamond formation, were partially converted to lherzolite.

Compared to our worldwide database, the lherzolitic microxenoliths from Diavik have higher Cr_2O_3 concentrations than lherzolitic garnets from diamond-bearing xenoliths from the Kaapvaal and Yakutian cratons (Figure 2.9). One diamond from a lherzolite xenolith (DO40) from the Cullinan/Premier mine, Kaapvaal craton, also has lherzolitic inclusions (a green clinopyroxene coexisting with a red garnet and an unidentified colourless mineral) documenting diamond crystallisation in relatively undepleted lherzolite for this locality (Viljoen et al. 2004). The higher Cr-number of garnets from the Diavik microxenoliths indicates a greater degree of initial depletion relative to diamondiferous lherzolites from other worldwide sources. The Cr-numbers of garnets from diamondiferous harzburgite xenoliths worldwide, however, overlap with the Diavik lherzolitic microxenoliths, suggesting similar degrees of initial depletion. This evidence also supports the model that

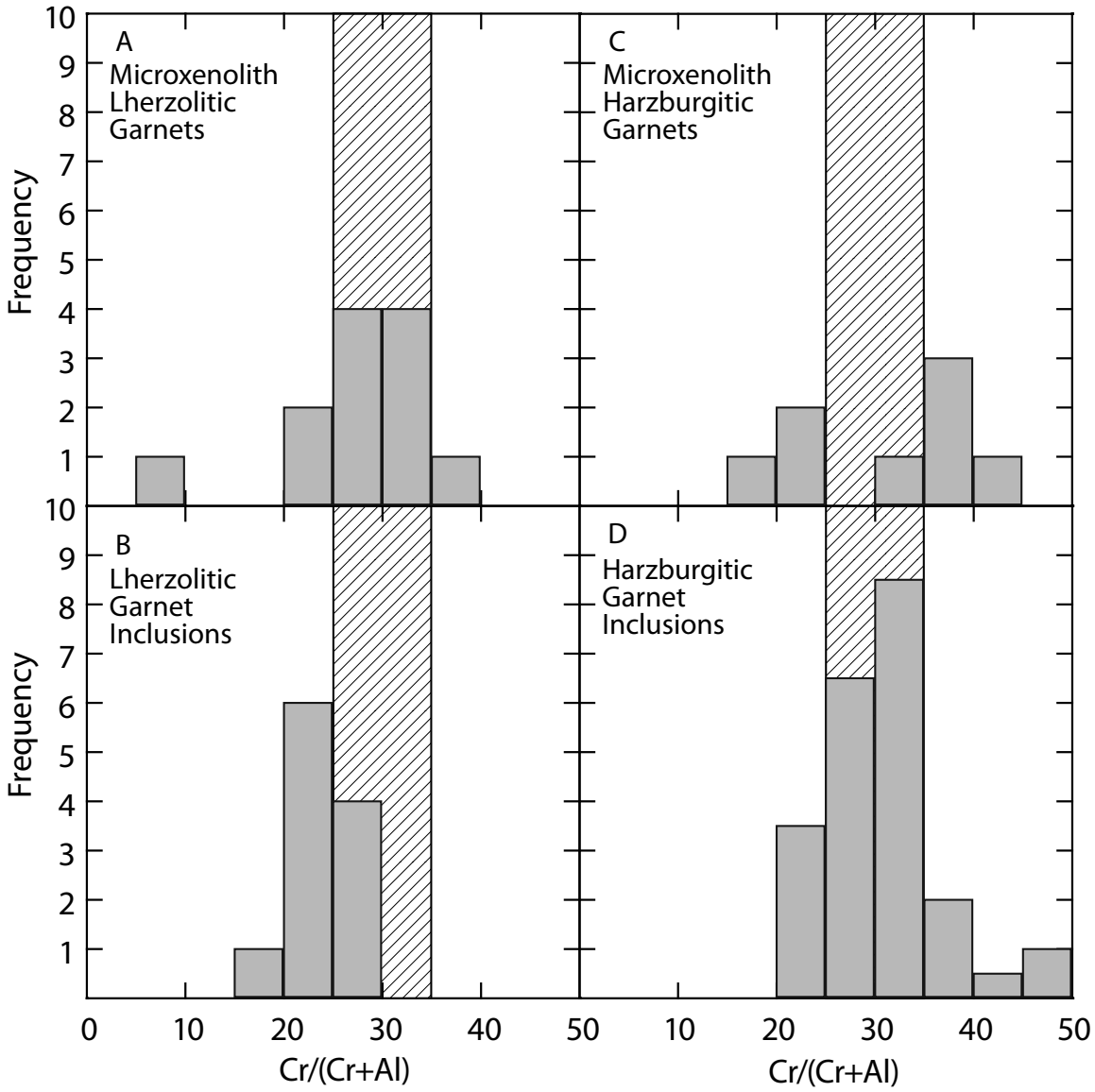

Figure 2.8: Histograms of garnet Cr-numbers (molar Cr/[Cr+Al]) for diamond-related peridotitic garnets from the Slave craton. A: the distribution for lherzolitic microxenolith garnets; B: lherzolitic garnet inclusions; C: harzburgitic microxenolith garnets; D: harzburgitic garnet inclusions. Note the overlap in modes between the *lherzolitic* microxenoliths (hachured region) and the *harzburgitic* inclusions, suggesting a similar Cr/Al ratio in the bulk rocks.

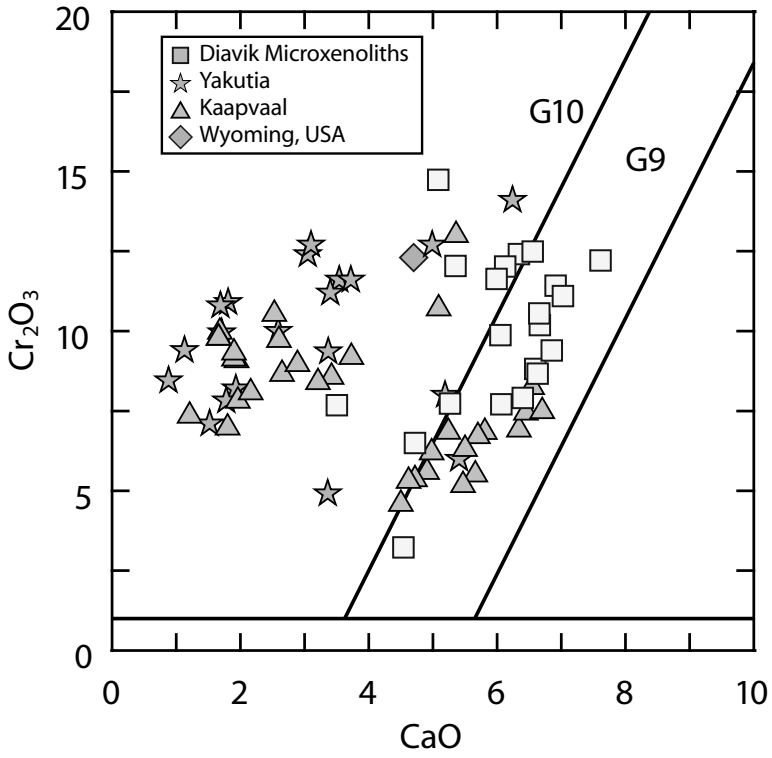

Figure 2.9: Cr_2O_3-CaO plot of garnets from diamondiferous peridotite xenoliths worldwide (Diavik: square symbols, Yakutia: stars, Kaapvaal: triangles, and Wyoming, U.S.A.: diamond). The Diavik lherzolitic microxenoliths are notably higher in Cr_2O_3 concentration compared with other garnets from diamondiferous lherzolites. Garnets from diamondiferous harzburgites from the Kaapvaal and Yakutian cratons have Cr_2O_3 concentrations overlapping with the Diavik microxenolith garnets. Data sources are referenced in the text.

the diamondiferous microxenoliths at Diavik represent originally harzburgitic sources.

2.8.3. Metasomatic processes in the Lac de Gras lithospheric mantle

2.8.3.1. Re-enrichment in major-elements

Peridotitic garnets found as inclusions in diamonds typically have high Cr and low Ca concentrations, indicative of derivation from depleted mantle peridotite (harzburgite) and the diamond potential of peridotitic mantle has been related to the abundance of such subcalcic, Cr-rich garnets in mineral concentrate (Gurney 1984). Diamond inclusion garnets from the Ekati and Diavik mines are generally consistent with this observation, although they are not as Ca-depleted as observed for some harzburgitic garnet inclusions from

Kaapvaal diamonds, in particular from the Kimberley area (Stachel et al. 2003; Donnelly et al. 2007). The overall depleted major-element signature (i.e. high Cr-number) of the microxenolith garnets is inconsistent with their generally relatively high concentrations of Ca, reflected in a predominantly lherzolitic character of the microxenolith. This suggests influx of a calcic metasomatic fluid that resulted in the partial conversion of harzburgite to lherzolite without affecting the bulk rock Cr/Al ratio.

Metasomatic conversion of harzburgitic to lherzolitic sources has been suggested for at least three localities in the Kaapvaal craton. Schulze (1995), in an investigation of low-Ca garnet harzburgites from Kimberley (mainly from the Bultfontein mine, South Africa), identified four types of core-rim zonations in inhomogeneous garnets. In every case, the zoning resulted in an increase of Ca towards the garnet rims. Burgess and Harte (1999; 2004) described five types of core-rim chemical variation patterns in zoned garnets from peridotite xenoliths from the Jagersfontein mine. Three of the patterns (their Type Ia, Ib, and Type II) involve compositional variations of lherzolitic garnets without changes in paragenesis. Their types IIIa and IIIb zoning patterns, however, indicate metasomatism resulting in the conversion of harzburgitic (G10) to lherzolitic (G9) garnets. A similar process was suggested by Griffin et al. (1999c) to explain zoning in garnets from the Wesselton kimberlite.

During storage at mantle temperatures such Ca zonation patterns are, however, short lived. Based on composition-corrected diffusivities (Carlson 2006), Ca-zoning would have persisted in the Diavik microxenolith garnets for less than 3 million years after a metasomatic event for storage conditions of 1100°C and 4.5 GPa. Absence of zonations in the microxenolith garnets, therefore, is consistent with metasomatic conversion of harzburgite to lherzolite and merely requires that this conversion did not take place penecontemporaneous to kimberlite emplacement. Garnets included in diamonds pre-dating the metasomatism would retain the depleted (i.e. harzburgitic) signature of the

original protolith while the host peridotite is converted to lherzolite (Schulze 1995).

The olivine inclusion recovered from diamond DGD12 has an Mg-number of 95.3 consistent with derivation from an extremely depleted peridotite, possibly a dunite (Bernstein et al. 2007). If the olivine inclusion in the diamond and the host garnet from DGD12 represented equilibrium conditions then the paragenesis last equilibrated at 680ºC (based on Mg-Fe exchange thermometry), which obviously is unreasonable. An olivine in equilibrium with the garnet from DGD12 at 1040ºC (the T_{Ni} for this garnet) would have an Mg-number of 92.3. This very large discrepancy (Fo 95.3 versus 92.3) clearly supports re-fertilization of a depleted source rock following diamond crystallization.

2.8.3.2. Metasomatic processes revealed in trace-elements

Sinusoidal REE_N are the most commonly observed patterns for peridotitic garnet inclusions in diamond. This type of pattern is interpreted as evidence for depletion followed by metasomatism by a highly fractionated (high LREE/HREE) fluid that may be related to diamond formation (Stachel et al. 2004). Peridotitic garnet inclusions from Diavik diamonds (Donnelly et al. 2007) and 17 of the microxenolith garnets have sinusoidal patterns. Although the predominance of sinusoidal REE_N patterns in the microxenolith garnets does not preclude the further episodes of metasomatism following diamond formation, it does suggest that the microxenoliths experienced an early history of depletion and re-enrichment similar to the garnets included in diamond.

The three lherzolitic garnets with humped REE_N patterns indicate that a second type of metasomatism affected some of the diamondiferous Central Slave lithospheric mantle. The transition from LREE-enriched sinusoidal to more $MREE_N$-rich garnet patterns has been attributed to a shift from fluid-dominated to melt-dominated metasomatism (Stachel et al. 1998). The garnets with humped REE_N patterns also have increased Ti, Y and Zr concentrations, consistent with melt metasomatism (Figure 2.10). T_{Ni} for these garnets is not elevated relative to the other samples. Thus, any evidence for possible heating associated with the passage of melts was lost due to subsequent re-equilibration at ambient mantle

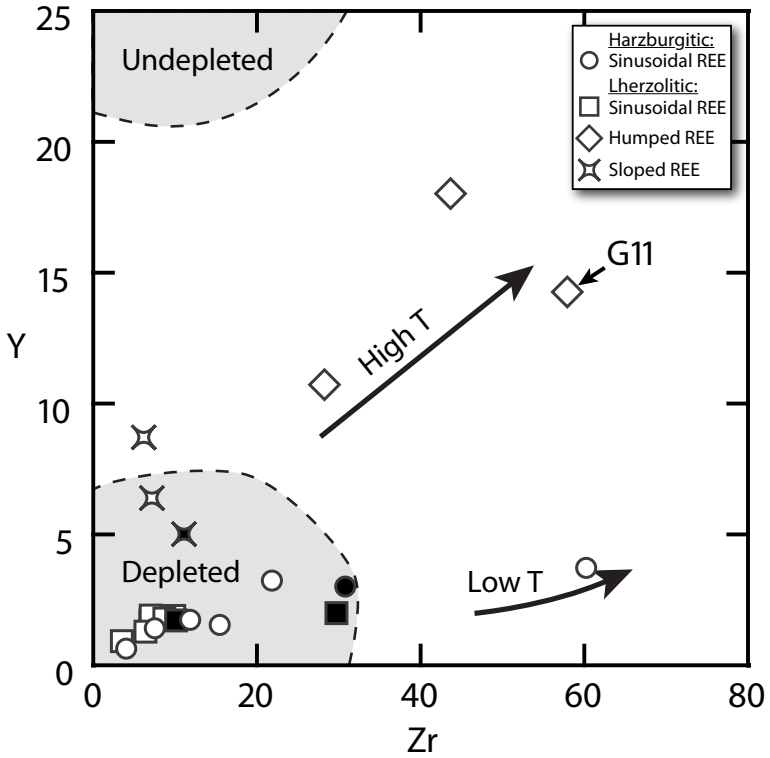

Figure 2.10: Y- Zr plot of the microxenolith garnets, the symbols relate to the REE_N patterns shown in Figure 2.7. Fields and metasomatism trends are from Griffin et al. (1999c).

conditions.

The garnets with positive slopes in the $MREE_N$-$HREE_N$ exhibit a third style of metasomatism by a medium with fairly unfractionated MREE/HREE. These samples follow a trend of enrichment in Y but not in Zr that extends from the 'depleted' field towards the 'undepleted' field on a Y-Zr plot (Figure 2.10). Sample DGD16 has a spike at La to approximately twice the chondritic concentration that indicates an additional metasomatic pulse by a highly fractionated LREE-rich fluid.

The absence of 'normal' REE_N patterns (i.e. positive slopes in $LREE_N$ and flat slopes from $MREE_N$ to $HREE_N$), indicative of more intense melt metasomatism (e.g. Stachel and Harris 1997), in any of the microxenolith garnets indicates that generally metasomatism of the diamondiferous mantle beneath Diavik has not been driven by melts that could presumably destroy diamonds (*cf.* McCammon et al. 2001).

2.9. Conclusions

Diamondiferous peridotite microxenoliths from the Diavik Diamond Mine provide an important sample suite revealing a complex metasomatic history of diamond-bearing mantle in the central Slave craton. The physical and chemical characteristics of the microxenolith diamonds indicate that they are typical samples from the overall Diavik production and not derived from a single diamond-rich layer with unique properties.

The microxenolith garnets record a primary stage of depletion that is consistent with formation of a high Cr/Al harzburgitic residue that is, in part, still spinel saturated after transport into the garnet stability field. It is in this environment that diamonds are likely to have formed, possibly synchronously with the infiltration of metasomatic fluids/melts. During the time interval from initial diamond formation at ~3.5 Ga (Westerlund et al. 2006) up to possibly only a few million years before kimberlite eruption at 55 Ma (Heaman et al. 2004 and references therein) metasomatic events have altered the lithospheric mantle beneath the central Slave craton via infiltration of Ca-rich fluids/melts. Evidence for Ca-rich fluids/brines is documented in fluid micro-inclusions in a diamond from Diavik (Klein-BenDavid et al. 2004). In some instances metasomatism converted diamondiferous harzburgite into lherzolite, reflected in the high ratio of lherzolitic to harzburgitic microxenoliths. The proportion of sharp-edged octahedra in the Diavik diamond production indicates that the metasomatism converting harzburgite to lherzolite was non-destructive to pre-existing diamonds. This is consistent with the predominance of sinusoidal REE_N patterns and overall low Y and Zr concentrations, which suggest an overall mild, fluid-dominated style of metasomatic re-enrichment.

The evidence for a secular evolution in the composition of the subcratonic lithospheric mantle presented here likely is not unique to the central Slave Craton. Widespread metasomatic re-enrichment of Archean cratonic roots with conversion of harzburgite to lherzolite may explain the apparent mismatch between evidence for highly depleted harzburgitic-dunitic lithospheric mantle during Archean craton formation (e.g. Ringwood

1991; Walter 1999; Bernstein et al. 2007) and the predominance of lherzolitic xenoliths and xenocrysts in Phanerozoic kimberlites (e.g. Schulze 1995; Griffin et al. 2003).

References

Aulbach S, Griffin WL, Pearson NJ, O'Reilly SY, Doyle BJ (2007) Lithosphere formation in the central Slave Craton (Canada): plume subcretion or lithosphere accretion. Contrib Mineral Petrol 154:409-427

Bernstein S, Kelemen PB, Hanghøj K (2007) Consistent olivine Mg# in cratonic mantle reflects Archean mantle melting to the exhaustion of orthopyroxene. Geology 35:459-462

Bleeker W, Davis WJ (1999) The 1991-1996 NATMAP Slave province project: Introduction. Can J Earth Sci 36:1033-1042

Boyd SR, Kiflawi I, Woods GS (1994) The relationship between infrared absorption and the A defect concentration in diamond. Philos Mag B 69:1149-1153

Boyd SR, Kiflawi I, Woods GS (1995) Infrared absorption by the B nitrogen aggregate in diamond. Philos Mag B 72:351-361

Brey GP, Köhler T (1990) Geothermobarmetry in four-phase lherzolites II. New thermometers, and practical assessment of existing thermobarometers. J Petrol 31:1353-1378

Bulatov V, Brey G, Foley S (1991) Origin of low-Ca, high-Cr garnets by recrystallization of low-pressure harzburgites. 5th Int Kimb Conf Ext Abstr, pp 29–31

Burgess SR, Harte B (1999) Tracing Lithosphere evolution through the analysis of heterogeneous G9/G10 garnets in peridotite xenoliths, I: Major element chemistry. In: Gurney JJ, Gurney JL, Pascoe MD, Richardson SH (eds) Proceedings of the 7th International Kimberlite Conference. Red Roof Design, Cape Town, South Africa, pp 66-80

Burgess SR, Harte B (2004) Tracing Lithosphere Evolution through the Analysis of Heterogeneous G9-G10 Garnets in Peridotite Xenoliths, II: REE Chemistry. J Petrol 45:609-633

Canil D (1999) The Ni-in-garnet geothermometer: calibration at natural abundances. Contrib Mineral Petrol 136:240-246

Carlson W (2006) Rates of Fe, Mg, Mn, and Ca diffusion in garnet. Am Min 91:1-11

Chinn IL, Gurney JJ, Kyser KT (1998) Diamonds and mineral inclusions from the NWT, Canada. 7th International Kimberlite Conference Extended Abstracts, Addendum. Cape Town, 4p

Daniels LRM, Richardson SH, Menzies AH, de Bruin D, Gurney JJ (1995) Diamondiferous garnet macrocrysts in the Newlands kimberlite, South Africa - Rosettta stones from

the Kaapvaal craton keel. 6th International Kimberlite Conference Extended Abstracts, pp 121-123

Dawson JB, Smith JV (1975) Occurrence of diamond in a mica-garnet lherzolite xenolith from kimberlite. Nature 254:580-581

de Wit MJ (1998) On Archean granites, greenstones, cratons and tectonics: does the evidence demand a verdict? Precambrain Res 91:181-226

Deines P (2002) The carbon isotope geochemistry of mantle xenoliths. Earth Sci Rev 58:247-278

Donnelly CL, Stachel T, Creighton S, Muehlenbachs K, Whiteford S (2007) Diamonds and their Mineral Inclusions from the A154 South pipe, Diavik Diamond Mine, Northwest Territories, Canada. Lithos In Press. doi:10.1016/j.lithos.2007.03.003

Griffin WL, Cousens DR, Ryan CG, Sie SH, Suter GF (1998) Ni in chrome pyrope garnets: a new geothermometer. Contrib Mineral Petrol 103:199-202

Griffin WL, Doyle BJ, Ryan CG, Pearson NJ, O'Reilly SY, Davies R, Kivi K, Van Achterbergh E, Natapov LM (1999a) Layered mantle lithosphere in the Lac de Gras area, Slave Craton: Composition, structure and origin. J Petrol 40:705-727

Griffin WL, O'Reilly SY, Ryan CG (1999b) The composition and origin of sub-continental lithospheric mantle. In: Boyd FR, Fei Y, Bertka CM, Mysen BO (eds) Mantle petrology : field observations and high-pressure experimentation: a tribute to Francis R. (Joe) Boyd, Geochemical Society, Houston, pp 13-45

Griffin WL, Shee SR, Ryan CG, Win TT, Wyatt BA (1999c) Harzburgite to lherzolite and back again: metasomatic processes in ultramafic xenoliths from the Wesselton kimberlite, Kimberly, South Africa. Contrib Mineral Petrol 134:232-250

Griffin WL, O'Reilly SY, Natapov LM, Ryan CG (2003) The evolution of lithospheric mantle beneath the Kalahari Craton and its margins. Lithos 71:215-241

Grütter H, Apter DB, Kong J (1999) Crust-Mantle Coupling: Evidence from Mantle-Derived Xenocrystic Garnets. In: Gurney JJ, Gurney JL, Pascoe MD, Richardson SH (eds) Proceedings of the 7th International Kimberlite Conference. Red Roof Design, Cape Town, South Africa, pp 307-313

Grütter HS, Gurney JJ, Menzies AH, Winter F (2004) An updated classification scheme for mantle-derived garnet, for use by diamond explorers. Lithos 77:841-857

Grütter H, Latti D, Menzies A (2006) Cr-saturation arrays in concentrate garnet compositions from kimberlite and their use in mantle barometry. J Petrol 47:801-820

Gurney JJ, Switzer GS (1973) The discovery of garnets closely related to diamonds in the Finsch pipe, South Africa. Contrib Mineral Petrol 39:103-116

Gurney JJ (1984) A correlation between garnets and diamonds in kimberlites. In: Glover JE, Harris PG (eds) Kimberlite occurrence and origins: a basis for conceptual models in exploration, Publication 8. Geology Department and University Extension, University of Western Australia, pp 143-166

Harley SL (1984) An experimental study of the partitioning of Fe and Mg between garnet and orthopyroxene. Contrib Mineral Petrol 86:359-373

Harris JW (1992) Diamond Geology. In: Field JE (ed) The properties of natural and synthetic diamond, Academic Press, London, pp 345-393

Heaman LM, Kjarsgaard BA, Creaser RA (2004) The Temporal Evolution of North American Kimberlites. Lithos 76:377-397

Helmstaedt H, Schulze DJ (1989) Southern African kimberlites and their mantle sample: implications for Archaean tectonics and lithosphere evolution. Spec Pub Geol Soc Au 14:358-368

Jaques AL, O'Neill HSC, Smith CB, Moon J, Chappell BW (1990) Diamondiferous peridotite xenoliths from the Argyle (AK1) lamproite pipe, Western Australia. Contrib Mineral Petrol 104:255-276

Kennedy CS, Kennedy GC (1976) The equilibrium boundary between graphite and diamond. J Geophys Res 81:2467-2470

Klein-BenDavid O, Izraeli ES, Hauri E, Navon O (2004) Mantle fluid evolution--A tale of one diamond. Lithos 77:243-253

Leahy K, Taylor WR (1997) The influence of the Glennie domain deep structure on the diamonds in the Saskatchewan kimberlites. Geol Geofiz 38:451-460

McCallum ME, Eggler DH (1976) Diamonds in an Upper Mantle Peridotite Nodule from Kimberlite in Southern Wyoming. Science 192:253-256

McCammon CA, Griffin WL, Shee SR, O'Neill HSC (2001) Oxidation during metasomatism in ultramafic xenoliths from the Wesselton kimberlite, South Africa: implications for the survival of diamond. Contrib Mineral Petrol 141:287-296

McDonough WF, Sun SS (1995) The Composition of the Earth. Chem Geol 120:223-253

Menzies A, Carlson RW, Shirey SB, Gurney JJ (1999) Re-Os Systematics of Newlands Peridotite Xenoliths: Implications for Diamond and Lithosphere Formation. In: Gurney JJ, Gurney JL, Pascoe MD, Richardson SH (eds) Proceedings of the 7th

International Kimberlite Conference. Red Roof Design, Cape Town, South Africa, pp 566-573

O'Neill HSC, Wood BJ (1979) An experimental study of Fe-Mg partitioning between garnet and olivine and its calibration as a geothermometer. Contrib Mineral Petrol 70:59-70

O'Neill HSC (1980) An experimental study of Fe-Mg partitioning between garnet and olivine and its calibration as a geothermometer: Corrections. Contrib Mineral Petrol 72:337

Richardson S, Gurney J, Erlank A, Harris J (1984) Origin of diamonds in old enriched mantle. Nature 310:198-202

Ringwood AE (1991) Phase transformations and their bearing on the constitution and dynamics of the mantle. Geochim Cosmochim Acta 55:2083-2110

Robinson DN (1979) Surface textures and other features of diamonds. University of Cape Town, Unpubl PhD

Ryan CG, Griffin WL, Pearson NJ (1996) Garnet geotherms: Pressure-temperature data from Cr-pyrope garnet xenocrysts in volcanic rocks. J Geophys Res 101:5611-5625

Schulze D (1986) Calcium anomalies in the mantle and a subducted metaserpentinite origin for diamonds. Nature 319:483-485

Schulze D (1995) Low-Ca garnet harzburgites from Kimberley, South Africa: Abundance and bearing on the structure and evolution of the lithosphere. J Geophys Res 100:12513-12526

Shee SR, Gurney JJ, Robinson DN (1982) Two diamond-bearing peridotite xenoliths from the Finsch kimberlite, South Africa. Contrib Mineral Petrol 81:79-87

Sobolev NV (1974) Deep-seated inclusions in kimberlites and the problem of the composition of the upper mantle, American Geophysical Union, Washington, D.C., p 279

Sobolev NV, Pokhilenko NP, Efimova ES (1984) Diamond-bearing peridotite xenoliths in kimberlites and the problem of the origin of diamonds. Rus Geol Geophys 25:63-80

Stachel T, Harris JW (1997) Diamond precipitation and mantle metasomatism - evidence from the trace element chemistry of silicate inclusions in diamonds from Akwatia, Ghana. Contrib Mineral Petrol 129:143-154

Stachel T, Viljoen F, Brey GP, Harris JW (1998) Metasomatic processes in lherzolitic and harzburgitic domains of diamondiferous lithospheric mantle: REE in garnets from xenoliths and inclusions in diamonds. Earth Planet Sci Lett 159:1-12

Stachel T, Harris JW, Tappert R, Brey GP (2003) Peridotitic diamonds from the Slave and the Kaapvaal cratons - similarities and differences based on a preliminary data set. Lithos 71:489-503

Stachel T, Aulbach S, Brey GP, Harris JW, Leost I, Tappert R, Viljoen KS (2004) The trace element composition of silicate inclusions in diamonds: a review. Lithos 77:1-19

Taylor WR, Jaques AL, Ridd M (1990) Nitrogen-defect aggregation characteristics of some Australasian diamonds: time-temperature constraints on the source regions of pipe and alluvial diamonds. Am Min 75:1290-1310

Thomassot E, Cartigny P, Harris JW, (Fanus) Viljoen KS (2007) Methane-related diamond crystallization in the Earth's mantle: Stable isotope evidences from a single diamond-bearing xenolith. Earth Planet Sci Lett 257:362-371

Viljoen KS, Swash PM, Otter ML, Schulze DJ, Lawless PJ (1992) Diamondiferous garnet harzburgites from the Finsch kimberlite, Northern Cape, South Africa. Contrib Mineral Petrol 110:133-138

Viljoen F, Robinson DN, Swash PM, Griffin WL, Otter ML, Ryan CG, Win TT (1994) Diamond- and graphite-bearing peridotite xenoliths from the Roberts Victor kimberlite, South Africa. In: Meyers HOA, Leonardos OH (eds) Proceedings of the 5th International Kimberlite Conference. Companhia de Pesquisa de Recursos Minerais, pp 285-303

Viljoen KSF, Dobbe R, Smit B, Thomassot E, Cartigny P (2004) Petrology and geochemistry of a diamondiferous lherzolite from the Premier diamond mine, South Africa. Lithos 77:539-552

Walter MJ (1999) Melting residues of fertile peridotite and the origin of cratonic lithosphere. In: Boyd FR, Fei Y, Bertka CM, Mysen BO (eds) Mantle petrology: field observations and high-pressure experimentation: a tribute to Francis R. (Joe) Boyd, Geochemical Society, Houston, pp 225-239

Westerlund KJ, Shirey SB, Richardson SH, Carlson RW, Gurney JJ, Harris JW (2006) A subduction wedge origin for Paleoarchean peridotitic diamonds and harzburgites from the Panda kimberlite, Slave craton: evidence from Re-Os isotope systematics. Contrib Mineral Petrol 152:275-294

Chapter 3: Oxidation of the Kaapvaal lithospheric mantle driven by metasomatism[1]

3.1. Introduction

The stabilities of native carbon (as either diamond or graphite), carbonate and hydrous phases in the mantle are determined by the prevailing oxidation state, monitored by oxygen fugacity (fO_2). The composition and speciation of a COH fluid is dictated by the ambient fO_2 conditions – under reducing conditions fluids are predicted to be predominantly CH_4-H_2O and at more oxidizing conditions CO_2-H_2O (e.g. French, 1966; Matveev et al., 1997). In the subcratonic lithospheric mantle, the stability of CO_2-rich fluid is complicated by silicate-CO_2 reactions that produce carbonates (e.g. Wyllie and Huang 1976). The fO_2 control on fluid speciation has direct bearing on the melting behaviour of the mantle. Taylor and Green (1989) described a scenario in which CH_4-dominated fluids, rising from reduced sublithospheric mantle, interact with relatively oxidized lithospheric peridotite precipitating elemental carbon and increasing the H_2O fugacity of the fluid. Melting would then commence if the wet solidus is exceeded. This 'redox melting' hypothesis requires that the asthenosphere, as the presumed major source of CH_4-rich mantle fluids, is more reducing than the overlying lithosphere. An alternative hypothesis suggests that the depleted lithosphere is more reduced than the deeper, more fertile asthenosphere (Haggerty and Tompkins 1983; Haggerty 1990). In this scenario, diamonds could form by the reduction of carbonate melts through interaction with the reduced lithosphere.

Studies of the shallow, spinel-bearing portion of the lithospheric mantle have revealed considerable heterogeneity with variations in oxygen fugacity caused by differing degrees of melt extraction (Bryndzia and Wood 1990; Woodland et al. 2006), tectonic setting (Wood et al. 1990; Ballhaus 1993), and metasomatism (e.g. McGuire et al. 1991; Ballhaus 1993).

1 A version of this chapter is published as Creighton S, Stachel T, Matveev S, Höfer HE, McCammon C, Luth RW (2009) Oxidation of the Kaapvaal lithospheric mantle driven by metasomatism. Contributions to Mineralogy and Petrology 157:491-504

Similar studies of the deeper, garnet-bearing portion of the lithospheric mantle are notably fewer. This is caused, in part, by the limited thermochemical data for the garnet solid solutions present and the technical limitations of accurately measuring ferric iron concentrations in mantle garnets that are typically below 1 wt% Fe_2O_3. Luth et al. (1990) attempted to use the andradite component in garnet to formulate an oxybarometer for mantle peridotites. With thermochemical data on the hypothetical skiagite garnet end-member (Woodland and O'Neill 1993), Gudmundsson and Wood (1995) experimentally calibrated a more precise oxybarometer for garnet-bearing mantle peridotites based on the reaction:

$$\underset{\text{skiagite}}{2Fe_3^{2+}Fe_3^{3+}Si_3O_{12}} = \underset{\text{ferrosillite}}{Fe_2Si_2O_6} + \underset{\text{fayalite}}{4Fe_2SiO_4} + O_2 \qquad (3.1)$$

This garnet peridotite oxybarometer has been applied to determine the fO_2 conditions of last equilibration for peridotite xenoliths from Finland, South Africa, Lesotho, and northern Canada. The consensus that is emerging is that within the deeper portions of the lithospheric mantle, there is a general reduction with increasing depth (Woodland and Peltonen 1999; Woodland and Koch 2003; McCammon and Kopylova 2004), consistent with crystal chemical controls (e.g. Gudmundsson and Wood 1995), and that metasomatism may lead to an overall increase in oxidation of the affected mantle (McCammon et al. 2001). This study is the first to couple *in situ* ferric iron measurements at high spatial resolution and garnet trace-element geochemistry to elucidate the effects of metasomatism on the oxidation state of the lithospheric mantle.

3.2. Samples

Nineteen garnet peridotite xenoliths were investigated for this study from the Boshof Road dumps (Bultfontein kimberlite), Kimberley, South Africa (Figure 3.1). Xenoliths containing spinel rather than garnet were excluded because this study focused solely on the deeper portion of the lithospheric upper mantle. Samples included in this study

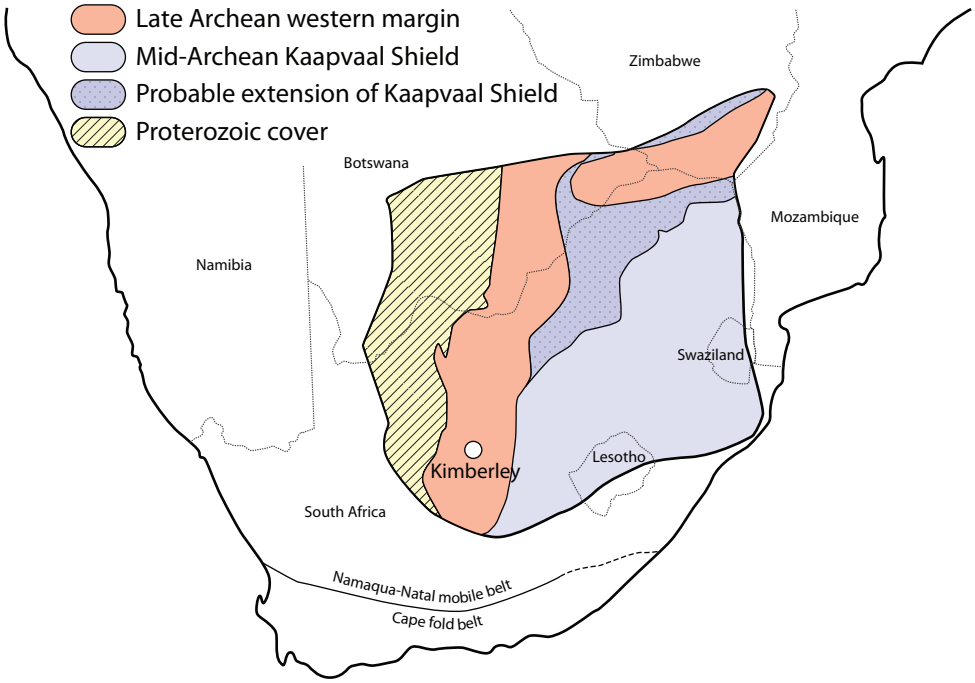

Figure 3.1: Map of southern Africa showing the location of the Kimberley kimberlites in South Africa. Craton boundaries and divisions are from de Wit et al. (1992).

were selected to represent a range of metasomatic re-enrichment from harzburgites and clinopyroxene-poor lherzolites to samples with evidence for modal metasomatism (e.g. abundant clinopyroxene and/or visible phlogopite). Sixteen samples have coarse textures and three are classified as mosaic-porphyroclastic, according to the terminology of Harte (1977). All of the samples show some evidence of alteration – variable serpentinization of olivine and kelyphyte rims on garnet. One sample (Bo-19) also contains spinel.

3.3. Analytical methods

The major- and minor-element concentrations of all minerals (Tables 3.1, 3.2, 3.3, 3.4) were measured using a JEOL JXA-8900 Superprobe with beam conditions set to 20 kV gun potential and 20 nA current. A combination of natural and synthetic mineral, oxide and metal standards were used to reduce counts to weight percent concentrations using the online CITZAF method. Precise analyses were obtained by setting count times from 30 to 60 seconds on each peak and half the peak count time on each background; detection limits from the average of at least 5 analyses are less than 100 ppm for all oxides except for P_2O_5

(250 ppm) and Na_2O (200 ppm).

Trace-element concentrations of the garnets were measured using a Perkin Elmer Elan 6000 quadrupole inductively coupled plasma mass spectrometer (ICP-MS) utilizing a Merchantek UP 213 UV laser ablation system. The analysis spot size was 160 μm diameter; averages of at least three spots are reported. Concentrations below the detection limits are indicated where appropriate (Table 3.5).

The ferric iron concentration of the garnets was determined using the flank method (Höfer et al. 1994; 2003) for measuring iron oxidation state with the electron microprobe. Based on Höfer and Brey (2007), we developed an analytical protocol specific for Fe-poor, mantle-derived pyropic garnets (for details see Appendix A). The accuracy of the flank method is demonstrated by comparing the $Fe^{3+}/\Sigma Fe$ of garnets measured using our modified protocol and using the Mössbauer 'milliprobe' (Figure 3.2). Propagated 1σ errors in $Fe^{3+}/\Sigma Fe$ are typically <0.01 and repeat analyses of the same garnet are within ± 0.008. Therefore, the 1σ error reported for the samples in this study is 0.008 or the statistical error if it is larger. Flank method measurements made with our modified protocol, therefore, can precisely measure the Fe^{3+} concentration of mantle-derived pyropic garnets with an accuracy comparable to Mössbauer spectroscopy. The flank method has dramatically improved spatial resolution compared to bulk Mössbauer and slightly improved spatial resolution compared to Mössbauer milliprobe; 20×20 μm compared to 50 μm diameter for the Mössbauer milliprobe.

3.4. Results

3.4.1. Mineral Chemistry

The xenolith garnets are pyropic and range in molar Mg-Number (100*Mg/[Mg+ΣFe]) from 81.4 to 87.1 (Table 3.1). Seventeen of the 19 garnets are lherzolitic and have Cr_2O_3 and CaO concentrations ranging from 2.26 to 6.51 and 4.39 to 6.06, respectively (Table 3.1). According to the classification scheme of Grütter et al. (2004), garnets from two

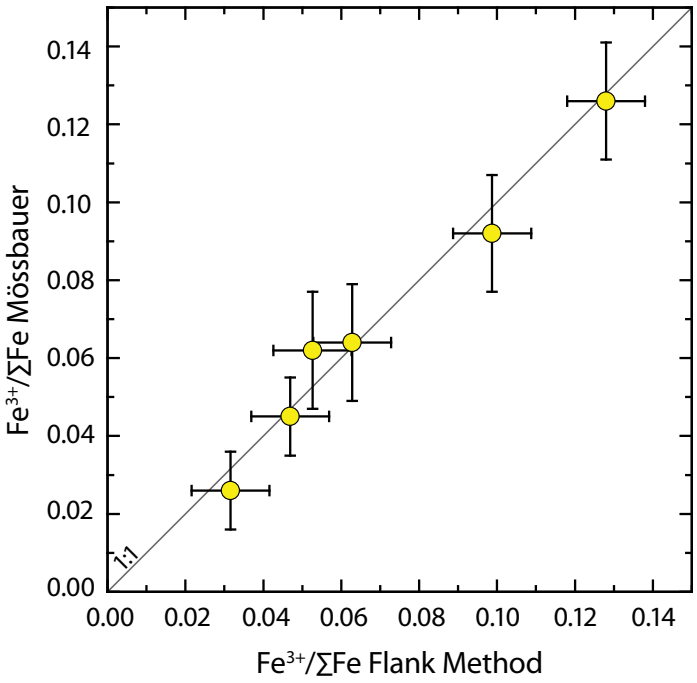

Figure 3.2: Comparison of $Fe^{3+}/\Sigma Fe$ measured by Mössbauer spectroscopy and using our modified version of the flank method. All samples plot along a 1:1 correlation line within their respective 1σ errors, demonstrating the accuracy of the technique. Details of the flank method are found in Höfer and Brey (2007); our modifications are outlined in the Appendix A.

xenoliths are classified as G10D and the rest are G9 (Figure 3.3). The strongly subcalcic garnets characteristic of inclusions in Kaapvaal diamonds (e.g. Gurney 1984; Stachel et al. 2003) are absent from this sample set. The garnet $Fe^{3+}/\Sigma Fe$ measured using the flank method ranges from 0.024 to 0.171, extending the range previously measured for Kimberley peridotitic garnets using Mössbauer spectroscopy (Luth et al. 1990; Canil and O'Neill 1996; McCammon et al. 2001; Woodland and Koch 2003), to both more oxidized and reduced values.

Olivine has a range in Mg-number from 90.5 to 93.4 (Table 3.2). One sample, Bo-13, a porphyroclastic lherzolite, has neoblastic olivine that is slightly more Fe-rich (Mg-number 92.7) than the porphyroclasts (93.4). Orthopyroxene in the xenoliths is comparably magnesian with Mg-numbers ranging from 91.7 to 94.2 (Table 3.3). The orthopyroxenes are relatively Cr-rich (0.21-0.41 wt.%) and Al- and Ti-poor (<0.82 wt.% Al_2O_3 and TiO_2 is below the detection limit for most analyses), Na_2O concentrations are <0.17 wt.%.

Table 3.1: Major-element concentration (wt%) and $Fe^{3+}/\Sigma Fe$ of the xenolith garnets measured using EPMA and the flank method, respectively. Garnet-olivine Fe-Mg exchange ($T_{O'Neill}$) and two-pyroxene (T_{BKN}) temperatures, orthopyroxene-garnet pressure (P_{BKN}) and $\Delta \log fO_2$ (FMQ) are also reported. Samples marked with an asterisk have a porphyroclastic texture. Concentrations below the detection limits (see text for details) are marked "b.d."

Sample	Bo-01	Bo-02	Bo-03	Bo-04	Bo-05	Bo-07	Bo-08*	Bo-10	Bo-12	Bo-13*
P_2O_5	0.02	0.05	0.06	0.07	0.02	0.06	0.03	0.05	0.03	b.d
SiO_2	41.68	41.90	42.02	41.44	41.93	42.07	42.23	41.93	41.70	41.13
TiO_2	0.06	b.d	b.d	0.02	0.07	b.d	0.33	0.03	0.03	b.d
Al_2O_3	21.91	20.65	21.25	20.00	21.95	20.65	21.88	20.19	19.26	20.28
Cr_2O_3	2.69	4.78	3.84	5.91	2.80	4.88	2.53	5.19	6.26	4.77
V_2O_3	b.d	0.02	0.03	0.03	b.d	0.02	0.03	0.03	0.04	0.03
Fe_2O_3	1.44	0.17	0.18	0.55	1.03	0.75	0.63	0.54	0.18	0.42
FeO	7.53	6.27	6.30	6.24	7.06	5.61	7.43	6.60	6.60	5.90
MnO	0.46	0.33	0.31	0.37	0.45	0.34	0.38	0.33	0.33	0.34
MgO	20.04	21.98	21.46	20.36	20.86	21.24	21.31	21.06	20.46	21.10
CaO	4.71	4.04	4.99	5.02	4.48	5.29	4.39	5.24	6.06	5.36
Na_2O	0.03	0.03	0.03	0.05	0.04	0.03	0.08	0.04	0.02	0.03
Total	100.57	100.23	100.47	100.05	100.70	100.94	101.26	101.24	100.98	99.35
$Fe^{3+}/\Sigma Fe$	0.147	0.024	0.025	0.073	0.116	0.107	0.071	0.069	0.024	0.060
1σ error	0.008	0.008	0.008	0.010	0.008	0.008	0.008	0.008	0.009	0.012
olivine a_{fa}	0.124	0.091	0.093	0.099	0.109	0.090	0.121	0.096	0.097	0.089
opx a_{fer}	0.078	0.057	0.060	0.062	0.069	0.057	0.081	0.065	0.062	0.057
$T_{O'Neill}$ (°C)	835	932	1025	903	824	971	1213	992	1042	970
P_{BKN} (GPa)	3.09	3.47	4.18	3.24	3.04	3.88	5.39	3.84	4.42	3.96
$\Delta \log fO_2$ (FMQ)	0.07	-3.13	-3.97	-1.22	-0.09	-1.32	-3.47	-1.73	-4.20	-2.23
T_{PBKN} (°C)	908	-	-	-	918	-	1179	-	-	1199
P_{BKN} (GPa)	3.55	-	-	-	3.61	-	5.16	-	-	5.30
$\Delta \log fO_2$ (FMQ)	-0.38	-	-	-	-0.63	-	-3.31	-	-	-3.15

Sample	Bo-14	Bo-17	Bo-18	Bo-19	Bo-20	Bo-21	Bo-26	Bo-27	Bo-30*
P_2O_5	0.05	0.08	0.04	b.d	0.06	0.06	b.d	0.06	0.07
SiO_2	41.97	41.15	41.68	42.00	41.06	40.96	40.80	41.10	40.76
TiO_2	0.07	0.04	0.02	0.04	0.03	b.d	0.05	0.02	0.05
Al_2O_3	21.46	18.66	20.36	20.94	18.93	20.41	22.30	21.14	19.42
Cr_2O_3	3.40	6.51	4.60	3.66	6.16	4.91	2.26	3.99	6.03
V_2O_3	b.d	0.03	0.03	0.02	0.02	0.02	b.d	0.02	0.03
Fe_2O_3	0.60	1.31	0.25	0.39	0.33	0.36	0.39	0.93	0.68
FeO	7.63	5.68	6.25	7.24	6.02	6.83	8.15	5.62	5.95
MnO	0.49	0.36	0.33	0.42	0.32	0.37	0.44	0.31	0.39
MgO	20.45	20.35	21.24	21.36	21.03	20.38	20.18	21.39	19.56
CaO	4.72	5.70	4.99	4.73	4.87	5.19	4.53	4.81	5.74
Na_2O	0.04	0.05	0.05	0.03	0.05	0.04	0.05	0.04	0.04
Total	100.86	99.92	99.84	100.82	98.88	99.54	99.13	99.44	98.71
$Fe^{3+}/\Sigma Fe$	0.066	0.171	0.034	0.046	0.047	0.045	0.042	0.130	0.093
1σ error	0.008	0.010	0.012	0.008	0.012	0.009	0.008	0.013	0.012
olivine a_{fa}	0.112	0.099	0.095	0.104	0.094	0.104	0.119	0.094	0.098
opx a_{fer}	0.071	0.079	0.061	0.066	0.060	0.065	0.075	0.060	0.068
$T_{O'Neill}$ (°C)	788	961	988	841	977	925	827	981	915
P_{BKN} (GPa)	2.71	4.05	3.74	2.94	3.46	3.39	3.04	3.67	3.33
$\Delta \log fO_2$ (FMQ)	-0.51	-1.02	-3.00	-1.39	-2.19	-2.12	-1.71	-0.86	-1.08
T_{PBKN} (°C)	939	-	1131	919	-	1078	924	-	1184
P_{BKN} (GPa)	3.62	-	4.55	3.39	-	4.29	3.62	-	4.81
$\Delta \log fO_2$ (FMQ)	-1.41	-	-3.60	-1.82	-	-2.85	-2.26	-	-2.19

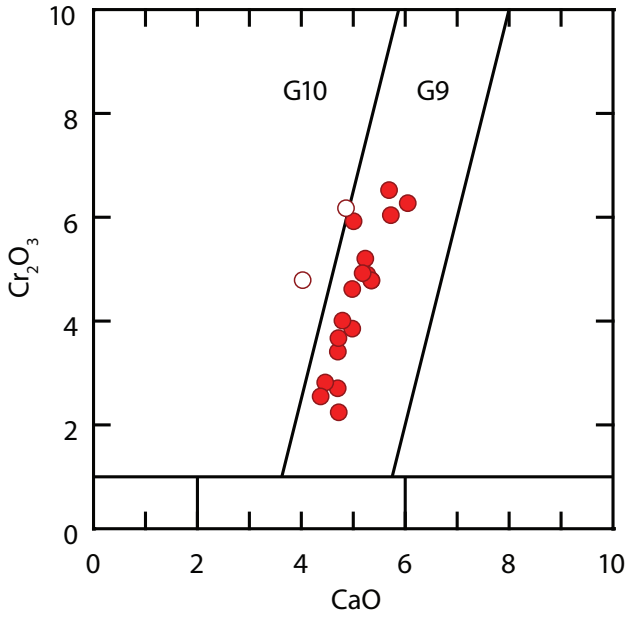

Figure 3.3: Classification of garnets on the CaO-Cr_2O_3 diagram of Grütter et al. (2004). The majority of the garnets classify as G9 (lherzolitic; filled symbols) and 2 are G10D (harzburgitic; open symbols).

Although the bulk of the xenoliths contain "lherzolitic" G9 garnets, modal clinopyroxene is not observed in all samples. The analyzed clinopyroxene is chromian diopside (Table 3.4) with Al_2O_3 and Cr_2O_3 concentrations typical of garnet-bearing cratonic lithospheric mantle (e.g. Ramsay and Tompkins 1994).

3.4.2. Trace-elements in garnet

Four different C1 chondrite normalized (REE_N) profiles are observed for the xenolith garnets: (i) sinusoidal; (ii) humped; (iii) sloped; and (iv) normal (Table 3.5). Sinusoidal patterns have steep positive slopes in the $LREE_N$ peaking at either Nd (circles in Figure 3.4a) or Sm (hexagons in Figure 3.4b) followed by a negative slope through the $MREE_N$ to minima at Er and a positive slope in the $HREE_N$ to Lu. Humped patterns have steep positive slopes through the $LREE_N$ from Ce to Sm, flat slopes from Sm to Tb at approximately 15× chrondritic abundance followed by negative slopes through the $HREE_N$ to 4-9× chrondritic Lu (squares in Figure 3.4a). Sloped patterns have variable positive slopes through the $LREE_N$ followed by constant positive slopes through the $MREE_N$ and $HREE_N$ to 10-20×

Table 3.2: Major-element concentration (wt%) of the xenolith olivine.

Sample	Bo-01	Bo-02	Bo-03	Bo-04	Bo-05	Bo-07	Bo-08	Bo-10	Bo-12	Bo-13
Mineral	olivine	olivine	olivine	olivine	olivine	olivine	olivine	olivine	olivine	olivine (nb)
P_2O_5	b.d.	b.d.	b.d.	b.d.	b.d.	b.d.	b.d.	b.d.	b.d.	b.d.
SiO_2	40.55	40.65	40.88	40.13	40.71	41.00	40.62	40.85	40.95	39.87
TiO_2	0.02	b.d.	b.d.	b.d.	0.02	b.d.	0.03	b.d.	b.d.	0.01
Al_2O_3	0.02	0.02	0.02	0.02	0.02	0.02	0.03	0.02	0.02	0.04
Cr_2O_3	0.01	0.02	0.01	0.02	0.00	0.01	0.02	0.02	0.02	0.01
V_2O_3	b.d.	b.d.	b.d.	b.d.	b.d.	b.d.	b.d.	b.d.	b.d.	b.d.
FeO	8.76	6.55	6.88	7.00	7.67	6.55	9.33	7.01	7.21	7.15
MnO	0.10	0.09	0.09	0.09	0.10	0.08	0.12	0.10	0.10	0.10
NiO	0.41	0.42	0.41	0.40	0.41	0.41	0.34	0.41	0.42	0.40
MgO	50.13	51.48	51.59	50.85	50.96	51.80	49.94	51.47	51.53	51.28
CaO	0.02	0.01	0.02	0.01	0.01	0.02	0.03	0.02	0.03	0.03
Na_2O	0.03	0.02	0.02	0.02	0.02	0.02	0.03	0.02	b.d.	0.03
K_2O	b.d.	b.d.	b.d.	b.d.	b.d.	b.d.	b.d.	b.d.	b.d.	b.d.
Total	100.05	99.28	99.93	98.56	99.93	99.93	100.49	99.93	100.31	98.94
Mg#	91.07	93.34	93.04	92.83	92.22	93.38	90.51	92.91	92.73	92.74

Sample	Bo-13	Bo-14	Bo-17	Bo-18	Bo-19	Bo-20	Bo-21	Bo-26	Bo-27	Bo-30
Mineral	olivine (pc)	olivine	olivine	olivine	olivine	olivine	olivine	olivine	olivine	olivine
P_2O_5	b.d.	b.d.	b.d.	b.d.	b.d.	b.d.	b.d.	0.00	0.01	0.01
SiO_2	40.81	40.04	40.37	40.25	40.09	39.83	41.08	40.47	40.95	40.13
TiO_2	b.d.	b.d.	b.d.	b.d.	b.d.	b.d.	b.d.	b.d.	b.d.	b.d.
Al_2O_3	0.04	0.03	0.04	0.04	0.03	0.04	0.04	0.04	0.05	0.02
Cr_2O_3	0.01	0.01	0.02	0.02	0.02	0.03	0.01	0.01	0.01	0.03
V_2O_3	b.d.	b.d.	b.d.	b.d.	b.d.	b.d.	b.d.	b.d.	b.d.	b.d.
FeO	6.51	7.78	7.17	6.92	7.25	6.81	7.49	8.36	6.90	6.99
MnO	0.08	0.10	0.10	0.09	0.09	0.09	0.09	0.10	0.09	0.10
NiO	0.43	0.37	0.42	0.41	0.41	0.41	0.39	0.41	0.42	0.41
MgO	51.98	51.06	51.34	51.44	51.03	51.07	50.99	50.20	51.65	51.16
CaO	0.02	0.01	0.02	0.02	0.01	0.03	0.01	0.01	0.02	0.03
Na_2O	0.02	0.02	0.03	0.04	0.03	0.03	0.02	0.02	0.03	0.03
K_2O	b.d.	b.d.	b.d.	b.d.	b.d.	b.d.	b.d.	b.d.	b.d.	b.d.
Total	99.91	99.45	99.52	99.24	98.98	98.35	100.14	99.64	100.13	98.92
Mg#	93.44	92.13	92.73	92.98	92.61	93.04	92.39	91.45	93.03	92.88

Table 3.2: Major-element concentration (wt%) of the xenolith orthopyoxene.

Sample	Bo-01	Bo-02	Bo-03	Bo-04	Bo-05	Bo-07	Bo-08	Bo-10	Bo-12	Bo-13
Mineral	opx	opx	opx	opx	opx	opx	opx	opx	opx	opx
P_2O_5	b.d.	b.d.	b.d.	b.d.	b.d.	b.d.	b.d.	b.d.	b.d.	b.d.
SiO_2	57.06	57.34	57.40	56.67	57.29	57.62	57.30	53.65	57.65	57.32
TiO_2	0.05	b.d.	b.d.	b.d.	0.07	b.d.	0.16	b.d.	b.d.	b.d.
Al_2O_3	0.75	0.80	0.74	0.79	0.80	0.75	0.81	0.72	0.67	0.69
Cr_2O_3	0.23	0.38	0.27	0.39	0.25	0.34	0.23	0.34	0.31	0.28
V_2O_3	b.d.	b.d.	b.d.	b.d.	b.d.	b.d.	b.d.	b.d.	b.d.	b.d.
FeO	5.40	3.98	4.18	4.27	4.81	3.99	5.62	4.24	4.36	3.97
MnO	0.12	0.10	0.10	0.11	0.12	0.10	0.13	0.10	0.11	0.09
NiO	0.09	0.11	0.11	0.10	0.09	0.11	0.10	0.11	0.11	0.10
MgO	35.27	36.08	35.85	35.52	35.62	36.12	34.86	34.56	36.08	36.32
CaO	0.30	0.28	0.46	0.33	0.23	0.37	0.53	0.43	0.46	0.36
Na_2O	0.08	0.10	0.09	0.12	0.08	0.09	0.17	0.11	0.06	0.08
K_2O	b.d.	b.d.	b.d.	b.d.	b.d.	b.d.	b.d.	b.d.	b.d.	b.d.
Total	99.36	99.18	99.21	98.31	99.36	99.49	99.92	94.27	99.83	99.23
Mg#	92.09	94.17	93.87	93.69	92.96	94.17	91.70	93.57	93.65	94.22

Sample	Bo-14	Bo-17	Bo-18	Bo-19	Bo-20	Bo-21	Bo-26	Bo-27	Bo-30
Mineral	opx	opx	opx	opx	opx	opx	opx	opx	opx
P_2O_5	b.d.	b.d.	b.d.	b.d.	0.01	0.00	0.00	0.01	0.02
SiO_2	57.24	52.99	57.09	56.79	56.42	57.80	57.19	57.60	54.32
TiO_2	0.04	b.d.	b.d.	b.d.	0.01	0.00	0.04	0.00	0.03
Al_2O_3	0.75	0.55	0.79	0.79	0.81	0.77	0.78	0.82	0.77
Cr_2O_3	0.22	0.29	0.32	0.25	0.39	0.33	0.21	0.29	0.41
V_2O_3	b.d.	b.d.	b.d.	b.d.	0.00	0.00	0.00	0.00	0.01
FeO	4.91	5.08	4.23	4.56	4.14	4.57	5.20	4.20	4.51
MnO	0.12	0.10	0.10	0.11	0.10	0.11	0.12	0.10	0.11
NiO	0.08	0.19	0.11	0.09	0.11	0.10	0.09	0.11	0.13
MgO	35.52	39.73	35.65	35.62	35.21	35.49	35.16	35.71	36.60
CaO	0.23	0.29	0.42	0.24	0.44	0.36	0.25	0.44	0.61
Na_2O	0.09	0.08	0.15	0.08	0.18	0.11	0.07	0.12	0.13
K_2O	b.d.	b.d.	b.d.	b.d.	0.00	0.00	0.00	0.00	0.03
Total	99.22	99.32	98.89	98.54	97.81	99.65	99.11	99.39	97.66
Mg#	92.80	93.31	93.76	93.30	93.82	93.26	92.35	93.80	93.54

Table 3.4: Major-element concentration (wt%) of the xenolith clinopyroxene.

Sample	Bo-01	Bo-05	Bo-08	Bo-13	Bo-14	Bo-18	Bo-19	Bo-26	Bo-30
Mineral	cpx	cpx	cpx	cpx	cpx	cpx	cpx	cpx	cpx
P_2O_5	b.d.	b.d.	b.d.	b.d.	b.d.	b.d.	b.d.	b.d.	b.d.
SiO_2	53.81	54.20	54.68	53.33	54.15	54.28	53.54	54.13	53.11
TiO_2	0.18	0.20	0.41	0.64	0.12	0.03	0.04	0.10	0.35
Al_2O_3	2.22	3.02	2.93	2.39	3.00	2.86	3.02	2.48	1.75
Cr_2O_3	1.79	2.14	1.32	1.00	2.15	2.33	2.09	1.68	1.41
V_2O_3	0.05	0.05	0.05	0.03	0.05	0.04	0.05	0.04	0.04
FeO	2.53	2.38	3.04	2.80	2.45	2.19	2.20	2.39	2.58
MnO	0.07	0.06	0.10	0.11	0.07	0.07	0.06	0.07	0.11
NiO	0.04	0.04	0.04	0.03	0.04	0.05	0.04	0.04	0.03
MgO	15.82	14.94	16.28	18.50	14.78	15.86	14.77	15.43	18.25
CaO	20.39	19.28	17.88	18.70	19.07	18.22	19.21	20.22	19.54
Na_2O	1.84	2.61	2.43	1.23	2.60	2.41	2.45	1.96	1.20
K_2O	b.d.	b.d.	b.d.	b.d.	b.d.	b.d.	b.d.	b.d.	b.d.
Total	98.75	98.95	99.19	98.79	98.51	98.35	97.48	98.56	98.38
Mg#	91.77	91.79	90.52	92.18	91.49	92.82	92.29	91.99	92.66
Cr#	35.01	32.16	23.27	21.95	32.47	35.32	31.72	31.20	35.15

chondritic Lu (pentagons in Figure 3.4a). Garnets with humped and sloped patterns show La enrichment relative to Ce (i.e. a negative slope from La_N to Ce_N). One garnet has a normal REE_N pattern, similar to humped patterns but with almost flat $MREE_N$-$HREE_N$ from Gd onwards at ~10× chondritic abundance (triangles in Figure 3.4b). Another garnet has a steep slope in the $LREE_N$ similar to sinusoidal patterns followed by a slight negative slope through the $MREE_N$ and almost flat $HREE_N$. This pattern appears transitional between the sinusoidal and the normal patterns (open inverted triangles in Figure 3.4b).

3.4.3. Thermobarometry and oxybarometry

Several thermometer-barometer combinations were used to calculate equilibration P-T conditions of the samples. For rocks in which clinopyroxene was not observed, the olivine-garnet Fe-Mg exchange thermometer of O'Neill and Wood (1979; also O'Neill 1980) was used in combination with the Al in orthopyroxene barometer (Brey and Köhler 1990). A combination of the two-pyroxene thermometer (Brey and Köhler, 1990) and the Al in orthopyroxene barometer was additionally used for samples in which clinopyroxene was present. For a well-equilibrated rock, all thermobarometer combinations should give

Table 3.5: Laser ablation ICPMS in situ trace-element concentrations (in ppm) of the xenolith garnets; concentrations below the detection limits are marked "b.d."

Sample	Bo-01	Bo-02	Bo-03	Bo-04	Bo-05	Bo-07	Bo-08	Bo-10	Bo-12	Bo-13
Sc	102.83	106.93	92.25	113.51	120.99	103.45	159.10	115.08	114.61	100.99
Ti	56.66	18.24	19.18	35.92	59.58	71.81	2,433	233	30.43	41.22
Ni	16.89	27.32	47.49	37.98	18.59	31.26	37.82	36.76	48.37	29.28
Zn	7.49	7.10	7.94	9.63	7.69	b.d.	b.d.	b.d.	8.80	b.d.
Ga	b.d.	b.d.	b.d.	b.d.	b.d.	1.98	4.68	2.00	b.d.	1.72
Rb	5.21	0.09	0.13	1.20	0.27	0.60	b.d	0.20	0.54	0.09
Sr	5.55	1.12	0.74	1.87	0.47	4.95	0.24	0.52	1.98	2.73
Y	11.11	1.67	0.82	5.06	15.62	1.27	17.60	8.81	0.38	1.07
Zr	11.83	28.38	37.45	89.92	15.71	45.60	104.34	95.18	17.96	9.68
Nb	0.44	0.40	0.98	0.48	0.12	0.92	0.20	0.64	1.53	0.73
Ba	2.65	0.29	0.02	2.38	0.55	3.96	0.10	0.20	0.66	0.21
Cs	0.11	b.d.	b.d.	0.06	b.d.	0.06	b.d	0.07	0.02	b.d
La	0.38	0.08	0.04	0.08	0.14	0.33	0.03	0.03	0.16	0.56
Ce	0.94	1.05	0.60	0.74	0.26	1.11	0.13	0.27	1.89	9.04
Pr	0.17	0.78	0.59	0.43	0.10	0.46	0.07	0.16	1.44	2.67
Nd	1.02	7.43	5.17	3.85	0.83	5.92	0.91	2.72	10.38	13.76
Sm	0.56	2.12	1.86	3.13	0.90	2.36	1.04	2.10	1.19	0.88
Eu	0.23	0.47	0.43	0.96	0.44	0.58	0.50	0.75	0.14	0.17
Gd	1.04	1.15	0.94	2.32	1.60	1.36	2.19	2.09	0.24	0.43
Tb	0.22	0.10	0.08	0.21	0.30	0.11	0.44	0.34	0.03	0.04
Dy	1.75	0.49	0.29	1.14	2.32	0.38	3.38	2.01	0.13	0.21
Ho	0.44	0.09	0.05	0.17	0.57	0.05	0.70	0.37	0.04	0.05
Er	1.49	0.14	0.16	0.42	1.84	0.13	1.79	0.79	0.11	0.12
Tm	0.24	b.d.	0.04	0.12	0.31	0.03	0.23	0.13	0.02	0.03
Yb	1.63	0.20	0.37	0.29	2.43	0.17	1.47	0.86	0.20	0.19
Lu	0.28	0.05	0.07	0.11	0.45	0.06	0.22	0.10	0.05	0.07
Hf	0.21	0.48	0.66	1.43	0.18	0.72	1.66	1.55	0.40	0.11
Ta	0.04	0.04	0.07	0.10	0.05	0.04	0.10	0.06	0.07	b.d.

Sample	Bo-14	Bo-17	Bo-18	Bo-19	Bo-20	Bo-21	Bo-26	Bo-27	Bo-30
Sc	102.82	127.14	109.40	107.22	105.18	104.12	117.55	95.46	127.04
Ti	419	365	212	254	45.51	29.43	501	239	41.75
Ni	19.23	33.84	34.84	24.41	62.13	43.51	18.85	39.91	58.51
Zn	11.46	b.d.	b.d.	10.89	10.20	9.90	b.d.	b.d.	10.11
Ga	2.91	2.86	1.84	1.85	b.d.	b.d.	2.50	2.34	b.d.
Rb	b.d.	0.15	0.35	0.21	0.10	0.45	0.63	0.23	0.14
Sr	0.44	1.42	3.48	1.93	1.82	3.57	10.56	0.47	7.35
Y	14.00	2.88	5.27	9.93	9.63	5.26	13.29	3.06	5.70
Zr	20.53	60.10	72.78	40.19	152.42	87.54	20.25	87.14	123.93
Nb	0.15	0.73	0.59	0.26	0.46	0.98	0.68	0.52	1.10
Ba	0.18	0.68	0.86	0.75	0.78	2.08	2.21	0.28	1.90
Cs	0.02	0.08	0.07	0.06	0.02	b.d.	0.09	0.02	0.04
La	b.d.	0.19	0.16	0.39	0.38	0.54	1.14	0.04	0.60
Ce	0.29	1.52	0.57	0.83	0.46	1.64	2.51	0.33	1.15
Pr	0.15	0.60	0.22	0.26	0.20	0.54	0.34	0.17	0.34
Nd	1.91	5.96	3.61	2.46	1.78	3.56	2.21	2.30	2.77
Sm	1.96	2.62	2.02	1.85	2.73	2.28	1.08	1.76	3.20
Eu	0.70	0.81	0.63	0.81	1.11	0.79	0.45	0.67	1.02
Gd	2.79	1.95	1.63	3.11	4.24	2.63	1.28	1.80	3.68
Tb	0.48	0.21	0.23	0.50	0.51	0.28	0.28	0.22	0.35
Dy	2.92	0.68	1.33	2.57	2.28	1.30	2.11	0.87	1.44
Ho	0.50	0.09	0.18	0.43	0.35	0.22	0.42	0.10	0.25
Er	1.47	0.28	0.39	0.97	0.60	0.41	1.27	0.22	0.48
Tm	0.20	0.05	0.07	0.11	0.09	0.06	0.26	0.04	0.06
Yb	0.94	0.44	0.44	0.83	0.42	0.51	2.08	0.33	0.50
Lu	0.21	0.10	0.10	0.11	0.08	0.10	0.36	0.07	0.11
Hf	0.21	0.65	1.18	0.42	1.75	1.02	0.28	1.01	1.24
Ta	b.d.	0.06	b.d.	b.d.	b.d.	0.11	0.07	0.06	0.07

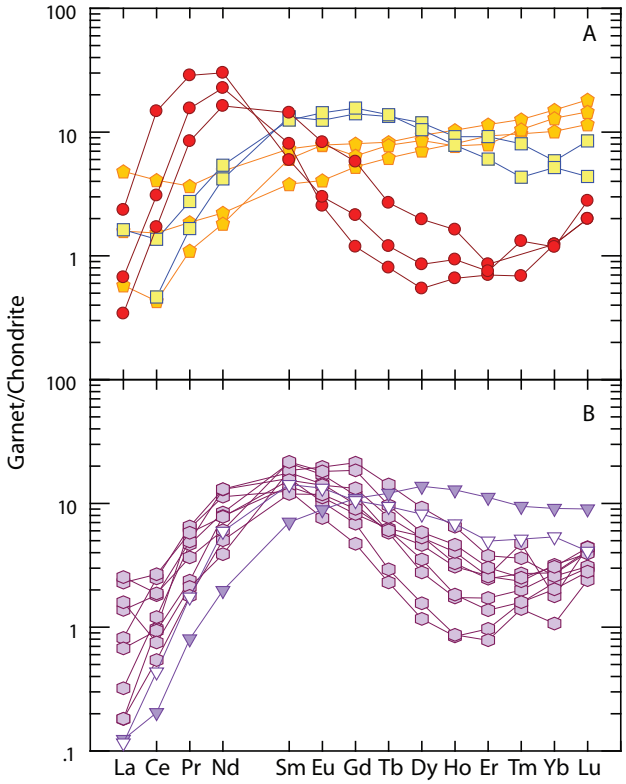

Figure 3.4: Chondrite normalized REE plots of xenolith garnets. **A.** Garnets with sinusoidal patterns and peaks at Nd are shown with circles. Two samples with humped REE_N patterns are shown with square symbols, the three samples with sloped patterns are shown with pentagons. **B.** The most commonly observed REE_N pattern in these samples is sinusoidal with maxima at Sm as shown with hexagonal symbols. The garnet with a normal type pattern is shown with filled inverted triangles. A garnet with a REE_N pattern transitional between normal and sinusoidal is shown with hollow inverted triangles. Normalization values are taken from McDonough and Sun (1995)

results agreeing within their respective experimental error. We consider disequilibrium evident in samples with differences in iteratively calculated temperatures of greater than 100ºC. Using this criterion, five of the 11 clinopyroxene-bearing samples are considered to have clinopyroxene that is not in equilibrium with orthopyroxene. The two-pyroxene temperatures, and consequently the Al-in-orthopyroxene pressures, calculated for these samples are greater than the temperatures calculated using Mg-Fe exchange thermometers. The differences in calculated temperatures and pressures range from 140 to 270ºC and 0.8 to 1.5 GPa, respectively. Regardless of which thermobarometer combination is used, the samples plot (Figure 3.5) along a 43mW/m^2 surface heat flow model geotherm (Pollack

and Chapman 1977).

These differences in P-T have a significant effect on the calculated oxygen fugacity expressed relative to the fayalite-magnetite-quartz buffer ($\Delta\log fO_2$ [FMQ]). A difference of 100ºC in the calculated temperature produces a variation in the $\Delta\log fO_2$ (FMQ) of 0.15 to 0.20; pressure has a larger effect, producing differences of 0.5 to 0.6 log-bar units for an assumed error of 0.5 GPa. The combined effect of differences in P-T estimates for samples with non-equilibrated clinopyroxene gives differences of 0.6 to 1.1 log-bar units in the calculated $\Delta\log fO_2$ (FMQ). All of our samples have demonstrated equilibrium between olivine, orthopyroxene and garnet – i.e. ΔT between orthopyroxene-garnet (Harley 1984)

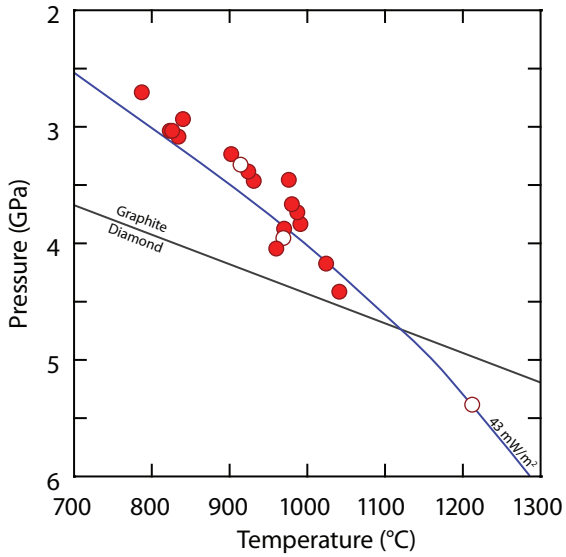

Figure 3.5: Equilibration pressure-temperature estimates calculated for our xenoliths using garnet-olivine Fe-Mg exchange thermometry and Al in orthopyroxene barometry. Also shown are the experimental diamond-graphite reaction boundary of Kennedy and Kennedy (1976) and the 43 mW/m^2 surface heat flow reference geotherm (Pollack and Chapman 1977). Coarse and granuloblastic (filled symbols) and porphyroclastic (open symbols) plot along the geotherm.

and olivine-garnet Fe-Mg exchange is less than ±80ºC. Therefore, we have used the olivine-garnet temperature and Al-in-orthopyroxene pressure in calculating oxygen fugacity (Table 3. 1).The fO_2 conditions calculated using the experimental calibration of Gudmundsson and Wood (1995) for these samples range over 4 orders of magnitude from $\Delta\log fO_2$ ~FMQ to FMQ-4.2 (Table 3.1). These values extend the range of $\Delta\log fO_2$ (FMQ) calculated for

garnet-bearing peridotite xenoliths from the Kaapvaal craton to both more oxidized and more reduced values.

3.5. Depth-fO_2 systematics

Woodland and Koch (2003) described an approximately linear trend of decreasing fO_2 with increasing depth in the garnet-bearing portion of the Kaapvaal lithospheric mantle sampled by kimberlites in South Africa and Lesotho (including data from Luth et al. 1990 and Canil and O'Neill 1996; as recalculated by McCammon et al. 2001). Coinciding with a transition from coarse-granular to porphyroclastic textures with increasing depth, Woodland and Koch (2003) observed a break in slope for their fO_2 data at ~150 km which they interpreted as reflecting the compositional and rheological boundary layer at the base of the lithosphere. Based on trace-element concentrations in garnet xenocrysts from Cretaceous Group 1 kimberlites, Griffin et al. (2003) place the base of the depleted lithospheric mantle for the Kaapvaal craton at ~180-190 km depth. The Kaapvaal seismic experiment (James et al., 2001) locates the present base of the lithosphere at even greater depth, at ~250 km. Thus, the break in slope for depth-fO_2 data observed by Woodland and Koch (2003) at Lesotho is shallower than these other depths to the lithosphere-asthenosphere boundary. The view that $\Delta\log fO_2$ (FMQ) calculated from porphyroclastic xenoliths reflects the redox state of the asthenosphere, therefore, is questionable.

As indicated above, temperature and, especially, pressure have significant effect on the calculated $\Delta\log fO_2$ (FMQ). The co-variation of depth (pressure) and fO_2 can be predicted for garnet-bearing lithospheric mantle by calculating $\Delta\log fO_2$ (FMQ) for a hypothetical isochemical peridotite assemblage. Assuming that $Fe^{3+}/\Sigma Fe$ in garnet remains constant and that there is no chemical exchange between minerals, $\Delta\log fO_2$ (FMQ) can be derived for T and P referenced to a model conductive geotherm corresponding e.g. to 43 mW/m^2 surface heat flow. The depth-$\Delta\log fO_2$ (FMQ) relationship for previously studied garnet-bearing peridotite xenoliths from South Africa and Lesotho, excluding the Kimberley region, can be described by two trends consistent with the predicted isochemical trends.

Xenoltihs with coarse and granuloblastic textures generally fall along a predicted depth-fO_2 trend calculated for a peridotite with garnet $Fe^{3+}/\Sigma Fe$ of 0.055, a value typical for coarse peridotites (Figure 3.6). Porphyroclastic peridotites are more oxidized and have a depth-fO_2 relationship consistent with a second predicted trend calculated for a peridotite with garnet $Fe^{3+}/\Sigma Fe$ of 0.10. The observation that porphyroclastic peridotites, with few exceptions, are more oxidized than coarse and granuloblastic xenoliths may appear contradictory with respect to their more Fe-rich bulk composition. According to equilibrium 3.1, the increased fayalite activity in olivine from porphyroclastic peridotites (e.g. Boyd 1987) results in a lower fO_2. This reduction in fO_2 predicted by the more fertile compositions of porphyroclastic peridotite xenoliths is more than compensated by their increased garnet ferric iron concentration (Luth et al. 1990). Thus, in the Kaapvaal craton, porphyroclastic peridotites are approximately 0.8 log-bar units (relative to FMQ) more oxidized at any given depth than coarse and granuloblastic varieties.

Both textural types of peridotite xenoliths preserve an overall decrease in fO_2 with depth. Assuming carbon saturation, the composition of a COH fluid in equilibrium with the deep garnet-bearing lithospheric mantle would be dominated by CH_4-H_2O components with the CH_4 /H_2O ratio increasing with increasing depth. The water maximum, the point at which the mole fraction of H_2O in the fluid is closest to unity, is crossed at approximately 120 km depth for compositions represented by porphyroclastic peridotites.

In contrast, similar texture-depth-fO_2 trends are not observed for our sample set from Kimberley and there is no discernable relationship between depth and fO_2 (Figure 3.7).

3.6. Metasomatism and the oxidation state of the subcratonic mantle

Compositional zoning of garnets in peridotite microxenoliths (<1 cm in diameter) from the Wesselton mine (one of the Kimberley kimberlites) preserve clear evidence of metasomatic re-enrichment – an increase in Ca from the core to rim accompanied by an increase in Ti, Zr and Y (Griffin et al. 1999). McCammon et al. (2001) measured the ferric iron concentration in the different garnet overgrowth zones and concluded that metasomatic

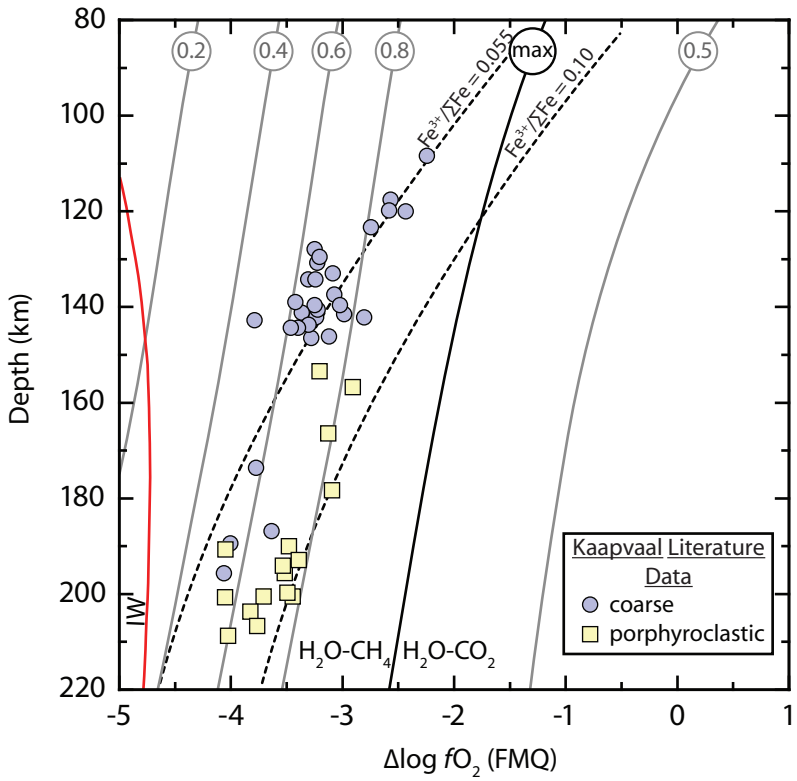

Figure 3.6: Depth- fO_2 relationship for previously-studied peridotite xenoliths from localities in the Kaapvaal craton excluding Kimberley (see text for references). Xenoliths with coarse and granuloblastic textures are shown with circles and porphyroclastic (sheared) peridotites are shown with squares. The dashed lines are parallel depth-fO_2 curves predicted for an isochemical change in P and T along a 43 mW/m^2 model geotherm. The location of the iron-wüstite buffer (IW) is shown for reference. Solid lines are isopleths indicating the mole fraction of H_2O in a COH fluid calculated after Huizenga (2001) assuming a carbon activity of 1. At fO_2 lower than the H_2O maximum, the fluid is predicted to be H_2O and CH_4-bearing. Under more oxidizing conditions, the fluid would contain H_2O and CO_2.

enrichment is a contributing factor in the oxidation of the lithospheric mantle. Compositional zoning is not present in our sample suite but the trace-element characteristics in the garnets attest to a varied metasomatic history of the lithospheric mantle.

Griffin and Ryan (1995) identified two trends in Zr-Y space for garnet that correspond to distinct types of metasomatism affecting peridotitic mantle. Both trends originate from a field for garnets derived from depleted sources (Figure 3.8) with low Y and Zr (Griffin and Ryan 1995). Garnets from melt metasomatized sources have a positive correlation in Y and Zr whereas garnets from phlogopite (fluid) metasomatized peridotites have increasing

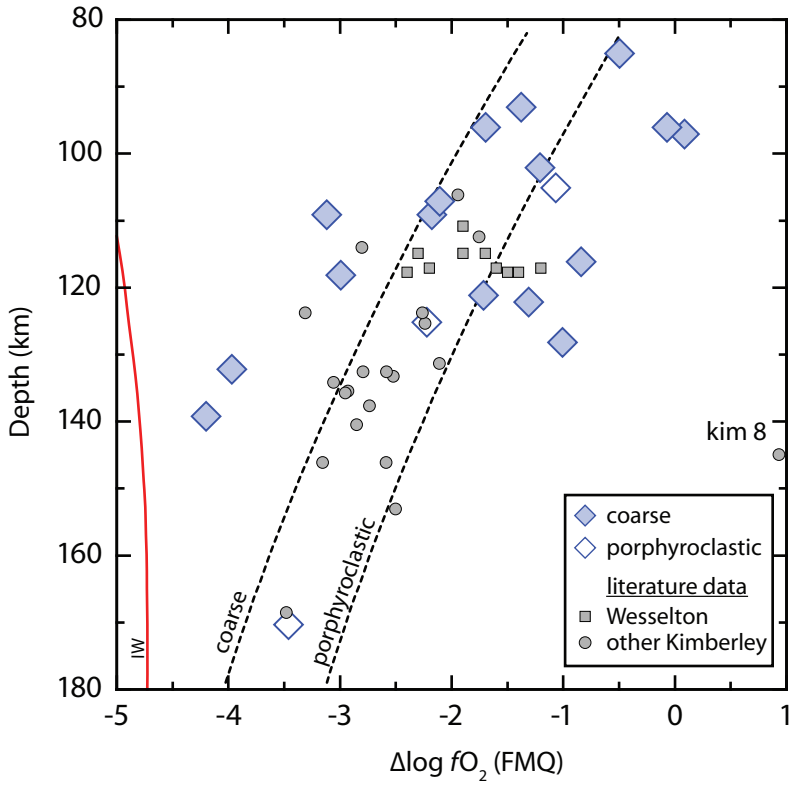

Figure 3.7: Depth-fO_2 plot for xenoliths samples from the Kimberley kimberlites only. Our samples with porphyroclastic textures are shown with open symbols; filled symbols represent samples with coarse and granuloblastic textures. The small grey circles are literature data for Kimberley xenoliths (references in the text). Small squares represent data from zoned garnets from the Wesselton mine (McCammon et al., 2001). The depth-fO_2 trends for other Kaapvaal xenoliths and the IW buffer are shown for reference.

Zr concentrations without a concomitant increase in Y. This diagram can be expanded by incorporating data from a recent study of metasomatized phlogopite-bearing garnet peridotite xenoliths from Kimberley. In this study, Gregoire et al. (2003) described two types of metasomatic trace-element patterns in clinopyroxene that relate to two major metasomatic events in the Kaapvaal lithosphere beneath the Kimberley region. The first is phlogopite-ilmenite-clinopyroxene (PIC) metasomatism, attributed to interaction with Group I kimberlitic melt; the second type has trace-element patterns similar to clinopyroxene in MARID (mica-amphibole-rutile-ilmenite-diopside; Dawson and Smith 1977) rocks. Trace-element concentrations of co-existing garnets in the metasomatized rocks define two distinct trends in Zr-Y space. Garnets from MARID metasomatized rocks

plot along a trend of increasing Y at nearly constant and low Zr (<50 ppm), extending from the depleted field. A trend of increasing Y with an associated increase in Zr is characteristic of garnets from PIC metasomatized rocks (Figure 3.8). This trend coincides with the high-temperature (melt metasomatism) field of Griffin and Ryan (Griffin and Ryan 1995).

Garnet REE_N profiles correspond to the styles of metasomatism indicated by their Zr-Y concentrations. Garnets with sinusoidal REE_N peaking at Nd plot within the depleted field of Griffin and Ryan (1995). Sinusoidal patterns with maxima at Sm are observed in garnets that plot along the trend ascribed to low-temperature, fluid metasomatism (Figure 3.8); garnets from PIC and MARID metasomatized rocks have normal and sloped or humped REE_N patterns, respectively (Figure 3.9). The similarities in Y and Zr concentrations, and REE_N patterns between our samples and those of Gregoire et al. (2003) suggest similar styles of metasomatic re-enrichment. The association of garnets with humped and sloped

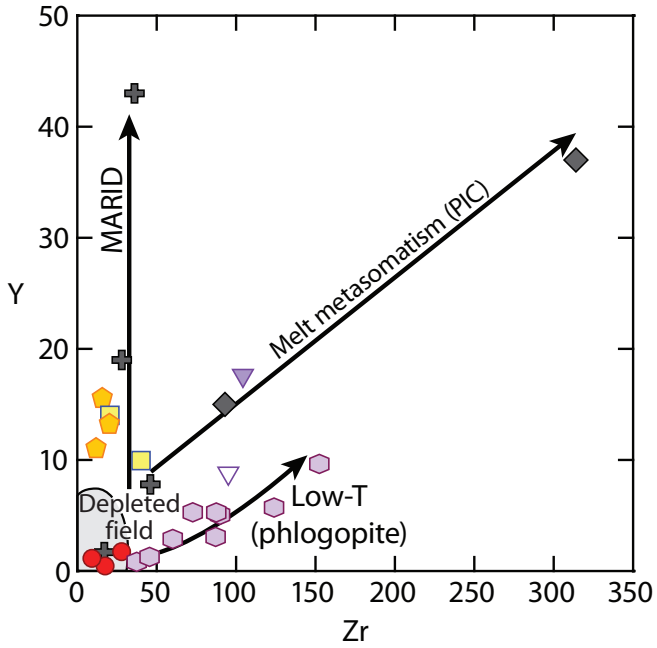

Figure 3.8: Y-Zr plot of the xenolith garnets modified after Griffin and Ryan (1995). Field of garnets from depleted source rocks is shaded. Symbols for these samples relate to the REE_N pattern (see Figure 3.4a, b). Other data are from Gregoire et al. (2003) showing a Y enrichment for MARID metasomatism (crosses) and, Y and Zr enrichment of PIC metasomatism (diamonds). Note that the sample with a REE_N pattern transitional between sinusoidal with Sm maxima and normal plots between the metasomatic trends associated with these REE_N profiles on this diagram.

REE_N patterns in our sample suite with MARID-like metasomatism is consistent with the observation of abundant clinopyroxene and coarse-grained phlogopite. Primary phlogopite is not present in samples that have not been affected by the MARID metasomatism.

Garnets recovered as inclusions in diamonds from the Kaapvaal craton have Y-Zr concentrations that overwhelmingly (93%) plot within the depleted field (Stachel et al., 2004 and references therein). Because the host diamond armours these garnets from post-encapsulation interaction with metasomatic fluids and melts, samples with garnets having depleted trace-element signatures may represent a "pre-metasomatic protolith" relative to the presumably much younger metasomatic events discussed here (e.g. Konzett et al. 1998). The most depleted harzburgitic garnet inclusions in diamonds have strongly sinusoidal REE_N patterns (Stachel et al. 2004) indicative of metasomatic re-enrichment in the most incompatible elements only. The evolution of REE_N patterns from strongly sinusoidal to

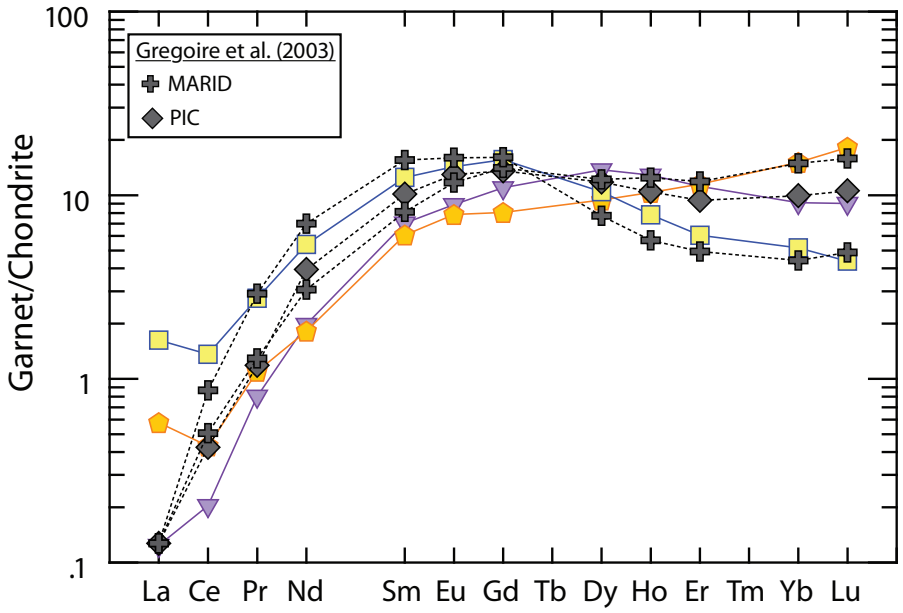

Figure 3.9: Comparison of REE_N in garnets from MARID and PIC metasomatized rocks (Gregoire et al., 2003) with three garnets from our sample suite. Sloped and humped REE_N are evident in MARID metasomatized samples; garnets with normal patterns derive from PIC metasomatized rocks. The similarity in REE_N between our sample suite and that of Gregoire et al. (2003) is predicted by similar Zr-Y concentrations, i.e. samples with overlapping REE_N profiles plot close together in Figure 3.8.

mildly sinusoidal and then to normal patterns typical of lherzolitic garnet inclusions has been interpreted as resulting from a transition from fluid dominated towards melt dominated metasomatism (Stachel et al. 2004). Thus, Nd_N/Y_N, (where Y_N proxies for $HREE_N$ such as Ho) characterizes the degree of sinuosity. This ratio can be used as a relative measure of the extent of metasomatic re-enrichment. Depleted garnets with strongly sinusoidal patterns have $Nd_N/Y_N >> 1$. With increasing metasomatism, Nd_N/Y_N ratios approach unity as the REE_N patterns evolve from mildly sinusoidal to normal. Garnets with sloped REE_N patterns have $Nd_N/Y_N < 1$. The $\Delta\log fO_2$ of our samples plotted vs. log Nd_N/Y_N (Figure 3.10a) shows increasing oxidation with increasing metasomatism for the MARID metasomatized samples. The co-variation is not as straightforward with samples that have apparently been metasomatized by fluids. Nevertheless, garnets from depleted source rocks are generally more reduced than garnets from metasomatized samples (Figure 3.10b).

As noted by McCammon et al. (2001) an increase in mantle oxidation resulting from metasomatism has implications for diamond stability. Carbon speciation in the mantle is dictated by the prevailing P-T-fO_2 conditions. The maximum stability limit of diamond in a peridotite matrix is determined by the intersection of the diamond-graphite transition and the magnesite-stabilizing reaction: $MgSiO_3 + MgCO_3 = Mg_2SiO_4 + C + O_2$ (EMOD/G) (Eggler and Baker 1982; as parameterized by Luth 1993, from updated, internally consistent thermochemical data).

The fO_2 conditions determined for peridotite xenoliths from the Kimberley kimberlites range in $\Delta\log fO_2$ (FMQ) from -4 to ~0. Seven of our samples cross over the EMOG reaction boundary and therefore carbonate would be the predicted stable host of carbon in these samples (Figure 3.11). The rim of one zoned garnet from the Wesselton mine also falls into the carbonate stability if the parameterized EMOD/G is used (*c.f.* McCammon et al. 2001). The most oxidized of our samples are those that have trace-element and mineralogical evidence for MARID-associated metasomatism.

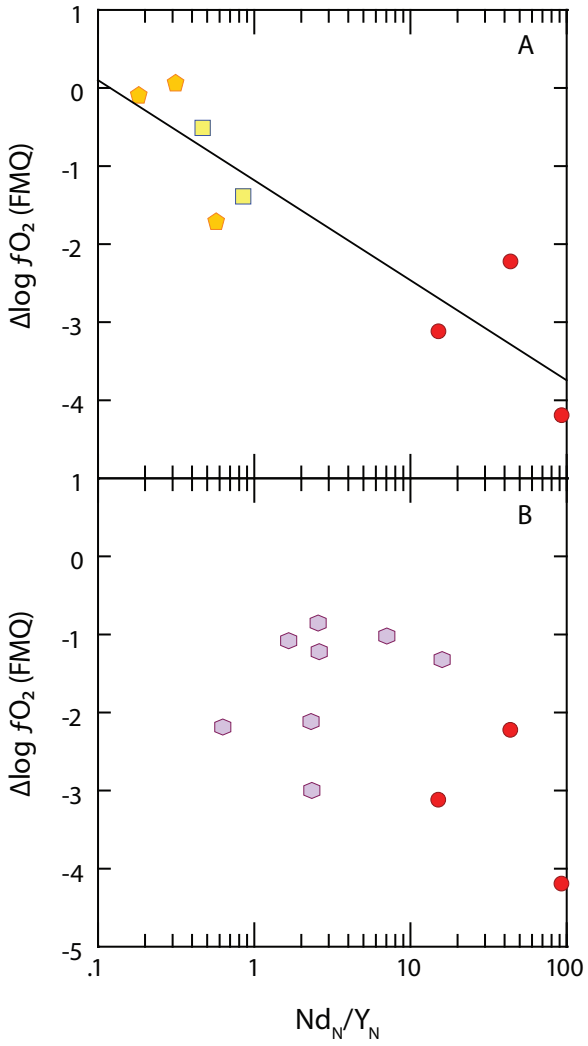

Figure 3.10: $\Delta \log fO_2$ (FMQ) plotted vs. Nd_N/Y as a measure of the degree of REE_N sinuosity. Symbols relate to the garnet REE_N profile as shown in Figure 3.4. **A.** A linear trend between log Nd_N/Y and $\Delta \log fO_2$ ($r^2 = 0.82$) demonstrates that oxidation increases with increasing degree of re-enrichment for MARID metasomatism. **B.** Fluid metasomatized samples also show a general oxidation with increasing degree of metasomatism but the trend is not as clear as for the MARID case.

We calculated the fO_2 conditions of MARID rocks using an oxybarometer derived for ilmenite-rutile equilibrium ($2Fe_2O_3$ (in ilmenite) + $4TiO_2 = 4FeTiO_3 + O_2$) applicable to these rocks (Zhao et al. 1999). Because the MARID mineral assemblage, by definition, excludes garnet and orthopyroxene, it is not possible to calculate an equilibrium pressure and temperature for these samples, and hence a unique fO_2 cannot be determined. We have, therefore, calculated a range of $\Delta \log fO_2$ (FMQ) using average MARID rutile and ilmenite

compositions and taking the maximum pressure and temperature of K-richterite stability (Sweeney et al. 1993; Konzett et al. 1997) and a 43 mW/m^2 surface heat flow geotherm (Pollack and Chapman 1977) as upper and lower temperature boundaries, respectively. The resulting area of possible MARID $\Delta\log fO_2$ (FMQ) is between 0.2 and 0.4 at 80 km tapering to -0.5 at 180 km depth (Figure 3.11). At approximately 180 km depth, the upper temperature stability limit of K-richterite intersects the 43 mW/m^2 surface heat flow model geotherm; thus the MARID assemblage is not stable at depths greater than 180 km. At shallower depths, the MARID field is more oxidized than the EMOD/G buffer reaction indicating that MARID metasomatism would stabilize magnesite at the expense of elemental carbon species – diamond or graphite.

Two of our five "MARID metasomatized" samples are clearly associated with this field and a third plots near the field (Figure 3.11). Woodland and Koch (2003) described a strongly metasomatized sample that has abundant clinopyroxene and chromian spinel and coarse phlogopite completely replacing garnet (their sample Kim 8). The fO_2 calculated using spinel-based equilibria for this sample puts it well into the stability field of carbonate ($\Delta\log fO_2$ (FMQ) = 0.94). These strongly metasomatized, oxidized samples indicate that portions of the lithospheric mantle in the Kimberley region that are no longer capable of hosting diamond or graphite.

Four of the fluid-metasomatized samples also plot within the carbonate stability field suggesting that fluid metasomatism can be relatively oxidizing and destructive to diamonds as well.

3.7. Conclusions

From this and previous studies of spinel- and garnet-bearing peridotite xenoliths, it is apparent that the mantle lithosphere is heterogeneous in oxygen fugacity vertically and laterally. The shallower spinel peridotite facies spans approximately four orders of magnitude in $\Delta\log fO_2$ (FMQ) from 1 to -3 (e.g. Ballhaus 1993), with some of the variability resulting from metasomatism, partial melt extraction, and tectonic setting. The

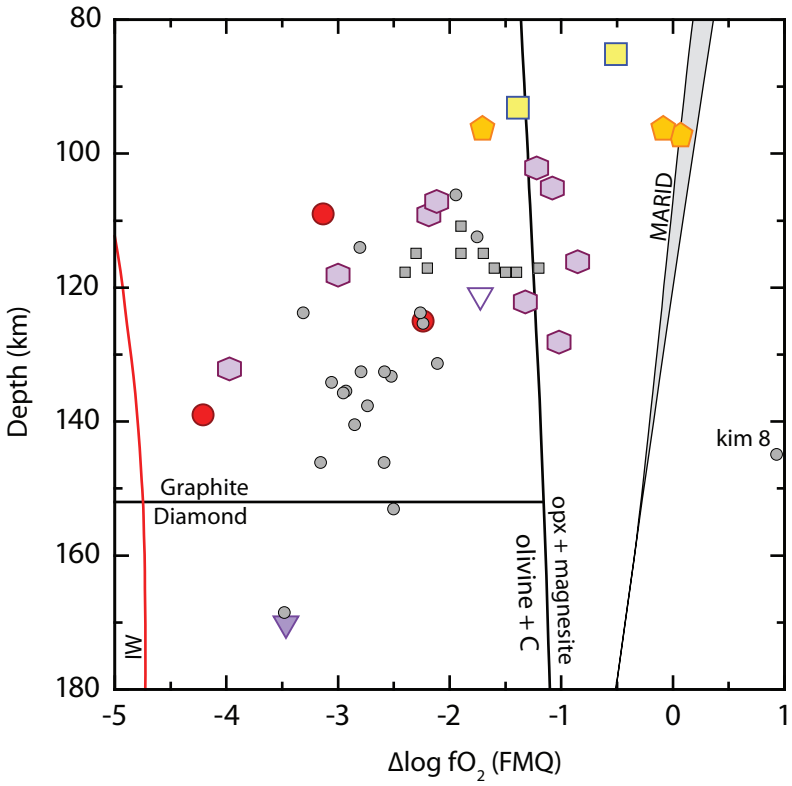

Figure 3.11: Depth-fO_2 relationship for Kimberley samples, symbols as in Figure 3.4a, b for our samples and Figure 3.7 for literature data. Areas of carbon speciation are identified by the intersection of the diamond/graphite transition curve intersecting the 43 mW/ m^2 reference geotherm at ~153 km depth and EMOD/G buffer. A field is also shown for MARID rocks (Zhao et al. 1999, details are in the text). Two of our samples with garnets exhibiting trace-element patterns indicative of MARID metasomatism are closely associated with the MARID field.

deeper, garnet facies lithospheric mantle shows a similar range of four orders of magnitude difference in $\Delta\log fO_2$ (FMQ) from 0 to -4. Consistent with the ΔV of reaction 3.1, there is an overall reduction with increased depth in the subcratonic lithospheric mantle relative to FMQ (e.g. Woodland and Koch 2003; McCammon and Kopylova 2004). Superimposed on this depth-fO_2 trend is oxidation resulting from metasomatic re-enrichment. Porphyroclastic peridotites, typically derived from deeper portions of the lithospheric mantle, are more fertile (e.g. lower average Fo content in olivine) and follow a more oxidized (by 0.8 log-bar units) depth-fO_2 trend than coarse and granuloblastic peridotite xenoliths. This may relate to a more oxidizing character of the melts infiltrating and metasomatizing porphyroclastic

peridotites. Alternatively, partitioning of ferric iron into garnet from clinopyroxene in response to generally higher temperatures for porphyroclastic peridotites (Canil and O'Neill 1996) may cause apparent oxidation in a closed system.

Xenoliths from the Kimberley region show such extensive metasomatic oxidation that a systematic depth-fO_2 trend can no longer be discerned for these samples. From the trace-element geochemistry of xenolith garnets coupled with *in situ* ferric iron measurements, we can conclude that the scatter observed in the depth-fO_2 systematics of the Kimberley xenoliths is a result of at least three different types of metasomatism. Of the three metasomatic styles revealed by garnet trace-element geochemistry, MARID melts appear to have been the most oxidizing and consequently the most diamond destructive.

References

Ballhaus C (1993) Redox states of lithospheric and asthenospheric upper mantle. Contrib Mineral Petrol 114:331-348

Boyd FR (1987) High- and low-temperature garnet peridotite xenoliths and their possible relation to the lithosphere-asthenosphere boundary beneath southern Africa. In: Nixon PH (ed) Mantle xenoliths. Wiley, Chichester, New York, pp 403-412

Brey GP, Köhler T (1990) Geothermobarmetry in four-phase lherzolites II. New thermometers, and practical assessment of existing thermobarometers. J Petrol 31:1353-1378

Bryndzia LT, Wood BJ (1990) Oxygen thermobarometry of abyssal spinel peridotites: the redox state and C-O-H volatile composition of the Earth's sub-oceanic upper mantle. Am J Sci 290:1093-1116

Canil D, O'Neill HSC (1996) Distribution of ferric iron in some upper-mantle assemblages. J Petrol 37:609-635

Dawson J, Smith J (1977) The MARID (mica-amphibole-rutile-ilmenite-diopside) suite of xenoliths in kimberlite. Geochim Cosmochim Acta 41:309-310

de Wit MJ, Roering C, Hart RJ, Armstrong RA, de Ronde CEJ, Green RWE, Tredoux M, Peberdy E, Hart RA (1992) Formation of an Archean continent. Nature 357:553-562

Eggler DH, Baker DR (1982) Reduced volatiles in the system C-O-H: Implications to mantle melting, fluid formation, and diamond genesis. In: Akimoto S, Manghnani MH (eds) High pressure research in geophysics. Center for Academic Publications Japan, Tokyo, pp 237-250

French B (1966) Some Geological Implications of Equilibrium between Graphite and a CHO Gas Phase at High Temperatures and Pressures. Rev Geophys 4:223-253

Gregoire M, Bell DR, Le Roex AP (2003) Garnet Lherzolites from the Kaapvaal Craton (South Africa): Trace Element Evidence for a Metasomatic History. J Petrol 44:629-657

Griffin W, Ryan C (1995) Trace elements in indicator minerals: area selection and target evaluation in diamond exploration. J Geochem Explor 53:311-337

Griffin WL, Shee SR, Ryan CG, Win TT, Wyatt BA (1999) Harzburgite to lherzolite and back again: metasomatic processes in ultramafic xenoliths from the Wesselton kimberlite, Kimberly, South Africa. Contrib Mineral Petrol 134:232-250

Griffin WL, O'Reilly SY, Natapov LM, Ryan CG (2003) The evolution of lithospheric mantle beneath the Kalahari Craton and its margins. Lithos 71:215-241

Grütter HS, Gurney JJ, Menzies AH, Winter F (2004) An updated classification scheme for mantle-derived garnet, for use by diamond explorers. Lithos 77:841-857

Gudmundsson G, Wood BJ (1995) Experimental test of garnet peridotite oxygen barometry. Contrib Mineral Petrol 119:56-67

Gurney JJ (1984) A correlation between garnets and diamonds in kimberlites. In: Glover JE, Harris PG (eds) Kimberlite occurrence and origins: a basis for conceptual models in exploration, Publication 8. Geology Department and University Extension, University of Western Australia, pp 143-166

Haggerty SE, Tompkins LA (1983) Redox state of Earth's upper mantle from kimberlitic ilmenites. 303:295-300

Haggerty SE (1990) Redox state of the continental lithosphere. In: Menzies MA (ed) Continental mantle. Clarendon Press; Oxford University Press, Oxford England, New York.

Harley SL (1984) An experimental study of the partitioning of Fe and Mg between garnet and orthopyroxene. Contrib Mineral Petrol 86:359-373

Harte B (1977) Rock nomenclature with particular relation to deformation and recrystallisation textures in olivine-bearing xenoliths. J Geol 85:279-288

Höfer HE, Brey GP, Schulz-Dobrick B, Oberhänsli R (1994) The determination of the oxidation state of iron by the electron microprobe. Eu J Min 6:407-418

Höfer HE (2002) Quantification of Fe^{2+}/Fe^{3+} by electron microprobe analysis – New developments. Hyper Inter 144/145:239-248

Höfer HE, Brey GP, Woodland AB (2003) Iron oxidation state of mantle minerals determined from L emission spectra by the electron microprobe. 8th International Kimberlite Conference Long Abstract. 4 pp.

Höfer HE, Brey GP (2007) The iron oxidation state of garnet by electron microprobe: Its determination with the flank method combined with major-element analysis. Am Min 92:873-885

Huizenga J-M (2001) Thermodynamic modelling of C-O-H fluids. Lithos 55:101-114

Kennedy CS, Kennedy GC (1976) The equilibrium boundary between graphite and diamond. J Geophys Res 81:2467-2470

Konzett J, Armstrong RA, Sweeney RJ, Compston W (1998) The timing of MARID metasomatism in the Kaapvaal mantle: An ion probe study of zircons from MARID xenoliths. Earth Planet Sci Lett 160:133-145

Konzett J, Sweeney RJ, Thompson AB, Ulmer P (1997) Potassium Amphibole Stability in the Upper Mantle: an Experimental Study in a Peralkaline KNCMASH System to 8.5 GPa. J Petrol 38:537-568

Luth RW, Virgo D, Boyd FR, Wood BJ (1990) Ferric iron in mantle-derived garnets: Implications for thermobarometry and for the oxidation state of the mantle. Contrib Mineral Petrol 104:56-72

Luth RW (1993) Diamonds, eclogites and the oxidation state of the Earth's mantle. Science 261:66-68

Matveev S, Ballhaus C, Fricke K, Truckenbrodt J, Ziegenben D (1997) Volatiles in the Earth's mantle: I. Synthesis of CHO fluids at 1273 K and 2.4 GPa. Geochim Cosmochim Acta 61:3081-3088

McCammon CA (1994) A Mössbauer milliprobe: Practical considerations. Hyper Inter 92:1235-1239

McCammon CA, Griffin WL, Shee SR, O'Neill HSC (2001) Oxidation during metasomatism in ultramafic xenoliths from the Wesselton kimberlite, South Africa: implications for the survival of diamond. Contrib Mineral Petrol 141:287-296

McCammon CA, Kopylova MG (2004) A redox profile of the Slave mantle and oxygen fugacity control in the cratonic mantle. Contrib Mineral Petrol 148:55-68

McDonough WF, Sun SS (1995) The Composition of the Earth. Chem Geol 120:223-253

McGuire A, Dyar M, Nielson J (1991) Metasomatic oxidation of upper mantle periodotite. Contrib Mineral Petrol 109:252-264

O'Neill HSC, Wood BJ (1979) An experimental study of Fe-Mg partitioning between garnet and olivine and its calibration as a geothermometer. Contrib Mineral Petrol 70:59-70

O'Neill HSC (1980) An experimental study of Fe-Mg partitioning between garnet and olivine and its calibration as a geothermometer: Corrections. Contrib Mineral Petrol 72:337

Pollack HN, Chapman DS (1977) On the regional variation of heat flow, geotherms, and lithospheric thickness. Tectonophysics 38:279-296

Ramsay RR, Tompkins LA (1994) The geology, heavy mineral concentrate mineralogy, and diamond prospectivity of the Boa Eperancaça and Cana Verde pipes, Corrego

D'anta, Minas Gerais, Brazil. In: Meyers HOA, Leonardos OH (eds) Proceedings of the 5th International Kimberlite Conference. Companhia de Pesquisa de Recursos Minerais, pp 329-345

Stachel T, Harris JW, Tappert R, Brey GP (2003) Peridotitic diamonds from the Slave and the Kaapvaal cratons - similarities and differences based on a preliminary data set. Lithos 71:489-503

Stachel T, Aulbach S, Brey GP, Harris JW, Leost I, Tappert R, Viljoen KS (2004) The trace element composition of silicate inclusions in diamonds: a review. Lithos 77:1-19

Sweeney RJ, Thompson AB, Ulmer P (1993) Phase relations of a natural MARID composition and implications for MARID genesis, lithospheric melting and mantle metasomatism. Contrib Mineral Petrol 115:225-241

Taylor WR, Green DH (1989) The role of reduced C-O-H fluids in mantle partial melting. In: Ross J (ed) Proceedings of the 4th International Kimberlite Conference. Blackwell, Carlton, Perth, Australia, pp 592-602

Wood BJ, Bryndzia LT, Johnson KE (1990) Mantle oxidation state and its relationship to tectonic environment and fluid speciation. Science 248:337-345

Woodland AB, O'Neill HSC (1993) Synthesis and stability of $Fe_3^{2+}Fe_2^{3+}Si_3O_{12}$ garnet and phase relations with $Fe_3Al_2Si_3O_{12}$-$Fe_3^{2+}Fe_2^{3+}Si_3O_{12}$ solutions. Am Min 78:1002-1015

Woodland AB, Peltonen P (1999) Ferric iron contents of garnet and clinopyroxene and estimated oxygen fugacities of peridotite xenoliths from the Eastern Finland Kimberlite Province. In: Gurney JJ, Gurney JL, Pascoe MD, Richardson SH (eds) Proceedings of the 7th International Kimberlite Conference. Red Roof Design, Cape Town, South Africa, pp 904-911

Woodland AB, Koch M (2003) Variation in oxygen fugacity with depth in the upper mantle beneath the Kaapvaal craton, southern Africa. Earth Planet Sci Lett 214:295-310

Woodland A, Kornprobst J, Tabit A (2006) Ferric iron in orogenic lherzolite massifs and controls of oxygen fugacity in the upper mantle. Lithos 89:222-241

Wyllie PJ, Huang W-L (1976) Carbonation and melting reactions in the system CaO-MgO-SiO_2-CO_2at mantle pressures with geophysical and petrological applications. Contrib Mineral Petrol 54:79-107

Zhao D, Essene EJ, Zhang Y (1999) An oxygen barometer for rutile-ilmenite assemblages: oxidation state of metasomatic agents in the mantle. Earth Planet Sci Lett 166:127-137

Chapter 4: Oxidation state of the lithospheric mantle beneath Diavik Diamond Mine, Central Slave Craton, NWT, Canada[1]

4.1. Introduction

Studies of the oxidation state of shallow spinel-facies peridotitic mantle have shown that the mantle is heterogeneous in oxidation state. The oxidation state of spinel peridotite is usually determined by the fO_2 recorded by the reaction:

$$\underset{\text{olivine}}{6Fe_2SiO_4} + O_2 = \underset{\text{opx}}{3Fe_2Si_3O_6} + \underset{\text{spinel}}{2Fe_3O_4} \quad (4.1)$$

Variations in the fO_2 of the shallow mantle have been attributed to depletion by melt extraction (Bryndzia and Wood 1990; Woodland et al. 2006) and differing tectonic setting (Wood et al. 1990). Reactions with infiltrating mantle fluids or melts (metasomatism) have also been suggested as causes for some of the heterogeneity of mantle fO_2 (McGuire et al. 1991; Ballhaus 1993).

Following the experimental calibration of a oxygen barometer suitable for garnet peridotites based on the reaction:

$$\underset{\text{garnet}}{2Fe_3^{2+}Fe_3^{3+}Si_3O_{12}} = \underset{\text{opx}}{Fe_2Si_2O_6} + \underset{\text{olivine}}{4Fe_2SiO_4} + O_2 \quad (4.2)$$

by Gudmundsson and Wood (1995), several analogous studies on garnet peridotite xenoliths have become available. Thus far, this oxybarometer has been applied to determine the fO_2 conditions for kimberlite-borne garnet peridotite xenoliths from Finland (Woodland and Peltonen 1999), South Africa and Lesotho (recalculated from data of Luth et al. 1990; Canil et al. 1994; Canil and O'Neill 1996; also McCammon et al. 2001; Woodland and Koch 2003; Creighton et al. 2009), and northern Canada (McCammon and Kopylova 2004). These studies have shown that the deeper portions of the cratonic lithospheric mantle are as heterogeneous in fO_2 as the shallow spinel-bearing peridotitic mantle.

1 A version of this chapter was submitted for publication to Contributions to Mineralogy and Petrology

Much of the heterogeneity in the deeper lithosphere has also been attributed to metasomatic processes. The first insight into the effect of metasomatism on oxidation state was gained through a study of zoned garnets from the Wesselton kimberlite in the Kimberley area of South Africa (McCammon et al. 2001), which showed that metasomatism caused oxidation of the affected mantle. A subsequent fO_2 study on metasomatized garnet peridotites from the Bultfontein kimberlite (also at Kimberley) agreed with this earlier conclusion and provided additional supporting evidence through the addition of garnet trace-element data (Creighton et al. 2009). With the present work, we aim to expand our knowledge of the effects of metasomatic re-enrichment processes on the oxidation state of the subcratonic mantle lithosphere and to compare the uniquely stratified lithospheric mantle of the central Slave Craton with that of the Kaapvaal Craton.

4.2. Samples

We examined 29 peridotite xenoliths for this study; 25 were recovered from the A154-North and South kimberlites during mining operations at Diavik (Figure 4.1; samples with MX prefix on Table 4.1) and four are from exploratory core drilled into the A154-North kimberlite prior to the commencement of mining (samples with A154 prefix on Table 1). Our sample suite includes 15 xenoliths with porphyroclastic and mosaic porphyroclastic texture and 15 with granuloblastic textures (terminology after Harte 1977). Alteration is present as variably serpentinized olivine and kelyphyte rims around garnet in all samples, but overall the preservation of the primary mineralogy in these xenoliths is excellent. Infiltration of kimberlitic melt is observed in eight of our samples and two other samples are cut by calcite veins. Zoning in mineral chemistry is observed neither petrographically nor in the mineral chemistry of any sample; nevertheless, all analyses reported here are from mineral cores to avoid any potential interaction with the transporting kimberlitic melt. One sample (MX5007) has spinel occurring as symplectite with clinopyroxene in addition to larger garnet crystals. Thermobarometric calculations (see below) place this sample at

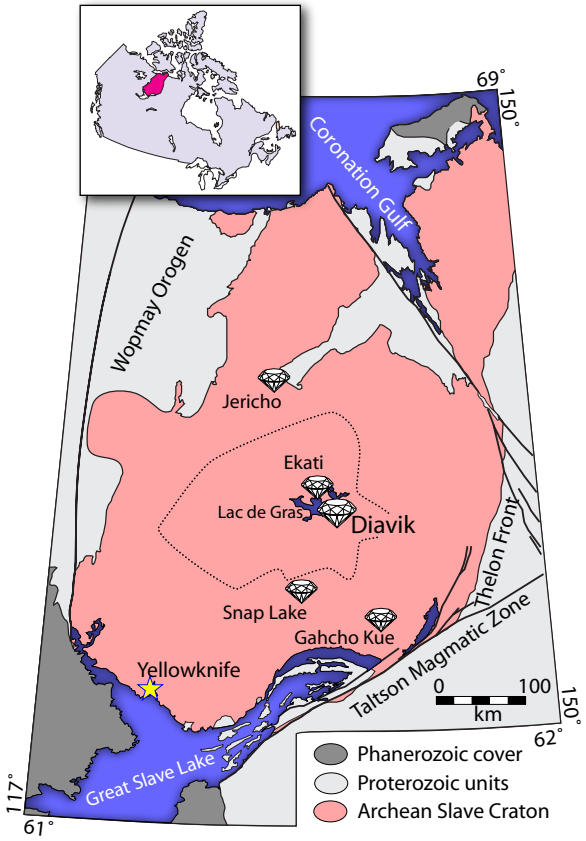

Figure 4.1: Location map of the Slave craton in northern Canada (modified after Bleeker and Davis 1999) showing the location of the Diavik diamond mine in the Lac de Gras area of the central portion of the craton. The central Slave mantle conductor occurs within the dotted line (Jones et al. 2003).

the lowest pressure (2.6 GPa) of any in our sample suite. Primary coarse-grained phlogopite or amphibole was not observed in any of the samples.

4.3. Analytical Methods

We measured the major and minor element concentrations (Tables 4.1, 4.2, 4.3, 4.4) of all minerals using a JEOL JXA-8900 Superprobe with beam conditions set to 20 kV gun potential and 20 nA current. Natural and synthetic mineral, oxide and metal standards were used to reduce counts to weight percent concentrations using the CITZAF algorithm. High precision analyses were achieved by setting count times from 30 to 60 seconds on each peak and half the peak count time on each background. The minimum detection limits from the average of at least 5 analyses are less than 100 ppm for all oxides except Na_2O

Table 4.1: Major-element composition of the garnets from xenoliths in this study measured using EPMA. The averages of at least 5 points are tabulated for all oxides except Fe_2O_3. Garnet classification (Grütter et al., 2004) and the Mg-number of coexisting olivine are also listed. Abbreviations for textures are: gb for granuloblastic, ppc for porphyroclastic and mpc for mosaic-porphyroclastic.

Sample	A154-01	A154-06	A154-09CR	A154-10	MX001	MX029	MX031	MX032	MX044	MX088	MX104	MX118	MX131	MX144
Texture	gb	ppc	gb	mpc	mpc	gb	gb	ppc	ppc	coarse	gb	coarse	mpc	gb
SiO_2	41.12	40.62	41.69	40.42	41.53	39.96	39.43	40.73	41.67	41.38	40.97	40.62	41.23	41.87
TiO_2	0.02	0.06	0.24	0.10	0.34	0.01	0.73	0.33	0.75	0.37	0.93	0.30	0.33	0.57
Al_2O_3	20.35	17.29	21.05	15.60	17.50	18.83	15.78	15.22	19.15	18.69	16.79	15.58	20.93	21.53
Cr_2O_3	4.94	7.98	3.89	10.18	7.29	6.87	8.83	9.65	4.16	5.69	7.08	9.47	3.23	1.77
Fe_2O_3	0.59	2.11	0.84	2.19	1.24	2.06	1.57	2.54	2.45	1.68	0.69	1.26	0.64	0.91
FeO	7.87	5.48	6.91	5.35	5.81	6.73	6.39	4.94	5.98	5.77	7.56	5.75	6.63	7.38
MnO	0.50	0.36	0.39	0.37	0.32	0.46	0.32	0.33	0.29	0.33	0.33	0.34	0.29	0.29
MgO	19.00	18.78	20.46	18.18	20.54	17.99	19.15	18.70	20.24	19.93	19.09	18.92	21.17	20.91
CaO	5.31	6.49	4.63	7.24	5.67	6.31	6.43	6.80	5.08	5.37	6.10	6.60	4.40	4.30
Na_2O	0.02	0.04	0.05	0.03	0.05	0.01	0.06	0.04	0.08	0.06	0.10	0.05	0.05	0.09
K_2O	0.06	0.00	0.00	0.00	0.00	0.00	0.00	0.01	0.00	0.00	0.00	0.00	0.00	0.00
Total	99.79	99.22	100.15	99.65	100.29	99.22	98.67	99.29	99.83	99.27	99.63	98.88	98.91	99.63
$Fe^{3+}/\Sigma Fe$	0.063	0.258	0.099	0.269	0.161	0.216	0.181	0.316	0.269	0.207	0.076	0.165	0.080	0.100
1σ	0.008	0.008	0.008	0.008	0.008	0.008	0.008	0.008	0.008	0.008	0.008	0.008	0.008	0.008
Garnet class	G9	G9	G9	G9	G11	G9	G11	G11	G11	G11	G11	G9	G9	G1
olv Mg-Number	92.3	91.3	91.3	91.3	91.6	91.8	90.9	91.4	89.7	91.4	90.3	91.6	91.3	89.9
Sample	MX162	MX165	MX5000	MX5001	MX5003	MX5004	MX5006	MX5007	MX5008	MX5009	MX5010	MX5011	MX5012	MX5020
Texture	mpc	mpc	gb	gb	gb	mpc	coarse	gb	mpc	mpc	gb	coarse	coarse	ppc
SiO_2	41.42	41.24	41.51	41.67	41.19	41.63	41.06	41.39	41.36	41.27	41.59	41.87	41.68	41.29
TiO_2	0.47	0.68	0.03	0.04	0.00	0.15	0.48	0.01	0.94	0.90	0.01	0.22	0.27	0.83
Al_2O_3	18.61	15.98	18.77	19.03	19.39	17.94	16.92	18.46	18.89	17.03	18.43	17.55	19.33	17.92
Cr_2O_3	6.01	8.42	5.51	5.47	6.06	6.87	7.79	7.21	4.38	6.99	7.29	7.88	5.54	6.01
Fe_2O_3	0.70	1.45	0.54	1.17	1.16	1.04	0.96	0.42	1.62	1.21	0.77	0.39	0.53	1.37
FeO	6.35	6.18	6.70	6.19	6.75	6.54	6.49	7.17	6.98	6.13	7.35	6.04	6.33	7.02
MnO	0.27	0.32	0.30	0.30	0.42	0.33	0.32	0.42	0.31	0.30	0.48	0.33	0.33	0.36
MgO	20.54	18.96	20.23	20.23	18.74	19.57	19.44	20.92	19.98	19.87	19.10	20.28	21.00	19.75
CaO	5.17	6.67	5.25	5.35	6.24	5.94	6.09	3.52	5.32	5.85	5.42	6.01	5.12	5.89
Na_2O	0.07	0.04	0.03	0.03	0.01	0.03	0.06	0.03	0.09	0.09	0.03	0.03	0.05	0.07
K_2O	0.00	0.00	0.00	0.00	0.00	0.00	0.00	0.00	0.01	0.00	0.00	0.00	0.00	0.00
Total	99.60	99.95	98.88	99.49	99.95	100.04	99.61	99.53	99.87	99.64	100.47	100.61	100.18	100.50
$Fe^{3+}/\Sigma Fe$	0.091	0.174	0.067	0.145	0.133	0.126	0.117	0.050	0.173	0.150	0.086	0.055	0.070	0.150
1σ	0.008	0.008	0.008	0.008	0.008	0.008	0.009	0.008	0.008	0.010	0.009	0.010	0.009	0.008
Garnet class	G11	G11	G9	G9	G9	G9	G11	G10	G11	G11	G9	G9	G9	G11
olv Mg-Number	91.7	91.3	91.3	91.3	92.7	91.0	91.2	92.6	89.8	91.3	92.7	92.4	91.9	90.0

Table 4.2: Major-element concentration (wt%) of the xenolith olivine.

Sample	P_2O_5	SiO_2	TiO_2	Al_2O_3	Cr_2O_3	FeO	MnO	NiO	MgO	CaO	Na_2O	Total
A154-01	b.d.	40.50	b.d.	0.01	b.d.	7.58	0.09	0.38	51.10	0.01	b.d.	99.71
A154-06	b.d.	40.06	b.d.	0.03	0.05	8.54	0.11	0.38	50.09	0.04	0.04	99.35
A154-09CR	0.01	40.46	0.01	0.02	0.02	8.55	0.12	0.37	50.52	0.02	0.02	100.13
A154-10	b.d.	40.28	0.00	0.03	0.06	8.53	0.12	0.38	50.45	0.04	0.03	99.93
MX001	b.d.	40.16	0.02	0.02	0.06	8.27	0.12	0.40	50.60	0.06	0.03	99.74
MX029	b.d.	40.21	b.d.	0.00	b.d.	8.07	0.09	0.00	50.70	b.d.	b.d.	99.09
MX031	b.d.	39.69	0.02	0.02	0.06	8.93	0.11	0.00	49.93	0.05	b.d.	98.81
MX032	0.01	40.62	b.d.	0.04	0.08	8.23	0.10	0.32	49.27	0.04	0.03	98.75
MX044	0.01	40.54	0.01	0.03	0.06	9.91	0.09	0.29	48.30	0.06	0.03	99.34
MX088	b.d.	40.65	0.01	0.03	0.05	8.30	0.09	0.26	49.40	0.04	0.02	98.86
MX104	0.02	40.81	0.02	0.05	0.06	9.35	0.10	0.31	48.74	0.04	0.02	99.51
MX118	b.d.	40.59	b.d.	0.03	0.08	8.12	0.09	0.32	49.54	0.07	0.02	98.89
MX131	0.01	40.26	b.d.	0.03	0.03	8.53	0.10	0.32	50.16	0.06	0.02	99.29
MX144	0.02	40.49	0.02	0.04	0.02	9.69	0.09	0.32	48.61	0.04	0.02	99.35
MX158	b.d.	40.57	0.03	0.03	0.03	8.95	0.09	0.34	49.13	0.03	0.02	99.22
MX162	b.d.	40.66	0.01	0.03	0.06	8.03	0.08	0.29	49.71	0.04	0.02	98.95
MX165	b.d.	40.76	0.02	0.04	0.07	8.39	0.09	0.33	49.61	0.04	0.02	99.37
MX5000	0.01	40.63	b.d.	0.03	0.05	8.38	0.09	0.32	49.20	0.04	0.02	98.77
MX5001	0.02	40.90	b.d.	0.03	0.04	8.41	0.09	0.33	49.44	0.04	0.03	99.32
MX5003	b.d.	40.68	b.d.	0.02	0.02	7.04	0.07	0.33	50.50	0.01	0.01	98.70
MX5004	b.d.	40.68	b.d.	0.04	0.05	8.75	0.09	0.33	49.42	0.05	0.02	99.44
MX5006	0.01	40.56	0.02	0.04	0.06	8.45	0.09	0.32	49.41	0.04	0.03	99.02
MX5007	b.d.	41.11	b.d.	0.03	0.03	7.18	0.07	0.28	50.58	0.02	0.02	99.33
MX5008	b.d.	40.42	0.03	0.05	0.04	9.85	0.10	0.26	48.46	0.05	0.03	99.30
MX5009	0.02	40.86	0.02	0.04	0.07	8.45	0.10	0.31	49.52	0.06	0.03	99.48
MX5010	b.d.	40.73	b.d.	0.03	0.02	7.11	0.07	0.31	50.90	b.d.	0.01	99.21
MX5011	0.01	40.73	b.d.	0.02	0.04	7.46	0.10	0.37	51.12	0.04	0.02	99.92
MX5012	b.d.	40.51	b.d.	0.02	0.03	7.94	0.11	0.36	50.77	0.05	0.02	99.83
MX5020	b.d.	40.37	0.02	0.02	0.04	9.66	0.12	0.34	49.00	0.06	0.02	99.66

Table 4.3: Major-element concentration (wt%) of the xenolith orthopyroxene.

Sample	P_2O_5	SiO_2	TiO_2	Al_2O_3	Cr_2O_3	FeO	MnO	NiO	MgO	CaO	Na_2O	Total
A154-01	b.d.	57.24	0.00	0.43	0.20	4.71	0.12	0.08	35.84	0.22	0.05	98.90
A154-06	b.d.	56.75	0.01	0.50	0.25	5.13	0.14	0.12	34.90	0.80	0.08	98.68
A154-09CR	b.d.	57.20	0.05	0.54	0.23	5.14	0.13	0.11	35.25	0.50	0.13	99.29
A154-10	b.d.	56.99	0.01	0.51	0.34	5.11	0.13	0.12	34.85	0.76	0.09	98.91
MX001	b.d.	57.58	0.07	0.61	0.34	4.96	0.13	0.13	34.88	0.98	0.18	99.88
MX029	b.d.	57.08	0.00	0.49	0.27	5.00	0.12	0.00	35.64	0.30	0.04	98.94
MX031	b.d.	56.39	0.10	0.56	0.41	5.32	0.12	0.00	34.69	0.79	0.17	98.56
MX032	b.d.	57.30	0.04	0.48	0.37	4.95	0.11	0.10	34.31	0.75	0.12	98.55
MX044	0.01	56.89	0.14	0.66	0.26	5.92	0.11	0.09	33.44	0.99	0.20	98.71
MX088	b.d.	57.35	0.09	0.50	0.23	4.98	0.11	0.08	34.56	0.59	0.13	98.62
MX104	0.02	57.34	0.18	0.54	0.30	5.66	0.12	0.10	33.99	0.80	0.17	99.21
MX118	0.01	57.11	0.03	0.47	0.37	4.82	0.11	0.09	34.46	0.76	0.12	98.35
MX131	b.d.	57.17	0.06	0.63	0.19	5.09	0.11	0.10	35.14	0.73	0.16	99.31
MX144	b.d.	57.12	0.13	0.64	0.14	5.83	0.11	0.10	33.70	0.76	0.19	98.73
MX158	b.d.	57.22	0.11	0.43	0.15	5.38	0.10	0.09	34.70	0.44	0.09	98.73
MX162	b.d.	57.24	0.10	0.56	0.30	4.77	0.09	0.09	34.39	0.70	0.17	98.42
MX165	b.d.	57.41	0.10	0.51	0.33	5.06	0.11	0.10	34.43	0.78	0.13	98.97
MX5000	b.d.	57.31	0.00	0.47	0.22	5.01	0.11	0.10	34.35	0.76	0.10	98.44
MX5001	b.d.	57.54	0.01	0.48	0.21	5.04	0.11	0.10	34.45	0.78	0.11	98.83
MX5003	b.d.	57.56	0.00	0.51	0.21	4.35	0.09	0.07	35.61	0.23	0.03	98.69
MX5004	0.01	57.26	0.03	0.51	0.29	5.23	0.11	0.10	34.43	0.74	0.12	98.84
MX5006	0.01	57.57	0.11	0.54	0.32	5.11	0.11	0.10	34.49	0.73	0.15	99.25
MX5007	b.d.	57.68	0.00	0.46	0.30	4.31	0.10	0.07	35.49	0.21	0.09	98.73
MX5008	0.01	57.07	0.17	0.58	0.21	5.90	0.12	0.09	33.80	0.85	0.17	98.97
MX5009	b.d.	57.26	0.15	0.60	0.34	5.03	0.12	0.09	34.12	0.89	0.19	98.80
MX5010	b.d.	57.71	0.02	0.41	0.20	4.43	0.10	0.07	35.77	0.18	0.04	98.92
MX5011	b.d.	57.86	0.03	0.55	0.32	4.46	0.12	0.11	35.57	0.72	0.12	99.84
MX5012	b.d.	57.56	0.04	0.62	0.28	4.74	0.12	0.11	35.26	0.72	0.16	99.60
MX5020	b.d.	57.09	0.14	0.59	0.28	5.78	0.13	0.11	34.00	0.84	0.17	99.14

Table 4.4: Major-element concentration (wt%) of the xenolith clinopyroxene.

Sample	P_2O_5	SiO_2	TiO_2	Al_2O_3	Cr_2O_3	FeO	MnO	NiO	MgO	CaO	Na_2O	K_2O	Total
A154-01	0.01	54.42	0.68	0.40	0.88	3.17	0.14	0.03	18.72	20.28	0.76	0.03	99.56
A154-06	0.01	53.97	0.01	0.68	0.72	2.64	0.11	0.07	18.89	20.61	0.54	0.07	98.32
A154-09CR	0.01	54.63	0.11	1.97	1.54	2.45	0.10	0.05	17.03	19.25	1.76	0.03	98.98
MX001	b.d.	54.80	0.14	1.33	1.29	2.96	0.12	0.06	18.99	18.16	1.32	0.06	99.28
MX029	b.d.	54.05	0.21	1.50	1.15	3.06	0.09	0.00	17.40	18.91	1.29	0.06	97.77
MX032	0.01	54.45	0.05	1.01	1.54	2.65	0.10	0.05	18.61	19.12	1.10	0.05	98.73
MX044	b.d.	54.66	0.17	1.67	0.96	3.70	0.11	0.05	19.07	17.11	1.41	0.04	98.95
MX088	0.01	54.55	0.13	1.59	1.19	2.59	0.09	0.03	17.82	19.17	1.42	0.04	98.64
MX104	0.01	54.46	0.22	1.43	1.24	3.29	0.11	0.05	18.36	18.16	1.41	0.05	98.80
MX131	0.01	54.71	0.10	1.93	0.99	2.70	0.09	0.05	18.12	18.12	1.48	0.07	98.36
MX144	b.d.	54.77	0.20	2.19	0.68	3.45	0.10	0.05	18.05	17.87	1.72	0.04	99.13
MX158	0.02	54.46	0.14	1.68	1.08	2.62	0.08	0.05	18.09	19.54	1.35	0.03	99.15
MX162	b.d.	54.45	0.14	1.73	1.61	2.66	0.08	0.04	18.06	18.37	1.66	0.04	98.84
MX165	b.d.	54.64	0.12	1.12	1.39	2.82	0.09	0.06	18.64	19.01	1.16	0.05	99.11
MX5000	0.01	54.63	0.01	1.02	0.81	2.67	0.09	0.05	18.92	19.31	0.85	0.06	98.43
MX5001	b.d.	54.78	0.01	1.03	0.81	2.69	0.10	0.05	19.02	19.66	0.87	0.07	99.08
MX5003	b.d.	54.34	0.05	1.20	1.18	1.70	0.07	0.04	17.42	21.86	1.11	b.d.	98.97
MX5004	b.d.	54.57	0.03	1.19	1.20	2.77	0.10	0.05	18.70	19.40	1.12	0.06	99.18
MX5006	0.01	54.63	0.14	1.34	1.47	2.78	0.10	0.04	18.42	18.92	1.37	0.05	99.28
MX5008	b.d.	54.33	0.24	1.59	1.10	3.57	0.10	0.04	18.54	18.01	1.40	0.05	98.99
MX5009	b.d.	54.57	0.19	1.63	1.42	3.05	0.11	0.05	18.79	17.66	1.46	0.04	98.98
MX5011	b.d.	54.82	0.04	1.27	1.39	2.24	0.10	0.05	18.55	18.64	1.14	0.08	98.35
MX5012	b.d.	54.72	0.08	1.76	1.41	2.54	0.10	0.05	18.03	18.59	1.56	0.05	98.93

(200 ppm).

Accurate and precise analysis of the concentration of ferric iron in garnet is essential for determining the oxygen fugacity of mantle-derived, garnet-bearing peridotite xenoliths. Therefore, we have used the electron microprobe-based flank method (Höfer and Brey 2007), with modifications specific for application to pyropic garnets (Creighton et al. 2009) for *in situ* ferric iron measurements of garnets in our samples. The accuracy of the modified flank method is comparable to the Mössbauer 'milliprobe' (Creighton et al. 2009). The 1σ error in $Fe^{3+}/\Sigma Fe$ reported for samples in this study is either the difference between repeat analyses of a single garnet grain (±0.008) or the propagated statistical error if it is larger than the former (Table 4.1). Measurements made with the modified flank method protocol have a spatial resolution of 30×30 μm.

Garnet trace-element concentrations were measured *in situ* with a Perkin Elmer Elan 6000 quadrupole ICP-MS coupled to a Merchantek UP 213 UV laser ablation system. The analytical spot size was 160 μm in diameter. The NIST 612 glass was used as an external standard and all analyses were normalized to the Ca concentration of the garnet determined by electron microprobe. The reported concentrations are the averages of at least three spots. Concentrations below the detection limits are indicated where appropriate (Table 4.5).

4.4. Results

4.4.1. Mineral major element composition

The major and minor element data measured on minerals in our samples are consistent with previous results on xenoliths/xenocrysts from the Diavik kimberlite pipes (Pearson et al. 1999; Aulbach et al. 2007). Garnets are predominantly lherzolitic in composition (Figure 4.2) with CaO concentrations ranging from 3.52 to 7.24 wt%, Cr_2O_3 concentrations from 1.77 to 10.2 wt% and total iron expressed as FeO from 6.40 to 8.60 wt%. Twelve garnets classify as high-Ti peridotitic or G11 (see Grütter et al. 2004) and one classifies as G1, with low Cr_2O_3 (1.77 wt%) and high TiO_2 (0.57 wt%) concentrations similar to megacryst

Table 4.5: Trace-element concentrations (ppm) measured using LA-ICPMS of garnets in our samples. Concentrations below the minimum limit of detection are indicated “b.d.”

Sample	A154-01	A154-06	A154-09CR	A154-10	MX001	MX029	MX031	MX032	MX044	MX088	MX104	MX118	MX131	MX144	MX158
Li	0.11	0.17	0.22	0.14	0.19	0.09	0.13	b.d.	0.39	0.70	0.58	0.20	0.15	0.54	b.d.
Sc	118.70	163.63	114.28	181.88	152.49	166.31	138.80	166.38	113.68	116.52	132.48	176.04	102.04	87.03	123.13
V	202.24	301.63	206.50	334.85	340.95	241.24	284.74	323.15	303.32	272.46	341.15	350.04	197.31	226.23	273.87
Ni	12.49	62.43	45.11	59.34	69.22	14.84	69.28	64.71	83.90	41.45	74.42	66.46	62.72	70.06	41.13
Zn	7.98	13.17	13.61	17.06	10.19	13.84	14.16	16.19	19.52	14.37	19.87	18.74	11.62	17.12	16.33
Ga	2.68	5.64	9.06	5.79	4.05	1.98	7.59	7.03	11.02	4.37	10.12	6.06	8.13	10.51	8.41
Rb	0.51	0.48	0.50	b.d.	0.39	b.d.	0.05	0.04	0.04	0.39	0.21	0.98	b.d.	0.54	0.69
Sr	0.76	0.69	1.47	1.12	0.71	0.78	0.81	0.65	0.68	0.42	1.47	0.69	0.21	0.31	1.03
Y	1.82	1.14	13.91	2.28	4.71	0.14	11.38	6.33	17.98	2.45	14.39	5.94	14.49	18.62	11.38
Zr	1.31	6.38	22.47	6.22	38.68	2.27	59.54	22.40	51.10	26.32	49.10	24.86	18.99	34.01	16.53
Nb	0.66	1.07	0.81	1.32	0.64	0.29	0.91	0.83	0.46	0.74	1.46	1.14	0.44	0.34	0.56
Cs	0.02	b.d.	b.d.	b.d.	0.05	b.d.	b.d.	b.d.	b.d.	0.04	b.d.	0.05	0.02	b.d.	0.04
Ba	1.94	24.10	3.96	0.53	0.75	0.28	b.d.	0.07	0.12	0.40	0.56	0.03	0.05	0.17	2.18
La	0.52	0.13	0.29	0.18	0.09	0.30	0.09	0.07	0.05	0.05	0.86	0.08	0.04	0.03	0.12
Ce	0.66	0.81	0.70	1.31	0.91	0.49	0.87	0.67	0.51	0.33	1.80	0.87	0.21	0.20	0.54
Pr	0.10	0.27	0.15	0.48	0.29	0.09	0.27	0.24	0.16	0.12	0.33	0.30	0.07	0.07	0.14
Nd	0.41	2.50	1.62	3.33	2.58	0.49	2.17	2.30	1.41	1.62	2.29	2.64	0.81	0.62	1.04
Sm	b.d.	1.08	1.04	1.38	1.63	b.d.	1.84	1.04	1.07	0.75	1.07	1.22	0.70	0.98	0.90
Eu	0.09	0.25	0.38	0.12	0.76	0.01	0.60	0.26	0.52	0.20	0.48	0.39	0.28	0.29	0.28
Gd	0.20	0.72	1.62	0.53	1.98	b.d.	2.09	0.93	2.05	0.57	2.70	1.53	1.07	1.44	1.46
Tb	b.d.	0.08	0.33	0.07	0.29	b.d.	0.40	0.16	0.43	0.09	0.43	0.20	0.29	0.36	0.26
Dy	0.44	0.29	2.55	0.44	1.51	b.d.	2.74	1.18	3.17	0.45	2.87	1.25	2.62	3.09	1.97
Ho	b.d.	0.07	0.57	0.10	0.24	b.d.	0.51	0.24	0.69	0.14	0.54	0.22	0.58	0.72	0.52
Er	0.33	b.d.	1.73	0.43	0.63	b.d.	1.26	0.87	1.97	0.33	1.75	0.82	1.92	2.24	1.37
Tm	b.d.	0.03	0.30	0.08	0.10	0.03	0.17	0.10	0.33	0.07	0.27	0.11	0.27	0.39	0.24
Yb	0.52	0.46	1.77	0.67	0.70	b.d.	1.10	0.95	2.47	0.45	1.45	0.81	2.52	2.78	1.72
Lu	0.15	0.10	0.36	0.16	0.12	0.09	0.19	0.15	0.35	0.09	0.28	0.15	0.33	0.42	0.22
Hf	0.21	0.23	0.58	0.31	1.15	0.11	1.76	0.50	1.59	0.80	1.31	0.67	0.70	0.84	0.53
Ta	0.06	0.16	0.08	0.20	0.13	0.10	0.10	0.08	0.07	0.07	0.10	0.14	0.04	0.04	0.05
W	0.13	0.11	0.07	0.20	0.08	0.09	0.06	0.10	0.04	0.06	0.03	0.18	0.14	b.d.	0.06
Pb	0.12	b.d.	0.07	0.12	0.12	0.18	0.09	0.09	0.05	0.07	b.d.	b.d.	0.12	0.19	1.53
Th	1.12	5.27	1.30	1.04	b.d.	130.54	3.22	1.05	0.95	0.67	1.71	7.12	2.17	0.57	0.72
U	0.03	0.07	b.d.	0.08	0.08	0.01	0.06	0.06	b.d.	0.07	0.33	0.09	0.03	0.05	0.09

Sample	MX162	MX165	MX5000	MX5001	MX5003	MX5004	MX5006	MX5007	MX5008	MX5009	MX5010	MX5011	MX5012	MX5020
Li	0.20	0.22	b.d.	0.25	0.14	0.35	b.d.	0.31	b.d.	0.22	0.06	b.d.	0.50	b.d.
Sc	115.08	152.42	140.64	139.97	133.16	181.19	151.62	160.88	113.54	135.11	176.27	133.24	119.68	128.72
V	258.34	335.43	320.62	317.09	256.10	369.61	301.52	236.02	310.47	271.00	251.31	321.32	280.73	328.58
Ni	58.74	72.86	64.48	62.43	15.15	61.73	63.72	33.74	55.62	76.11	14.66	48.86	49.54	63.22
Zn	15.45	16.35	12.84	11.36	9.52	15.10	15.85	13.33	15.53	15.43	9.91	9.82	11.05	13.01
Ga	6.81	8.42	5.10	5.19	1.68	6.99	5.95	3.67	9.22	8.16	1.67	4.10	6.34	9.61
Rb	0.23	0.42	3.41	5.65	1.87	0.16	b.d.	0.41	b.d.	b.d.	0.06	b.d.	3.19	0.45
Sr	0.38	0.64	0.27	0.29	0.78	0.78	0.57	1.87	2.12	0.69	6.84	0.69	0.61	1.43
Y	19.68	11.48	1.86	1.98	0.13	3.19	8.37	0.30	17.17	19.20	1.38	10.67	14.23	14.42
Zr	29.07	39.45	6.51	7.41	1.08	15.64	47.71	1.90	51.40	60.02	2.97	23.56	20.93	50.68
Nb	0.54	0.76	0.77	0.71	0.18	1.02	0.61	0.78	1.71	0.66	0.25	0.71	0.52	0.53
Cs	b.d.	b.d.	0.05	0.05	0.03	b.d.	b.d.	0.04	b.d.	b.d.	b.d.	b.d.	b.d.	b.d.
Ba	0.04	0.05	0.07	0.16	0.06	0.33	0.13	5.02	12.23	0.18	0.09	0.21	1.40	4.09
La	b.d.	0.09	0.07	0.06	0.24	0.10	0.06	0.38	1.11	0.09	1.05	0.09	0.13	0.18
Ce	0.35	0.72	0.47	0.44	1.37	0.52	0.64	1.67	1.92	0.62	4.67	0.86	0.54	0.63
Pr	0.14	0.22	0.16	0.15	0.26	0.19	0.24	0.29	0.27	0.24	0.57	0.25	0.18	0.20
Nd	1.02	2.27	1.12	1.26	1.50	1.59	2.48	1.42	2.25	1.95	1.98	2.32	1.38	1.66
Sm	0.98	1.67	0.83	b.d.	b.d.	0.94	1.84	b.d.	1.33	1.54	b.d.	1.37	b.d.	1.29
Eu	0.51	0.52	0.16	0.16	0.07	0.30	0.69	b.d.	0.79	0.65	0.07	0.36	0.48	0.55
Gd	2.17	1.95	0.63	0.45	0.20	0.98	2.05	0.42	2.46	2.80	0.45	1.63	2.42	1.88
Tb	0.44	0.37	0.06	0.08	0.03	0.11	0.33	0.01	0.47	0.57	0.07	0.37	0.40	0.47
Dy	3.66	2.45	0.34	0.32	0.07	0.63	1.76	0.17	2.31	4.04	0.34	2.24	2.79	3.30
Ho	0.83	0.46	0.12	0.09	0.01	0.12	0.36	b.d.	0.92	0.77	0.05	0.62	0.73	0.66
Er	2.42	1.28	0.29	0.31	0.09	0.36	0.88	0.07	2.66	2.19	0.26	2.22	2.29	2.08
Tm	0.29	0.19	0.06	0.09	0.01	0.11	0.13	0.03	0.33	0.30	0.04	0.31	0.37	0.32
Yb	2.01	0.98	0.66	0.63	0.23	0.86	0.92	0.25	2.61	1.72	0.38	2.08	2.87	1.83
Lu	0.30	0.18	0.13	0.10	0.06	0.14	0.15	0.13	0.40	0.25	0.12	0.26	0.39	0.38
Hf	0.87	1.10	0.19	0.17	b.d.	0.40	1.22	0.20	1.34	1.82	0.18	0.98	0.81	1.86
Ta	0.09	0.09	0.11	0.10	0.06	0.10	0.06	0.11	b.d.	0.09	0.01	b.d.	0.13	0.11
W	0.11	0.07	0.10	0.09	0.05	0.15	0.02	b.d.	b.d.	0.03	0.03	b.d.	b.d.	b.d.
Pb	0.12	0.12	0.08	0.09	0.09	0.15	0.13	0.82	b.d.	b.d.	0.12	0.31	0.73	0.40
Th	1.16	4.22	0.57	3.88	6.61	1.83	0.03	0.15	0.11	200.90	79.26	0.07	0.04	0.09
U	0.02	0.04	0.10	0.04	0.01	0.02	0.04	0.06	b.d.	0.04	0.03	0.08	0.06	0.09

garnets. Based on garnet composition, only one xenolith classifies as harzburgitic (Figure 4.2). Thus far, including literature data, only five garnets classify as G10 from Diavik xenoliths compared to 27 in the database of of samples from the nearby Ekati Diamond Mine (Menzies et al. 2004). Strongly sub-calcic harzburgitic garnets (CaO < 2 wt%) are absent in the Diavik xenolith suites studied to date.

Olivine and orthopyroxene are both magnesian with molar Mg-Numbers (100×[Mg/(Mg+Fe)]) ranging from 89.7 to 93.0 and 88.5 to 93.9, respectively, consistent with data from other cratons. Chrome diopside is observed in 23 of our 29 samples, with Al_2O_3 and Cr_2O_3 concentrations ranging from 0.40 to 2.24 and 0.68 to 2.30 wt%, respectively.

4.4.2. Garnet trace-element concentrations

Four types of chondrite-normalized rare earth element (REE_N) patterns are observed

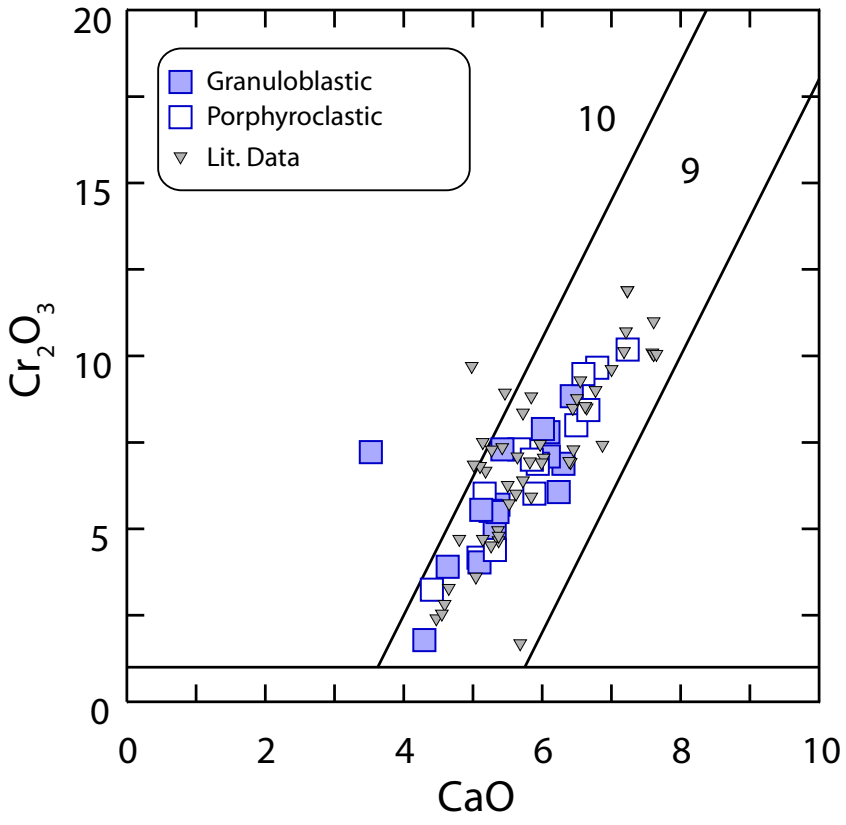

Figure 4.2: Plot of CaO vs. Cr_2O_3 of garnets from Diavik xenoliths. Compositional fields are from Grütter et al. (2004). The small inverted triangle symbols are from Aulbach et al. (2007) and Pearson et al. (1999).

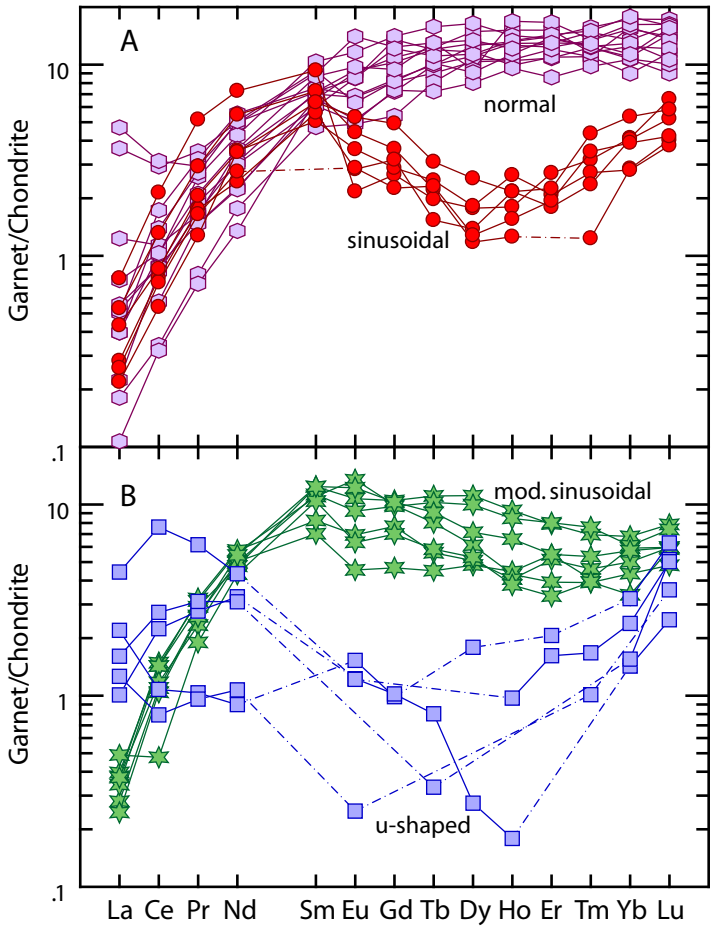

Figure 4.3: REE concentrations of xenolith garnets in our study. Concentrations are normalized to C1 chondrite values (McDonough and Sun 1995). Dashed lines indicate that that an element was below the limit of detection. Different symbols are used to distinguish groups of garnets with similar REE_N.

in garnets from our samples (Figure 4.3a, b). Six garnets have sinusoidal REE_N patterns – positive slopes to a maximum at Sm_N followed by negative slopes to a trough at Ho_N and 4-7× chondritic Lu (shows as filled circles in Figure 4.3a). Garnets from 13 samples have normal patterns – steep positive slopes from $LREE_N$ to $MREE_N$ and flat slopes at approximately 10-20× chondritic concentration through MREE and HREE (hexagons in Figure 4.3a). Three garnets with normal REE_N patterns have super-chondritic La concentrations and negative slopes from La_N to Ce_N. Six garnets are moderately sinusoidal – steep positive slopes through the $LREE_N$ to a maximum at Sm_N, then negative slopes to Tm_N or Yb_N, followed by a positive slope to 5-8× chondritic Lu (stars in Figure 4.3b). The remaining

five garnets have u-shaped patterns - LREE concentrations from 1-10× chrondritic followed by a negative slope to a trough through the $MREE_N$ and positive slopes to Lu at 2-8× chondritic concentration (squares in Figure 4.3b). Garnets with u-shaped REE_N patterns are only observed in xenoliths from <110 km depth whereas garnets with normal patterns occur in xenoliths from depths >140 km, consistent with the lithospheric mantle beneath the Slave craton containing an "ultradepleted" (predominantly harzburgitic) shallow layer and a more fertile (predominantly lherzolitic) deeper layer (Griffin et al. 1999). Low concentrations of Zr and Y in garnets with u-shaped REE_N (Table 4.5) are consistent with their derivation from the ultradepleted layer.

Garnets with u-shaped REE_N patterns are observed only in samples with granuloblastic textures whereas garnets with sinusoidal, moderately sinusoidal and normal REE_N patterns are found in rocks with porphyroclastic and granuloblastic textures.

4.4.3. Thermobarometry and oxygen fugacity calculations

Temperatures and pressures of last equilibration were calculated using a variety of thermobarometer combinations. Temperatures were calculated iteratively with pressure using the Al-in-orthopyroxene barometer of Brey and Köhler (1990; P_{BKN}), the olivine-garnet Fe-Mg exchange thermometer (O'Neill and Wood 1979; O'Neill 1980; $T_{O'Neill}$), the Fe-Mg orthopyroxene-garnet exchange thermometer of Harley (1984; T_{Harley}) and the two-pyroxene thermometer calibration of Brey and Köhler (1990). In order to assess whether the minerals were in mutual equilibrium, we calculated temperatures at fixed pressures using the above thermometer calibrations and also included the single crystal clinopyroxene thermometer of Nimis and Taylor (2000, T_{NT}). In a well-equilibrated rock, the temperatures calculated using these thermometers should agree within their respective experimental errors. Using differences >150°C between temperatures calculated at fixed pressure as the criterion for evidence of disequilibrium, all of our xenoliths show equilibrium between orthopyroxene and garnet, and olivine and garnet (i.e. $T_{O'Neill}$ is within 65°C of T_{Harley}; Table 4.6). Five of our clinopyroxene-bearing samples have T_{BKN}-$T_{O'Neill}$ between 150 and 185°C;

two of our samples have a much larger temperature differences of ~400°C. T_{NT} calculated for all clinopyroxene-bearing samples, however, agrees within 65°C with T_{BKN} (Figure 4.4b) suggesting that clinopyroxene is out of equilibrium with the rest of the mineral

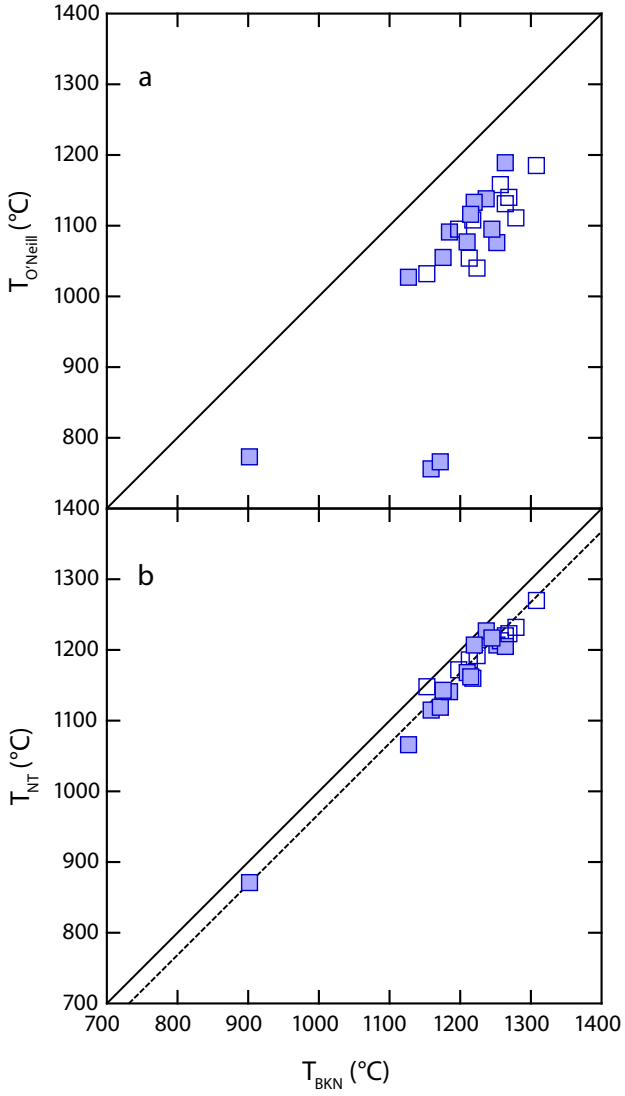

Figure 4.4: Comparison of the thermometer results for our samples. a. Fe-Mg garnet-olivine exchange thermometry ($T_{O'Neill}$) and b. the single clinopyroxene temperature (T_{NT}) compared with a two-pyroxene thermometer (T_{BKN}). All temperatures were calculated at constant pressure. The solid line in **a** and **b** are 1:1 correlation lines and the dashed line in **b** is a linear best fit correlation line (R^2=0.96). Note the three samples at low $T_{O'Neill}$ with high T_{BKN} are within 100°C of T_{NT} suggesting that clinopyroxene is not equilibrated in these samples. Solid symbols are for granuloblastic textures, open symbols are for samples with porphyroclastic textures.

assemblage.

If the disequilibrium determined for our samples was an artifact of unaccounted ferric iron in clinopyroxene and/or garnet (all iron in garnet is assumed to be ferrous for thermobarometric calculations), a correlation should exist between the temperature mismatch ($\Delta T = T_{BKN} - T_{O'Neill}$) and $\Delta \log fO_2$. No such trend is observed in our data, suggesting that exceedingly large differences in the Fe-Mg thermobarometry due to unaccounted Fe^{3+} is not the cause of the apparent disquilibrium of clinopyroxene. An explanation for unequilibrated clinopyroxene in these samples is beyond the scope of this paper but may relate to late re-introduction of clinopyroxene into these samples, as has been suggested for xenoliths in the Kimberley area (Simon et al. 2003). Based on the established equilibration of garnet and orthopyroxene in all the samples, the observation of unequilibrated clinopyroxene does not affect the fO_2 calculations presented here.

Despite $T_{O'Neill}$ being lower than T_{BKN} by approximately 100°C for all samples (Figure 4.4a; Table 4.6), we have chosen to use a combination of $T_{O'Neill}$ and P_{BKN} in calculating $\Delta \log fO_2$ in order to compare the fO_2 for samples with and without clinopyroxene (or with non-equilibrated clinopyroxene). The fO_2 calculated using the combination of T_{BKN} and P_{BKN} would shift $\Delta \log fO_2$ (FMQ) of the entire dataset by approximately -0.5 for all samples except the two with the largest temperature differences (Table 4.6). For these two samples, $\Delta \log fO_2$ (FMQ) based on T_{BKN} is lowered by approximately 3 log units because of the strong dependence of fO_2 on pressure for garnet peridotites.

The calculated temperatures and pressures range from 720 to 1210°C and 2.6 to 5.8 GPa (Table 4.1). Samples from our xenolith suite and peridotite xenoliths from previous studies (recalculated from data from Pearson et al. 1999; and Aulbach et al. 2007) predominantly plot between model geotherms with 40 and 42 mW/m^2 surface heat flow (Pollack and Chapman 1977), irrespective of texture (Figure 4.5). Evidence for a "stepped" geotherm proposed for the Lac de Gras region, whereby the P-T array below 900°C approximates a 35 mW/m^2 model conductive geotherm and higher temperature xenoliths

Table 4.6: Results of thermobarometric and oxygen fugacity calculations; $\Delta \log fO_2$ (FMQ) was calculated at $T_{O'Neill}$ calculated iteratively with P_{BKN}. T_{BKN} was calculated iteratively with P_{BKN}. Temperatures in the last three rows are calculated at fixed pressure and are useful for assessing whether the minerals are in mutual equilibrium.

Sample	A154-01	A154-06	A154-09CR	A154-10	MX001	MX029	MX031	MX032	MX044	MX088	MX104	MX118	MX131	MX144	MX158
$T_{O'Neill}$ (°C)	726	1048	1035	1032	1153	745	1045	1069	1207	1105	1086	1110	1178	1196	1056
P_{BKN} (GPa)	2.92	4.59	4.62	4.47	4.86	2.91	4.44	4.75	5.54	5.27	5.21	4.99	5.55	5.83	5.59
Log fO_2 (ΔFMQ)	-0.62	-1.18	-2.30	-1.01	-1.92	0.95	-1.28	-1.09	-2.04	-1.97	-3.28	-2.00	-3.48	-3.44	-3.50
1σ error	0.79	0.63	0.71	0.62	0.66	0.64	0.65	0.61	0.62	0.64	0.75	0.66	0.74	0.71	0.74
T_{BKN} (°C)	1227	1176	1146		1293	1246		1239	1346	1206	1293		1282	1281	1200
P_{BKN} (GPa)	6.79	5.39	5.40		5.73	6.80		5.71	6.60	6.00	6.84		6.28	6.45	6.80
Log fO_2 (ΔFMQ)	-3.71	-1.70	-2.84		-2.46	-2.13		-1.67	-2.70	-2.44	-4.31		-3.92	-3.81	-4.27
T_{Harley} (°C)	810	990	1010	976	1070	802	981	1007	1131	1056	1054	1026	1109	1171	1053
P_{BKN} (GPa)	3.50	4.24	4.45	4.18	4.36	3.31	4.04	4.41	4.99	4.92	4.97	4.54	5.08	5.65	5.57
$T_{O'Neill}$ (°C)*	756	1032	1027	1019	1131	766	1027	1054	1185	1091	1076	1090	1158	1189	1055
T_{BKN} (°C)*	1159	1153	1127		1264	1172		1213	1308	1185	1252		1257	1264	1176
T_{NT} (°C)*	1115	1148	1066		1220	1119		1186	1270	1141	1207		1213	1205	1143

Sample	MX162	MX165	MX5000	MX5001	MX5003	MX5004	MX5006	MX5007	MX5008	MX5009	MX5010	MX5011	MX5012	MX5020
$T_{O'Neill}$ (°C)	1128	1050	1156	1148	759	1115	1092	777	1154	1131	714	1114	1138	1135
P_{BKN} (GPa)	5.08	4.86	5.55	5.52	3.07	5.02	4.94	2.57	5.63	5.03	2.76	4.81	4.95	5.28
Log fO_2 (ΔFMQ)	-2.86	-1.76	-3.76	-2.63	0.21	-2.42	-2.39	-0.58	-2.53	-2.14	0.15	-3.42	-3.16	-2.40
1σ error	0.72	0.65	0.77	0.67	0.68	0.68	0.70	0.84	0.65	0.68	0.74	0.87	0.79	0.67
T_{BKN} (°C)	1244	1257	1261	1241	913	1223	1237		1304	1316		1271	1238	
P_{BKN} (GPa)	5.86	6.19	6.31	6.19	4.05	5.76	5.91		6.85	6.27		5.70	5.60	
Log fO_2 (ΔFMQ)	-3.35	-2.58	-4.23	-3.05	-0.71	-2.90	-3.01		-3.29	-2.91		-3.95	-3.58	
T_{Harley} (°C)	1059	1011	1093	1094	804	1042	1037	828	1108	1057	795	1031	1058	1074
P_{BKN} (GPa)	4.63	4.62	5.10	5.13	3.35	4.54	4.59	2.93	5.27	4.56	3.31	4.36	4.45	4.83
$T_{O'Neill}$ (°C)*	1108	1040	1138	1133	773	1095	1077	799	1140	1111	744	1095	1116	1116
T_{BKN} (°C)*	1218	1224	1237	1220	902	1198	1210		1269	1279		1245	1215	
T_{NT} (°C)*	1160	1192	1227	1207	871	1172	1168		1223	1232		1217	1162	

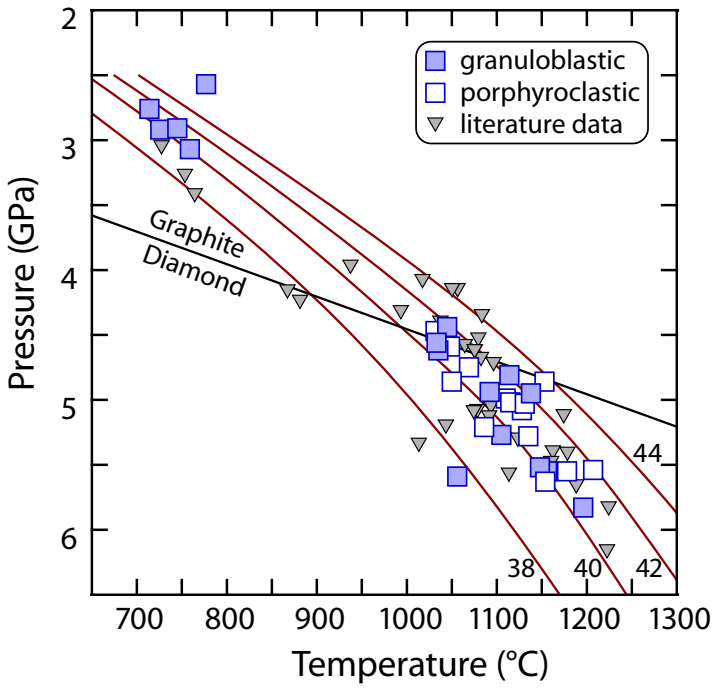

Figure 4.5: Olivine-garnet Fe-Mg exchange temperatures and orthopyroxene-garnet Al-exchange pressures calculated for xenoliths from the Diavik kimberlites. The small inverted symbols are recalculated from data published by Aulbach et al. (2007) and Pearson et al. (1999). Model geotherms from Pollack and Chapman (1977) and the experimentally derived diamond-graphite transition (Kennedy and Kennedy 1976) are also shown.

plot along a 40 mW/m^2 geotherm (Griffin et al. 1999; Pearson et al. 1999; Aulbach et al. 2007), is not present in our dataset.

Samples with the largest difference in calculated temperatures (i.e. the strongest evidence for disequilibrium) all have garnets with u-shaped patterns and granuloblastic textures. The low equilibration temperatures calculated for these samples indicates that they are derived from the shallow, ultradepleted layer (Griffin et al. 1999). The trace-element composition of garnets from these samples is consistent with this interpretation. There are no other correlations between the depth from which samples were derived and the trace-element composition of their garnets.

We calculated the oxygen fugacity of our samples, expressed for consistency with previous work relative to the fayalite-magnetite-quartz buffer (metastable at these depths) as $\Delta \log f\mathrm{O}_2$ (FMQ), using the experimental calibration of Gudmundsson and Wood (1995) that has an estimated 1σ error of ±0.6 log units. The total 1σ error for our $f\mathrm{O}_2$ calculations

are the sum of the calibration error and the 1σ error on the flank method measurements propagated through the oxybarometer calibration (Table 4.6). We did not include errors resulting from uncertainties in the thermobarometric calculations. For a typical sample from our dataset, a combined uncertainty of 100°C and 0.5 GPa in the calculated temperature and pressure would correspond to an uncertainty in $\Delta\log fO_2$ (FMQ) of +0.60/-0.80. The $\Delta\log fO_2$ (FMQ) of our Diavik samples ranges from 0.95 to -3.76 (Table 4.1) extending the fO_2 measured for kimberlite-hosted garnet peridotite xenoliths worldwide to more oxidized values. Garnets with the lowest and highest $Fe^{3+}/\Sigma Fe$ are from xenoliths with coarse and porphyroclastic textures, respectively, similar to studies from the Kaapvaal craton (Luth et al. 1990). But unlike xenoliths from Lesotho kimberlites (Woodland and Koch 2003), there is no clear systematic relationship between fO_2 and the texture of our samples. Similarly, there is no correlation between kimberlitic melt infiltration and fO_2; there is no evidence for oxidation or reduction caused by interaction with the kimberlite on ascent from the mantle.

4.5. Origin and evolution of Central Slave cratonic peridotites

As the major host of trace elements in peridotite (especially harzburgite), garnet is sensitive to, and can provide a history of, events that have affected their host rock. Garnet REE_N patterns are useful indicators of depletion and metasomatic re-enrichment events that affected their mantle source. Our samples have garnets with REE_N patterns that preserve a history of strong initial depletion followed by two differing styles of metasomatic re-enrichment.

Samples with garnets that have u-shaped, sinusoidal and moderately sinusoidal REE_N patterns, and high Cr-numbers (100*Cr/[Cr+Al]) preserve evidence of a two-stage depletion process. The high Cr-number of the garnet (indicative of high bulk rock Cr/Al) can only be explained by extensive partial melting in the spinel stability field (e.g. Canil and Wei 1992; Stachel et al. 1998) whereas positive slopes from the $MREE_N$ to $HREE_N$ indicates that partial melting was initiated in the garnet stability field (Stachel et al. 1998).

The residue of this polybaric melting event subsequently was brought back into the garnet stability field, preserving preserved evidence of the previous, low-pressure depletion. The LREE enrichment of these garnets indicates that they are not pristine samples of depleted mantle but that their host rocks were metasomatized by a highly fractionated (high LREE/HREE) agent (Stachel et al. 2004).

Garnets with normal REE_N patterns preserve evidence of a second style of metasomatic re-enrichment by comparatively less fractionated melts. Metasomatism by these melts re-introduces HREE and other HFSE in addition to highly incompatible trace-elements such as LREE. Because of increasing element compatibility in the garnet structure from LREE to HREE, melt metasomatism imparts normal REE_N patterns (Stachel et al. 2004) in garnets of affected peridotite effectively overprinting and erasing any trace-element evidence for depletion and any previous metasomatism. The high Cr-number of these garnets, however, still preserves evidence of previous depletion in the spinel stability field.

4.6. Pre-metasomatic oxygen fugacity

The barometric fO_2 calculated from the activities of ferric/ferrous-bearing phases (equations 4.1 and 4.2) can be reset by metasomatism (McGuire et al. 1991; Ballhaus 1993; McCammon et al. 2001; Creighton et al. 2009) and therefore is unsuitable for determining the pre-metasomatic fO_2 of peridotite xenoliths. In order to elucidate the effect of metasomatism on the fO_2 of the lithospheric mantle, a suitable starting point must be selected. We have chosen to use a depth-fO_2 curve calculated by Frost and McCammon (2008) for a garnet peridotite of bulk silicate earth composition. Their calculation assumes a constant bulk-rock $Fe^{3+}/\Sigma Fe$ and accounts for the temperature-dependent Fe-Mg partitioning between the constituent minerals. A pre-metasomatic fO_2 of FMQ-1.45 (NNO-1) at 3 GPa, determined by Canil (2004) from V/Al and V/Yb systematics of cratonic peridotites, falls on the curve predicted by Frost and McCammon (2008). Extrapolation of this predicted depth-fO_2 profile intersects the iron-wüstite fO_2 buffering reaction at approximately 7.5 GPa, consistent with experimental evidence suggesting that metal saturation occurs in the mantle between 7 and

8 GPa (Rohrbach et al. 2007). These two independent points support the notion that the depth-fO_2 trend calculated by Frost and McCammon (2008) is a reasonable estimate for the premetasomatic fO_2 of the lithospheric mantle. Therefore, we interpret the deviation of our samples from this predicted trend as the effect of metasomatism.

4.7. Oxidation and reduction by metasomatism

The two metasomatic styles observed in our samples (fluid and melt) had different effects on the fO_2 of the lithospheric mantle. Fluid-metasomatized samples (u-shaped, sinusoidal and moderately sinusoidal garnet REE_N patterns) have $\Delta \log fO_2$ (FMQ) decreasing from 1 at 80 to 90 km depth to -3.8 at ~180 km depth (Figure 4.6a). The trend defined by these samples crosses the enstatite-magnesite-olivine-diamond/graphite (EMOD/G) buffer (Eggler and Baker 1982) that defines the upper fO_2 stability limit of diamond/graphite in peridotite at approximately 135 km depth. This intersection indicates that graphite is not likely to be a stable phase in the shallow portion (i.e. the ultradepleted layer) of the lithospheric mantle beneath Diavik and that the fluid responsible for the metasomatism was strongly oxidizing and possibly carbonate-bearing. The oxidized nature of our samples derived from the ultra-depleted layer indicates the anomalously high conductivity observed from magnetotelluric data in the central Slave craton (Jones et al. 2003) cannot be attributed to the presence of graphite. The interaction of oxidized, LREE- and COH-rich metasomatic fluids will impart sinusoidal patterns on garnets with depleted signatures and precipitate diamond in the deeper portions of the lithospheric mantle.

As noted above, u-shaped REE_N patterns in garnets from the ultradepleted layer indicate that these samples were only mildly affected by the fluid metasomatism, but they are the most oxidized. This apparent contradiction can be partially resolved by considering the effects of pressure and temperature on fO_2. Increasing the temperature by 100°C and pressure by 0.5 GPa has a combined effect of reducing $\Delta \log fO_2$ (FMQ) by 0.65 to 0.80 (Creighton et al. 2009). Therefore, the elevated fO_2 of these samples is, in part, due to their low equilibration pressures and temperatures; their offset from the predicted depth-fO_2

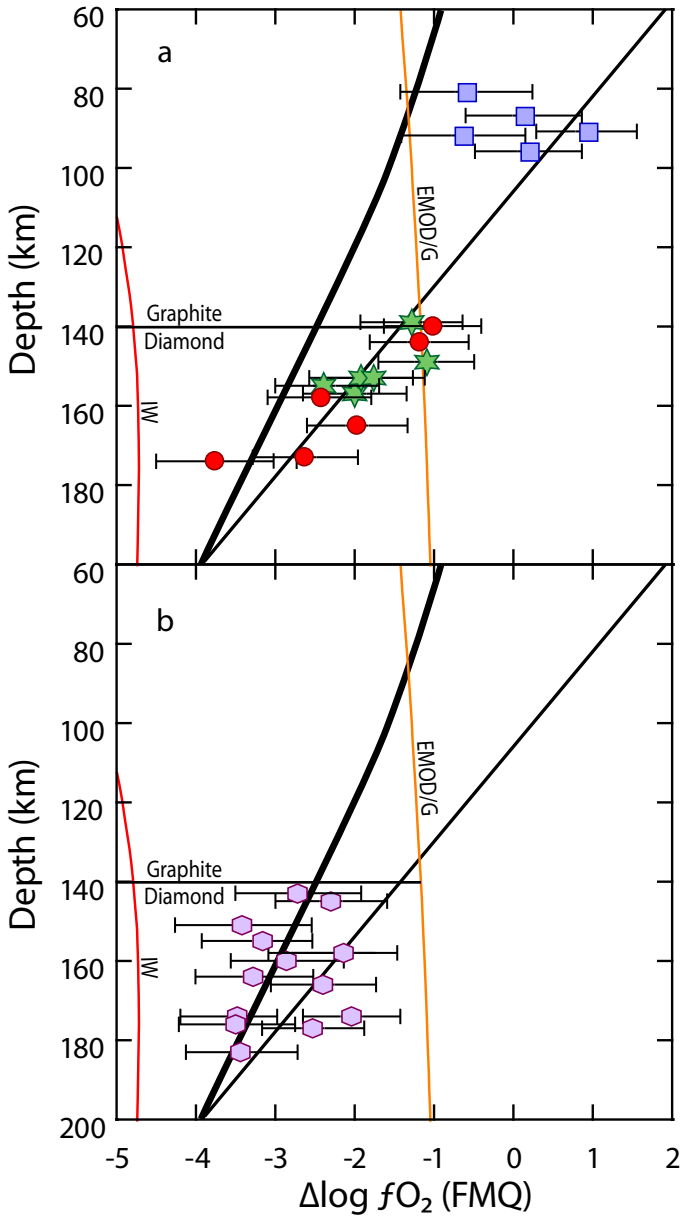

Figure 4.6: Variation in Δlog fO_2 (FMQ) with depth for xenoliths from our study. **a**. Samples with evidence for fluid metasomatism (u-shaped and sinusoidal REE_N patterns) and **b.** samples with evidence of melt metasomatism (i.e. normal REE_N patterns). Also shown are the iron-wüstite (IW) and enstatite-magnesite-olivine-diamond/graphite (EMOD/G) oxygen buffers, and the graphite-diamond transition. The thick curve represents the depth-fO_2 trend predicted for the pre-metasomatic garnet-bearing lithospheric mantle (from frost Frost and McCammon 2008). The thin line is a linear fit (R^2=0.80).through samples showing evidence for fluid metasomatism

trend (Figure 4.6a) is, however, an effect of metasomatic oxidation.

The effect of the melt metasomatism, responsible for imparting normal REE_N profiles in garnet, on the redox profile of the lithospheric mantle beneath Diavik is not as well constrained. Melt-metasomatized samples do not have an apparent depth-fO_2 trend but instead cover a range in $\Delta\log fO_2$ (FMQ) from -2 to -3.5 and fall between 140 and 185 km depth (Figure 4.6b). Most of the melt-metasomatized samples plot within error of the predicted bulk silicate earth depth-fO_2 trendline but three samples are more oxidized. This suggests that these samples were previously affected by an oxidizing metasomatic event; possibly by the same metasomatizing agent as the fluid-metasomatized samples. The melt metasomatism would, therefore, have been reducing, effectively returning the affected mantle back to fO_2 conditions predicted for pre-metasomatic garnet-bearing lithospheric mantle (Figure 4.6b).

Alternatively, the melt-metasomatized samples may not have previously been affected by oxidizing fluids. In this scenario, the melt must have been oxidizing (evidenced by the three samples falling on the oxidized side of the depth-fO_2 trend) and the samples plotting along the predicted depth-fO_2 profile would be the least affected by metasomatism. Consequently, samples falling on the predicted depth-fO_2 trend should preserve some trace-element evidence of the original depletion event (e.g. steep positive slopes from the $MREE_N$ to $HREE_N$) which is not the case for any of these samples. Therefore, an oxidizing character for the melt metasomatic event is considered very unlikely.

4.8. Comparison to other regions

4.8.1. Depth-fO_2 trends

A compilation of depth-fO_2 trends derived for garnet peridotite xenoliths from kimberlites from southern Africa (Woodland and Koch 2003; Creighton et al. 2009), for xenoliths in the northern (Jericho) and southern (Gahcho Kue) Slave craton (McCammon and Kopylova 2004) and for our melt-metasomtized samples is shown in Figure 4.7. The

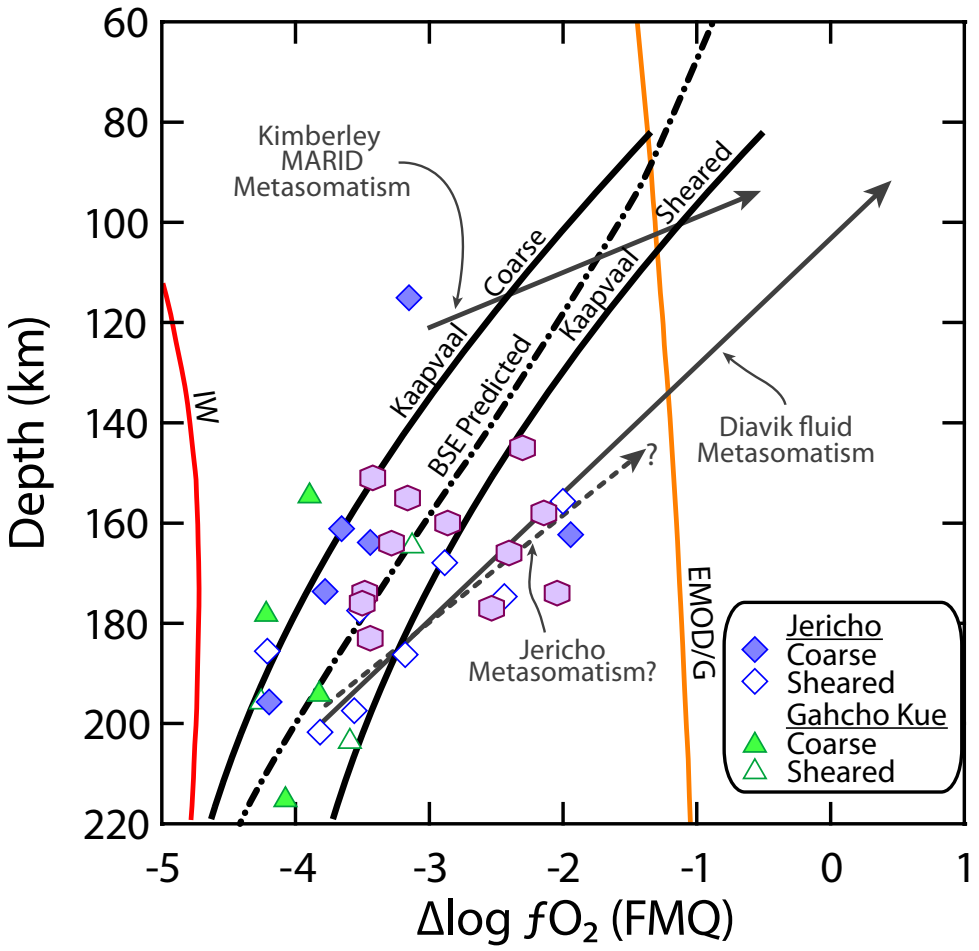

Figure 4.7: Compilation of Δlog fO_2 (FMQ) – depth data for xenoliths worldwide. A predicted depth-fO_2 trend calculated for bulk silicate earth (BSE; Frost and McCammon 2008) is shown as a reference from which metasomatic trends can be deduced. Data from the Kaapvaal craton are shown with depth-fO_2 trends defined by Creighton et al. (2009) for coarse and sheared peridotites. Data from the Jericho and Gahcho Kue kimberlites are shown as diamond and triangle shaped symbols, respectively. Open symbols indicate samples with sheared textures whereas filled symbols indicate samples with coarse textures. Samples from this study with evidence of melt metasomatism are shown with filled hexagons. Metasomatic oxidation trends from the Kimberley area of the Kaapvaal craton (MARID metasomatism) and a trend of increasing oxidation due to fluid metasomatism observed for our samples are also shown. A possible metasomatic trend for Jericho peridotite xenoliths is tentatively shown although it is not known if this metasomatism was caused by fluids or melts. The IW and EMOD/G buffers are shown for reference.

depth-fO_2 profile defined by xenoliths from the Kaapvaal craton is divided into two trends – one defined for coarse and granuloblastic xenoliths that have an average $Fe^{3+}/\Sigma Fe$ in garnet of 0.05 and a second for porphyroclastic (sheared) peridotites that have an average $Fe^{3+}/\Sigma Fe$ in garnet of approximately 0.15 (Creighton et al. 2009). The trend for coarse peridotites from the Kaapvaal craton is more reduced than a trend predicted for bulk silicate earth, assuming a whole rock $Fe^{3+}/\Sigma Fe$ of 0.02 (Frost and McCammon 2008), whereas the trend for sheared peridotites is more oxidized (Figure 4.7). Garnet peridotite xenoliths from Jericho have a similar texture-fO_2 relationship with porphyroclastic peridotites being generally more oxidized than coarse samples (McCammon and Kopylova 2004) and may indicate a depletion-reduction and metasomatism-oxidation relationship similar to the Kaapvaal craton. The few samples available from Gahcho Kue (McCammon and Kopylova 2004) are consistent with the notion that the same texture-fO_2 relationship exists in the southern Slave craton, but at present the data are too sparse to make a definitive statement. Xenoliths from Diavik, however, lack a clear relationship between fO_2 and rock texture.

4.8.2. Effects of metasomatism

The effects of metasomatic re-enrichment processes are superimposed on predicted depth-fO_2 trends from all xenolith suites studied thus far. The most prominent metasomatic overprint on the depth-fO_2 profile of the Kaapvaal lithospheric mantle is linked to the texture of the peridotite samples (Luth et al.1990). Many porphyroclastic peridotite xenoliths have more fertile bulk compositions and consequently have lower Mg-numbers in olivine and Ti-rich garnets compared to coarse peridotites (e.g. Boyd 1987). The reduced nature of coarse Kaapvaal xenoliths most likely is the result of high degrees of depletion required for their initial formation, whereas the sheared peridotites were oxidized as a result of the metasomatism that re-introduced Fe and Ti. At Kimberley, an additional metasomatic overprint mainly affecting the shallow lithospheric mantle that may be linked to the MARID (Dawson and Smith 1977) event in this region was strongly oxidizing (Creighton et al. 2009). Diavik xenoliths affected by fluid metasomatism preserve evidence for oxidation

occurring over a depth interval of approximately 100 km (Figure 4.6a). Data from Jericho appear to follow a similar metasomatic trend (Figure 4.7), but in the absence of trace-element data for garnets in the Jericho samples it is not possible to determine whether this apparent metasomatic trend is a result of fluid or melt metasomatism.

4.9. Conclusions

Garnet peridotite xenoliths from the Diavik diamond mine in the central Slave craton preserve a complex history of primary depletion and subsequent metasomatic re-enrichment, both of which have had significant effects on the oxidation state of the lithospheric mantle. The mantle in the central Slave craton is layered with respect to chemical depletion (Griffin et al. 1999) and redox state. Garnets in xenoliths derived from the highly melt depleted shallow (<140 km) layer (Griffin et al. 1999) are ultradepleted in their trace-element patterns and have the highest fO_2 of any garnet peridotite determined thus far. Two distinct styles of metasomatic re-enrichment are recognized. Fluid dominated metasomatism imparted u-shaped and sinusoidal REE_N patterns in affected garnets and had a strong oxidizing effect on the lithospheric mantle. Reduction of the COH component of the fluids involved in this style of metasomatism would have precipitated diamond upon interaction with the depleted and, consequently, reduced lithospheric mantle. The ubiquity of garnets with sinusoidal REE_N patterns recovered as inclusions in diamonds from worldwide sources (Stachel et al. 2004) could indicate that this type of metasomatism may be a principal mechanism of diamond formation in highly depleted (harzburgitic-dunitic) sources. The second metasomatic event, affecting only the lower layer in the lithospheric mantle beneath Diavik, was caused by the infiltration of HREE and other HFSE carrying melts. The redox effect of this metasomatism was relatively weak but apparently reducing. It is unlikely that the infiltration of a reducing melt into approximately equally reduced lithosphere would lead to further diamond precipitation. The reducing nature of the melt metasomatism at Diavik was unlike the MARID metasomatism in the Kaapvaal craton (Creighton et al.

2009) in that the Diavik melt metasomatic event was not diamond destructive.

References

Aulbach S, Griffin WL, Pearson NJ, O'Reilly SY, Doyle BJ (2007) Lithosphere formation in the central Slave Craton (Canada): plume subcretion or lithosphere accretion. Contrib Mineral Petrol 154:409-427

Ballhaus C (1993) Redox states of lithospheric and asthenospheric upper mantle. Contrib Mineral Petrol 114:331-348

Bleeker W, Davis WJ (1999) The 1991-1996 NATMAP Slave province project: Introduction. Canadian Journal of Earth Science 36:1033-1042

Boyd FR (1987) High- and low-temperature garnet peridotite xenoliths and their possible relation to the lithosphere-asthenosphere boundary beneath southern Africa. In: Nixon PH (ed) Mantle xenoliths. Wiley, Chichester, New York, pp 403-412

Brey GP, Köhler T (1990) Geothermobarmetry in four-phase lherzolites II. New thermometers, and practical assessment of existing thermobarometers. J Petrol 31:1353-1378

Bryndzia LT, Wood BJ (1990) Oxygen thermobarometry of abyssal spinel peridotites: the redox state and C-O-H volatile composition of the Earth's sub-oceanic upper mantle. American Journal of Science 290:1093-1116

Canil D, Wei K (1992) Constraints on the origin of mantle-derived low Ca garnets. Contrib Mineral Petrol 109:421-430

Canil D, O'Neill HSC, Pearson DG, Rudnick RL, McDonough WF, Carswell DA (1994) Ferric iron in peridotites and mantle oxidation states. Earth Planet Sci Lett 123:205-220

Canil D, O'Neill HSC (1996) Distribution of ferric iron in some upper-mantle assemblages. J Petrol 37:609-635

Canil D (2004) Mildly incompatible elements in peridotites and the origins of mantle lithosphere. Lithos 77:375-393

Creighton S, Stachel T, Matveev S, Höfer HE, McCammon C, Luth RW (2009) Oxidation of the Kaapvaal lithospheric mantle driven by metasomatism. Contrib Mineral Petrol 157:491-504

Dawson J, Smith J (1977) The MARID (mica-amphibole-rutile-ilmenite-diopside) suite of xenoliths in kimberlite. Geochim Cosmochim Acta 41:309-310

Eggler DH, Baker DR (1982) Reduced volatiles in the system C-O-H: Implications to mantle melting, fluid formation, and diamond genesis. In: Akimoto S, Manghnani MH (eds) High pressure research in geophysics. Center for Academic Publications Japan, Tokyo, pp 237-250

Frost D, McCammon C (2008) The Redox State of Earth's Mantle. Ann Rev Earth Planet Sci 36:389-420

Griffin WL, Doyle BJ, Ryan CG, Pearson NJ, O'Reilly SY, Davies R, Kivi K, Van Achterbergh E, Natapov LM (1999) Layered mantle lithosphere in the Lac de Gras area, Slave Craton: Composition, structure and origin. J Petrol 40(5):705-727

Grütter HS, Gurney JJ, Menzies AH, Winter F (2004) An updated classification scheme for mantle-derived garnet, for use by diamond explorers. Lithos 77:841-857

Gudmundsson G, Wood BJ (1995) Experimental test of garnet peridotite oxygen barometry. Contrib Mineral Petrol 119:56-67

Harley SL (1984) An experimental study of the partitioning of Fe and Mg between garnet and orthopyroxene. Contrib Mineral Petrol 86:359-373

Harte B (1977) Rock nomenclature with particular relation to deformation and recrystallisation textures in olivine-bearing xenoliths. J Geol 85:279-288

Höfer HE, Brey GP (2007) The iron oxidation state of garnet by electron microprobe: Its determination with the flank method combined with major-element analysis. Am Mineral 92:873-885

Jones AG, Lezaeta P, Ferguson IJ, Chave AD, Evans RL, Garcia X, Spratt J (2003) The electrical structure of the Slave craton. Lithos 71:505-527

Kennedy CS, Kennedy GC (1976) The equilibrium boundary between graphite and diamond. J Geophys Res 81:2467-2470

Luth RW, Virgo D, Boyd FR, Wood BJ (1990) Ferric iron in mantle-derived garnets: Implications for thermobarometry and for the oxidation state of the mantle. Contrib Mineral Petrol 104:56-72

McCammon CA, Griffin WL, Shee SR, O'Neill HSC (2001) Oxidation during metasomatism in ultramafic xenoliths from the Wesselton kimberlite, South Africa: implications for the survival of diamond. Contrib Mineral Petrol 141:287-296

McCammon CA, Kopylova MG (2004) A redox profile of the Slave mantle and oxygen fugacity control in the cratonic mantle. Contrib Mineral Petrol 148:55-68

McDonough WF, Sun SS (1995) The Composition of the Earth. Chem Geol 120:223-253

McGuire A, Dyar M, Nielson J (1991) Metasomatic oxidation of upper mantle periodotite. Contrib Mineral Petrol 109:252-264

Nimis P, Taylor WR (2000) Single clinopyroxene thermobarometry for garnet peridotites. Part I. Calibration and testing of a Cr-in-cpx barometer and an enstatite-in-cpx thermometer. Contrib Mineral Petrol 139:541-554

O'Neill HSC, Wood BJ (1979) An experimental study of Fe-Mg partitioning between garnet and olivine and its calibration as a geothermometer. Contrib Mineral Petrol 70:59-70

O'Neill HSC (1980) An experimental study of Fe-Mg partitioning between garnet and olivine and its calibration as a geothermometer: Corrections. Contrib Mineral Petrol 72:337

Pearson NJ, Griffin WL, Doyle BJ, O'Reilly SY, van Achterbergh E, Kivi K (1999) Xenoliths from the kimberlite pipes of the Lac de Gras area, Slave Craton, Canada. In: Gurney JJ, Gurney JL, Pascoe MD, Richardson SH (eds) Proceedings of the 7th International Kimberlite Conference. Red Roof Design, Cape Town, South Africa, pp 109-116

Pollack HN, Chapman DS (1977) On the regional variation of heat flow, geotherms, and lithospheric thickness. Tectonophysics 38:279-296

Rohrbach A, Ballhaus C, Golla-Schindler U, Ulmer P, Kamenetsky VS, Kuzmin DV (2007) Metal saturation in the upper mantle. Nature 449:456-458

Simon NSC, Irvine GJ, Davies GR, Pearson DG, Carlson RW (2003) The origin of garnet and clinopyroxene in "depleted" Kaapvaal peridotites. Lithos 71:289-322

Stachel T, Viljoen F, Brey GP, Harris JW (1998) Metasomatic processes in lherzolitic and harzburgitic domains of diamondiferous lithospheric mantle: REE in garnets from xenoliths and inclusions in diamonds. Earth Planet Sci Lett 159:1-12

Stachel T, Aulbach S, Brey GP, Harris JW, Leost I, Tappert R, Viljoen KS (2004) The trace element composition of silicate inclusions in diamonds: a review. Lithos 77:1-19

Wood BJ, Bryndzia LT, Johnson KE (1990) Mantle oxidation state and its relationship to tectonic environment and fluid speciation. Science 248:337-345

Woodland A, Kornprobst J, Tabit A (2006) Ferric iron in orogenic lherzolite massifs and controls of oxygen fugacity in the upper mantle. Lithos 89:222-241

Woodland AB, Peltonen P (1999) Ferric iron contents of garnet and clinopyroxene and estimated oxygen fugacities of peridotite xenoliths from the Eastern Finland Kimberlite Province. In: Gurney JJ, Gurney JL, Pascoe MD, Richardson SH (eds)

Proceedings of the 7th International Kimberlite Conference. Red Roof Design, Cape Town, South Africa, pp 904-911

Woodland AB, Koch M (2003) Variation in oxygen fugacity with depth in the upper mantle beneath the Kaapvaal craton, southern Africa. Earth Planet Sci Lett 214:295-310

Chapter 5: Conclusions

There are three key parameters that dictate whether diamond will be a stable phase in the lithospheric mantle – temperature, pressure and oxygen fugacity (fO_2). The temperature, pressure (Kennedy and Kennedy 1976) and fO_2 conditions (e.g. Eggler and Baker 1982) necessary for diamond stability in peridotitic mantle were constrained several decades ago but application of these data to increase our understanding of how diamond forms and is preserved in the Earth's mantle is limited by a lack of constraints on the oxidation state of the lithospheric mantle. Further, it is unclear how mantle metasomatism changes fO_2 and hence affects diamond stability. It is clear from studies of kimberlite-hosted, mantle-derived peridotite xenoliths that the major- and trace-element composition of the lithospheric mantle has been changed from its initially depleted state by transient melt and fluid infiltration events; a feature common to all sections of lithospheric mantle (Frey and Green 1974).

Evidence from inclusions in diamonds from the Kaapvaal and Slave cratons (Stachel et al. 2003; Stachel and Harris 2008) indicates that the lithospheric mantle was originally highly depleted harzburgite or even dunite (Fo_{95} olivine; Table 2.3). Garnets in diamondiferous microxenoliths from the Diavik mine preserve evidence that the depleted mantle was converted from its initially depleted state to more fertile (i.e. lherzolitic) compositions. The preservation of sharp-edged octahedral diamond in these microxenoliths indicates that the metasomatism responsible for this re-enrichment was not diamond destructive. The lack of diamondiferous microxenoliths containing both olivine and orthopyroxene in addition to garnet precludes the calculation of fO_2 for these samples. The redox effect of the metasomatism can be elucidated, however, by comparison to larger xenoliths derived from a similar depth range that contain the full mineralogy of their respective peridotite source.

Trace-element concentrations, especially the rare earth elements, in mantle-derived garnets are sensitive indicators of the depletion/metasomatism history of their host rock

(Hoal, et al. 1994; Stachel, et al. 1998). The C1 chrondrite normalized rare earth element (REE_N) patterns in garnet from the Diavik diamondiferous microxenoliths are mostly sinusoidal (Figure 2.7), indicative of metasomatism by LREE-enriched fluids (Stachel and Harris 1997). This style of metasomatism in the lithospheric mantle beneath Diavik apparently was oxidizing (Section 4.5.4). The deeper portion of the lithospheric mantle, at pressures above the diamond-graphite transition (~4.5 GPa), is still reduced enough that diamond is predicted to be the stable form of carbon (Figure 4.7) whereas the shallower portion is oxidized above the EMOG buffer indicating that carbonate rather than graphite is likely the stable carbon-bearing phase. Garnets with normal REE_N patterns indicate that the deeper portion of the lithospheric mantle at Diavik was in part also metasomatized by melts. The redox effect of the melt metasomatism is somewhat ambiguous but may have been reducing (Section 4.5.4; Figure 4.7).

Mantle xenoliths from the Bultfontein kimberlite also preserve a complex history of metasomatism that had various effects on the formation and preservation of diamond in the lithospheric mantle in the southwest portion of the Kaapvaal craton. Like the samples from Diavik, there are garnets with sinusoidal REE_N patterns but, unlike at Diavik, these samples are the most reduced. If one assumes that the fluids responsible for imparting sinusoidal REE_N patterns in garnets had the same redox effect at both locations (i.e. it was oxidizing as deduced at Diavik), then this would indicate that the mantle beneath the southwestern portion of the Kaapvaal craton was extremely reduced initially. Alternatively, the redox effect of the fluids need not be the same in both locations and fluid metasomatism could have been reducing for the Kaapvaal but oxidizing for the Slave. 'Typical' melt metasomatism, associated with normal REE_N patterns in affected garnets (Section 3.4.2; Figure 3.4), in the Kaapvaal lithospheric mantle, like at Diavik, is ambiguous with respect to the effect that this type of metasomatism had on the oxidation state of the mantle.

The Kaapvaal samples also retain evidence for an additional type of melt metasomatism that is not observed in the central Slave craton – the so-called MARID

metasomatism (Dawson and Smith 1977). Samples affected by this metasomatic event have an increased modal abundance of clinopyroxene; phlogopite is also observed in these samples and garnets with humped or sloped REE_N patterns (Section 3.6; Figure 3.9). The MARID metasomatic event has been temporally linked with the eruption of the Group 2 kimberlites in the southwest Kaapvaal craton (Konzett, et al. 1998) and had a particularly intense effect on the lithospheric mantle in the region (Griffin, et al. 2003, Figure 1.1). The MARID event was unambiguously oxidizing (Figure 3.11) to the point that native carbon either as diamond or graphite may not be stable in mantle lithosphere affected by the MARID event. Consistent with this is the observation that Group 1 kimberlites, erupted from mantle highly affected by the MARID event, generally have lower diamond grades than Group 2 kimberlites (Field, et al. 2008) in the same general area.

From the above examples, it is clear that the infiltration of metasomatic melts and fluids has a significant effect on the prevailing fO_2 of the lithospheric mantle and, therefore, exerts an important control on the formation and preservation of diamond. There is an important limitation in our understanding of how mantle metasomatism changes the fO_2 of the lithospheric mantle: the initial fO_2 of the depleted mantle is as yet unknown. Research into the redox sensitive partitioning behaviour of V (e.g. Canil and Fedortchouk 2000; Canil 2002; Canil 2004; Lee, et al. 2005) has begun to put some constraint on the fO_2 conditions of the peridotite residua of high degree partial melting that later were assembled to form the continental lithospheric mantle. So far, however, these studies have not yet established a firm starting point and hence the magnitude of oxidation or reduction caused by mantle metasomatism cannot be unambiguously constrained.

References

Canil D, Fedortchouk Y (2000) Clinopyroxene-liquid partitioning for vanadium and the oxygen fugacity during formation of cratonic and oceanic mantle lithosphere. J Geophys Res 105:26003-26016

Canil D (2002) Vanadium in peridotites, mantle redox and tectonic environments: Archean to present. Earth Planet Sci Lett 195:75-90

Canil D (2004) Mildly incompatible elements in peridotites and the origins of mantle lithosphere. Lithos 77:375-393

Dawson J, Smith J (1977) The MARID (mica-amphibole-rutile-ilmenite-diopside) suite of xenoliths in kimberlite. Geochim Cosmochim Acta 41:309-310

Eggler DH, Baker DR (1982) Reduced volatiles in the system C-O-H: Implications to mantle melting, fluid formation, and diamond genesis. In: Akimoto S, Manghnani MH (eds) High pressure research in geophysics, Center for Academic Publications Japan, Tokyo, pp 237-250

Field M, Stiefenhofer J, Robey J, Kurszlaukis S (2008) Kimberlite-hosted diamond deposits of southern Africa: A review. Ore Geol Rev 34:33-75

Frey FA, Green DH (1974) The mineralogy, geochemistry and origin of Iherzolite inclusions in Victorian basanites. Geochim Cosmochim Acta 38:1023-1059

Griffin WL, O'Reilly SY, Natapov LM, Ryan CG (2003) The evolution of lithospheric mantle beneath the Kalahari Craton and its margins. Lithos 71:215-241

Hoal KEO, Hoal BG, Erlank AJ, Shimizu N (1994) Metasomatism of the mantle lithosphere recorded by rare earth elements in garnets. Earth Planet Sci Lett 126:303-313

Kennedy CS, Kennedy GC (1976) The equilibrium boundary between graphite and diamond. J Geophys Res 81:2467-2470

Konzett J, Armstrong RA, Sweeney RJ, Compston W (1998) The timing of MARID metasomatism in the Kaapvaal mantle: An ion probe study of zircons from MARID xenoliths. Earth Planet Sci Lett 160:133-145

Lee CTA, Leeman WP, Canil D, Li ZXA (2005) Similar V/Sc systematics in MORB and arc basalts: Implications for the oxygen fugacities of their mantle source regions. J Petrol 46:2313-2336

Stachel T, Harris JW (1997) Diamond precipitation and mantle metasomatism - evidence from the trace element chemistry of silicate inclusions in diamonds from Akwatia, Ghana. Contrib Mineral Petrol 129:143-154

Stachel T, Viljoen F, Brey GP, Harris JW (1998) Metasomatic processes in lherzolitic and harzburgitic domains of diamondiferous lithospheric mantle: REE in garnets from xenoliths and inclusions in diamonds. Earth Planet Sci Lett 159:1-12

Stachel T, Harris JW, Tappert R, Brey GP (2003) Peridotitic diamonds from the Slave and the Kaapvaal cratons - similarities and differences based on a preliminary data set. Lithos 71:489-503

Stachel T, Harris J (2008) The origin of cratonic diamonds—Constraints from mineral inclusions. Ore Geol Rev 34:5-32

Appendix A: Modifications to the Flank Method[1]

The flank method protocol used to measure Fe^{3+} concentrations in mantle-derived garnets follows the pioneering work of Höfer et al. (1994) as detailed by Höfer and Brey (2007). From this base, the method has been modified to improve the precision and accuracy for the analysis of mantle-derived pyropic garnets with low ΣFe and Fe^{3+} concentrations. The modifications include: 1) increasing the number of analytical points and decreasing the dwell time per spot; 2) operating the electron probe with a beam current of 150-160 nA and an accelerating voltage of 20 kV; 3) using garnets standards compositionally similar to the unknowns to establish calibration curves (e.g. Figure 16 of Höfer and Brey 2007).

We have increased the number of analytical points to a 10 × 10 grid with a spacing of 2-3 μm between each spot. The spacing is set large enough to avoid overlapping activation volumes and gives an effective spatial resolution of 20×20 μm or 30×30 μm. Flank method analyses are conducted with spectrometers in a fixed position to avoid errors introduced by minor irreproducibility in the mechanical positioning of the spectrometer crystal. In this modified protocol, measurements are first made on the Lβ flank position for a grid on all garnets and then the spectrometer is driven to the Lα flank position and the grid sequence is repeated. Instrumental drift is monitored by repeat analysis of one of the standard garnets.

The data set of 100 points, counted for 60 seconds each on Lβ and Lα (total analysis time of ~3.5 hours per sample), has a Gaussian distribution and, therefore, allows the use of simple statistics to describe the population. Thus, the Fe Lβ/Lα ratio of the garnet is taken as the mean of the analyses and the error in $Fe^{3+}/\Sigma Fe$ is estimated by propagating the standard error of the mean. Repeat analyses of a single garnet fragment over a period of several months had a reproducibility in $Fe^{3+}/\Sigma Fe$ of ± 0.008.

Operating with high beam current increases the intensity (count rate) of the weak

1 A portion of Appendix A is published as an appendix in Creighton S, Stachel T, Matveev S, Höfer HE, McCammon C, Luth RW (2009) Oxidation of the Kaapvaal lithospheric mantle driven by metasomatism. Contributions to Mineralogy and Petrology 157:491-504

L-line X-Ray emissions which is important for measuring samples with low total (< 10 wt% FeO_T) and ferric iron (< 1.0 wt.% Fe_2O_3) concentrations. The increased count rate improves the sensitivity of the flank method making it applicable to mantle-derived pyropic garnets; however, the increased X-Ray intensity of major-element emissions (e.g. Mg, Si) increases "dead time" of gas-flow proportional counters making simultaneous quantitative analysis using 1st order Kα emissions unreliable. With proper calibration, it may, however, be possible to use 2nd order lines for quantitative analysis.

Höfer and Brey (2007, their Figure 14) show that in the region of key interest for mantle garnets (<10 wt.% FeO_T, and $Fe^{3+}/\Sigma Fe < 0.15$) there is considerable scatter and disagreement between the flank method and Mössbauer spectroscopy for natural samples. One potential source of the observed discrepancy may be the sensitivity of the flank method to crystallographic site distortions due to cation substitution (Höfer 2002). By measuring fragments of natural homogeneous garnet crystals, similar in major-element composition to the unknowns (especially in Ca concentration), using a Mössbauer 'milliprobe' with a young high specific activity point source (see McCammon 1994; with experimental setup as in McCammon and Kopylova 2004) we have been able to improve the agreement between the two techniques (Figure 3.2). The calibration curves necessary for calculating the $Fe^{3+}/\Sigma Fe$ of unknown garnets (e.g. Figure 16 of Höfer and Brey, 2007) were constructed using the same grains measured with Mössbauer spectroscopy, eliminating any error that may be introduced by slight variations in ferric iron concentrations in the standard garnets. Because of minor variations in spectrometer reproducibility, it is important that the calibration curves be derived for each analytical session. Using these modifications, the flank method can now be applied to accurately and precisely measure Fe^{3+}/Fe^{2+} of mantle-derived garnets.

Another potential application of the high spatial resolution of the flank method is the ability to measure variations in Fe^{3+} in zoned garnets. Garnets in the present study were found to be unzoned, so this ability was not needed. But to illustrate the potential, we were

able to measure ferric iron zoning in a large (~3.7 cm diameter) garnet in xenolith PHN 1611 from Thaba Putsoa, Lesotho (Figure A.1) using the flank method. The ferric iron zoning in this sample indicates an increase in $\Delta \log fO_2$ with the metasomatic enrichment apparent in this sample.

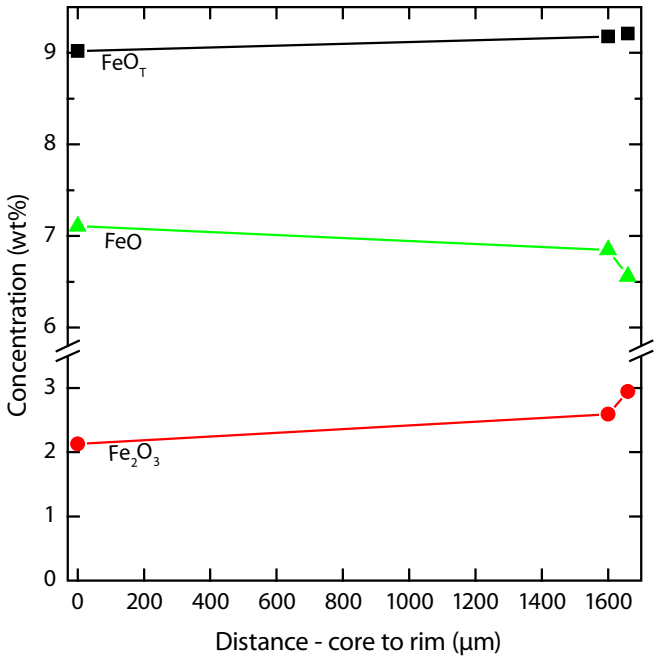

Figure A.1: Iron zoning in a large (~3.4 cm diameter) garnet from xenolith PHN1611. Total iron reported as FeO_T shows a slight increase from core to rim. Ferric iron measured with the flank method shows a dramatic increase from 2.60 to 2.94 wt% Fe_2O_3 within 60 µm from the garnet rim. The 1σ error bars are smaller than the symbols used.

Methodology for flank method measurements

The following gives a practical outline of how to use the flank method on the JEOL 8900 superprobe at the University of Alberta.

Spectrometer Setup

Spectrometers 2 and 4 both have TAP crystals that are suitable for flank method measurements but the best results so far are from spectrometer 4. The measurement positions are determined by qualitative scans from 650 to 750 eV on the Harvard almandine and

synthetic andradite standards. The proper location of the flank measurement positions are then located at the extrema in the difference spectrum i.e. andradite – almandine (Figure A2). The maximum located near the FeLα emission peak (between 705 and 710 eV) is the correct position for the "FeLα" flank method measurement, the minimum in the difference spectrum near the FeLβ peak (between 715 and 720 eV) is the measuring position for the flank method "FeLβ". The pulse height analyzer (PHA or SCA) settings for the spectrometer should be optimized using the FeLα flank position on the andradite standard. A narrow window will avoid overlaps from higher order X-ray emission lines leading to a smaller error in the measured $Fe^{3+}/\Sigma Fe$.

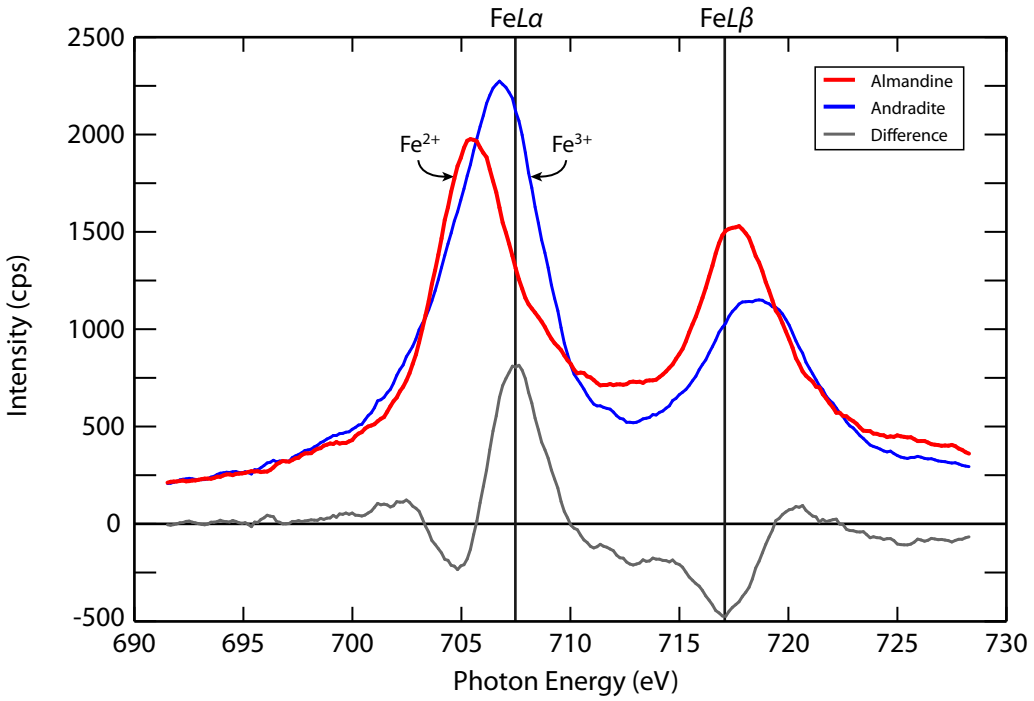

Figure A.2: FeL emmission spectra of almandine and andradite. The difference spectrum is used for determining where flank method measurements should be made (indicated by vertical lines).

Flank measurements

Because of limitations in the JEOL software, it is necessary to use proxy elements in the measurement condition file – Ar for FeLα and Br for FeLβ. For peak positions, use the flank positions determined from the difference spectrum, set the counting time for 90 seconds with no background and use differential mode. Use the narrow window settings determined from the andradite standard from above.

Use the normal routine for setting analytical grids of 9×9 or 10×10, with a minimum of 1.5 μm spacing between points, firstly on the pyrope standards DG3 and DG7. Place grids[2] on the unknowns as desired returning to DG7 after two unknowns; the repeat analysis of DG7 will be useful for correcting any instrumental drift. Use the file manager to duplicate the file containing the preset analytical spots for the FeLα measurements. Using the program for serial analysis, set up the measurement routine to start with FeLβ and then to return to the same spots for FeLα.

Data reduction

Run a summary with net intensities of Ar and Br and a summary of the beam current values of each analytical spot. Insert these data into an Excel® spreadsheet. Normalize each result by multiplying the net intensity by the current to get the count rate. Be aware that the JEOL software reports the net intensity in counts per second per microampere (cps/μA) and the beam current is reported in nA. From the normalized count rates, calculate the FeLβ/FeLα; these ratios will be used to calculate the $Fe^{3+}/\Sigma Fe$ of the garnet. Calculate the mean, standard deviation and 95% confidence interval of the mean for each standard and unknown using the *AVERAGE()*, *STDEV()*, and *CONFIDENCE()* functions in Excel. Plot the FeLβ/FeLα vs. Fe^{2+} for DG3 and DG7 and calculate the linear regression (see Figure 16a of Höfer and Brey 2007). Use the equation of the linear regression to calculate the Δ ratio (see Figure 16b of Höfer and Brey 2007) for all standards and unknowns. This

2 A grid is the simplest method for setting numerous analytical spots but there is no reason why the spots could not be set in any random arrangement e.g. along the circumference of a zoned garnet.

is done by substituting ΣFe for Fe^{2+} in the linear equation above. Plot Fe^{3+} vs. Δ ratio for DG3 and DG7 and regress the data. If the regression does not pass reasonably close to the origin, the standardization is off and the data are useless. Calculate the Fe^{3+} of the unknown garnets using the slope of the second regression line. From this it is trivial to calculate $Fe^{3+}/\Sigma Fe$ and Fe_2O_3.

The 2σ error is calculated by propagating the 95% confidence interval of the mean through the Fe^{3+} calculations. Add the 95% confidence interval to the Δ ratio and multiple by the slope of the second regression line from above. This is maximum Fe^{3+} for these data; the error in Fe^{3+} is the difference between the Fe^{3+} and the maximum Fe^{3+}. Calculating the error in $Fe^{3+}/\Sigma Fe$ is done by dividing the maximum Fe^{3+} by ΣFe and subtracting the actual $Fe^{3+}/\Sigma Fe$ determined for the sample.

References

Höfer, H.E. and Brey, G.P., (2007) The iron oxidation state of garnet by electron microprobe: Its determination with the flank method combined with major-element analysis. Am Mineral, 92: 873-885.

McCammon CA., (1994) A Mössbauer milliprobe: Practical considerations. Hyper Inter 92:1235-1239

McCammon, C.A. and Kopylova, M.G., (2004) A redox profile of the Slave mantle and oxygen fugacity control in the cratonic mantle. Contrib Mineral Petrol, 148: 55-68.

Appendix B: Wet chemical determination of ferrous iron in small (<50 mg) samples

The technique for determining is based on the work of Yokoyama and Nakamura (2002) and this appendix should be used in conjunction with that paper as the primary reference. The technique outlined by Yokoyama and Nakamura (2002) is not unique to their work but it does take advantage of some more recent technological advances especially that of an automated burette. The method is based on the reactions:

$$Fe^{2+}_{sample} + V^{5+}_{excess} = Fe^{3+} + V^{4+} \quad \text{(B1)}$$

$$Fe^{2+}_{excess} + V^{5+} = Fe^{3+} + V^{4+} \quad \text{(B2)}$$

$$3Fe^{2+} + Cr^{6+} = 3Fe^{3+} + Cr^{3+} \quad \text{(B3)}$$

Reaction B1 proceeds to the right as the ferrous iron is liberated from the sample during digestion under strongly acidic conditions. The amount of excess V^{5+} reduced to V^{4+} is the same as the amount of Fe^{2+}in the sample and because V^{4+} is resistant to oxidation, it does not back-react to V^{5+} during the digestion and subsequent analysis. The remaining V^{5+} in the digestion vessel is reacted to V^{4+} by the addition of a known amount of excess Fe^{2+} (Equation B2). The amount of Fe^{2+} liberated from the sample can be determined by measuring the excess V^{5+} by titrating the excess Fe^{2+} with Cr^{6+} (Equation B3). The equation for calculating wt.% FeO in the sample is:

$$FeO(wt\%) = \frac{(V_{Cr} \times C_{Cr} + W_V \times C_V - W_{Fe} \times C_{Fe})}{W_{sample}} \times 71.8444 \times 100 \quad \text{(B4)}$$

Where V_{Cr} is the volume of Cr^{6+} titrant and W_x is the weight of the Fe^{2+} and V^{5+} solutions and C_x is the concentration of the solution.

The following text is intended to complement Yokoyama and Nakamura (2002) as comments and advice on implementation at the University of Alberta with respect to specific sections of their paper.

§2.1.3: The actual concentration can be determined by titration of solid ammonium iron(II) sulfate hexahydrate using the following procedure and equation:

1. weigh ~0.1 g of solid $Fe(NH_4)_2(SO_4)_2 \cdot 6H_2O$ into a Nalgene beaker
2. add in 5 ml of phosphoric/sulfuric acid mix with a syringe
3. dilute to 40 ml with water
4. pour the solution into a pyrex beaker
5. add 1 drop of indicator and the magnetic stirrer rod
6. titrate with Cr^{6+} until a permanent faint purple color

$$C_{Cr} = \left(\frac{W_{Fe}}{391.971} \cdot 10^3 \right) \times \frac{1}{V_{Cr}} \tag{B5}$$

§2.1.6: Do *not* mix these acids without a water bath and consider mixing in the polyethene dropper bottle.

§2.1.7: The initial concentration of Fe^{2+} in this solution **must** be measured at the beginning of each titration series, noting the time. The concentration decreases due to atmospheric oxidation of Fe^{2+} by the equation: $Fe^{2+}[t] = Fe^{2+}[t_0] - 0.00005 \times t$; where t is time in hours and concentration is in mmol/g. The concentration can be determined by the following procedure and equation:

1. weigh ~0.7 g of solution in a Nalgene beaker
2. add in 5 ml of phosphoric/sulfuric acid mix with a syringe
3. dilute to 40 ml with water
4. pour the solution into a pyrex beaker
5. add 1 drop of indicator and the magnetic stirrer rod
6. titrate with Cr^{6+} until a permanent faint purple color

$$C_{Fe} = \frac{V_{Cr} \times C_{Cr}}{W_{Fe}} \tag{B6}$$

§2.1.8: The $NaVO_3$ is difficult to dissolve, use a magnetic stir rod. The concentration of V^{5+} in this solution is robust for long periods of time although it may become discoloured after sitting for a few weeks. The concentration is determined using the following procedure and equation:

1. weigh ~0.7 g of V^{5+} solution into a Nalgene beaker
2. add ~1.4 g of Fe^{2+} solution
3. add in 5 ml of phosphoric/sulfuric acid mix with a syringe
4. dilute to 40 ml with water
5. pour the solution into a pyrex beaker
6. add 1 drop of indicator and the magnetic stirrer rod
7. titrate with Cr^{6+} until a permanent faint purple color

$$C_V = \frac{W_{Fe} \times C_{Fe} - V_{Cr} \times C_{Cr}}{W_V} \tag{B7}$$

§2.1.10: We use a Metrohm 775 Dosimat automated burette with a 50 ml capacity. The burette is not accurate immediately following the filling procedure therefore after the automated fill is complete dispense and discard the first 5 ml. It is likewise advisable to not allow the burette to refill during a titration (most titrations require less than 5 ml of titrant).

§2.2.1: Because of the high Mg and Ca concentration in pyropic garnets, dissolution in HF-H_2SO_4 is difficult. The formation of CaF_2 and MgF_2 slimes often coat the undissolved portion of the garnet. I recommend fine grinding of the sample under ethanol (to minimize oxidation during grinding) and occasionally breaking up the slime by placing the sealed dissolution vessel in an ultrasonic bath for a few minutes during the dissolution process. Adding more HF-H_2SO_4 is also advisable. The recommended procedure follows.

1. weigh ~20 mg of sample into a teflon savillex vial
2. weigh ~0.7 g of V^{5+} solution into the teflon vial with the sample
3. using a syringe, add 4-5 ml of acid for rock powders, 8-10 ml for garnets
4. cap tightly and cook on a hotplate overnight at ~150-220°C
5. weigh ~1 g of Fe^{2+} solution in a teflon or polyethylene beaker
6. remove the sample vial from the hotplate
7. add 5 ml of phosphoric/sulfuric acid mix into the teflon beaker with a syringe
8. dilute with 40-50 (80-100) ml of boric acid solution (10 ml per 1.5 ml of HF-H_2SO_4 mix)
9. pour the entire contents into a pyrex beaker; wash the teflon beaker into the pyrex beaker with a few ml of water
10. manually agitate the sample and immediately pour the contents of the vial into the beaker, washing the contents into the pyrex beaker with a few ml of water
11. add 1-2 drops of indicator and the magnetic stirrer rod
12. titrate to the end-point with Cr^{6+}

§3.4: Subtract 0.005 ml of Cr^{6+} for each drop of indicator added.

This slightly modified version of the wet chemical procedure has been successfully applied to measuring $Fe^{3+}/\Sigma Fe$ in a large garnet megacryst from Diavik (sample no. UA5). The ferric iron concentration of this garnet has also been measured using Mössbauer milliprobe and the flank method (Figure B1). The results of all these measurements all agree within their respective 1σ errors[1] indicating that the wet chemical method as described in Yokoyama and Nakamura (2002) can be successfully applied to very small samples and verifying the accuracy of the flank method.

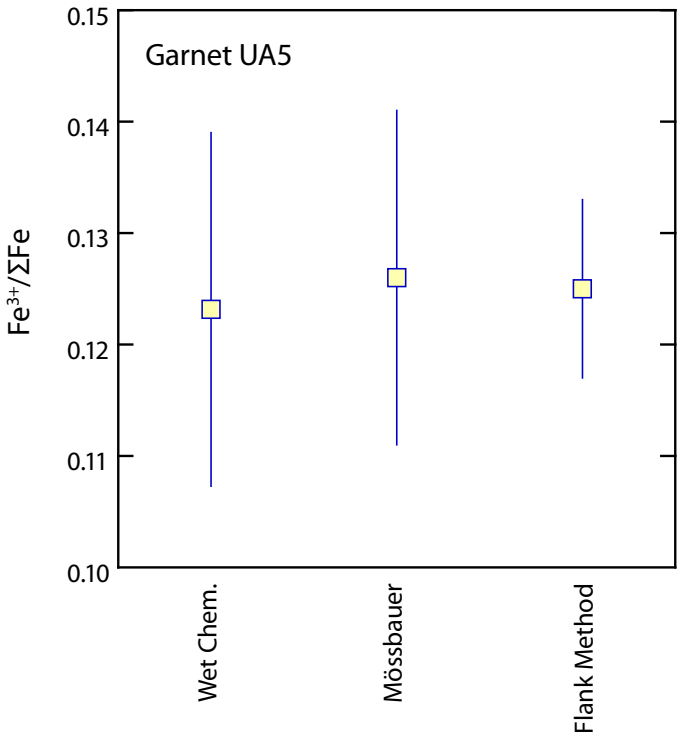

Figure B.1: Comparison of $Fe^{3+}/\Sigma Fe$ measured for one garnet using wet chemistry, Mössbauer milliprobe and the flank method (Appendix A). The vertical bars indicate the 1σ error of the respective methods used.

1 The 1σ error determined for $Fe^{3+}/\Sigma Fe$ of this garnet using the wet chemical method is the standard deviation of four repeat analyses.

Appendix C: Xenolith Petrography

The following tables summarize petrographic observations of samples investigated for the preceding chapters. Some of the samples listed are were not included because they did not contain garnet or were otherwise deemed superfluous (e.g. websterite samples).

Sample	Sample suite	Mineralogy					Texture				Comments
		olivine	opx	cpx	garnet	spinel	coarse	gb	ppc	mppc	
Bo-01	Boshoff	x	x	x	x		x				+ phlogopite
Bo-02	Boshoff	x	x	x	x		x				
Bo-03	Boshoff	x	x	x	x		x				+ phlogopite
Bo-04	Boshoff	x	x	x	x	x	x				
Bo-05	Boshoff	x	x	x	x		x				+ phlogopite
Bo-06	Boshoff	x	x	x						x	all garnets are altered
Bo-07	Boshoff	x	x	x	x		x				+ phlogopite
Bo-08	Boshoff	x	x	x	x					x	+ secondary calcite
Bo-09	Boshoff	x	x	x		x				x	
Bo-10	Boshoff	x	x	x	x			x			
Bo-11	Boshoff	x	x	x		x		x			+ phlogopite
Bo-12	Boshoff	x	x	x	x			x			
Bo-13	Boshoff	x	x		x					x	
Bo-14	Boshoff	x	x	x	x	x	x				+ phlogopite
Bo-15	Boshoff	x	x			x	x				
Bo-16	Boshoff	x	x	x		x		x			+ phlogopite
Bo-17	Boshoff	x	x	x		x		x			
Bo-18	Boshoff	x	x	x	x				x		
Bo-19	Boshoff	x	x	x	x	x		x			
Bo-20	Boshoff	x	x		x			x			
Bo-21	Boshoff	x	x		x			x			
Bo-22	Boshoff	x	x				x				
Bo-23	Boshoff	x	x				x				
Bo-24	Boshoff	x	x	x					x		
Bo-25	Boshoff	x	x	x		x		x			
Bo-26	Boshoff	x	x	x	x			x			secondary phlogopite
Bo-27	Boshoff	x	x	x	x				x		
Bo-28	Boshoff	x	x	x		x		x			spinel in symplectite with clinopyroxene
Bo-29	Boshoff	x	x	x		x		x			
Bo-30	Boshoff	x	x	x	x					x	

Sample	Sample suite	Mineralogy					Texture				Comments
		olivine	opx	cpx	garnet	spinel	coarse	gb	ppc	mppc	
A154-01	Diavik	x	x	x	x			x			calcite vein
A154-06	Diavik	x	x	x	x				x		
A154-09A	Diavik	x	x	x	x					x	
A154-09CR	Diavik	x	x	x	x			x			strongly altered
A154-10	Diavik	x	x		x					x	
A154-11	Diavik	x		x	x					x	
A154-17	Diavik	x			x			?			heavily altered
MX001	Diavik	x	x	x	x					x	
MX013	Diavik		x	x	x		x				websterite
MX014	Diavik	x	x	x	x		x				olivine websterite
MX029	Diavik	x	x	x	x			x			too thin
MX031	Diavik	x	x		x			x			
MX032	Diavik	x	x	x	x				x		
MX038	Diavik		x	x	x		x				exsolution in px -- websterite
MX039	Diavik	x	x	x	x		x				websterite/ highly altered
MX044	Diavik	x	x	x	x				x		
MX056	Diavik	x	x	x	x			x			exsolution in px -- websterite, primary phlogopite
MX058	Diavik	x	x	x		x		x			
MX060	Diavik	x	x	x	x		x				exsolution in px -- websterite
MX088	Diavik	x	x	x	x		x				calcite veins
MX093	Diavik			x							clinopyroxene-ilmenite megacryst
MX101	Diavik	x	x	x	x		x				websterite -- exsolutions in px
MX104	Diavik	x	x	x	x			x			altered
MX117	Diavik	x	x	x	x				x		highly altered -- zoning in opx
MX118	Diavik	x	x		x		x				too thin
MX123	Diavik	x	x	x	x		x				websterite
MX131	Diavik	x	x	x	x					x	
MX135	Diavik		x	x	x			x			websterite
MX142	Diavik		x								orthopyroxenite
MX144	Diavik	x	x	x	x			x			kimberlite infiltration
MX158	Diavik	x	x	x	x				x		
MX160	Diavik	x	x	x		x		x			
MX162	Diavik	x	x	x	x				x		
MX165	Diavik	x	x	x	x				x		kimberlite infiltration

Sample	Sample suite	Mineralogy					Texture				Comments
		olivine	opx	cpx	garnet	spinel	coarse	gb	ppc	mppc	
MX5000	Diavik	x	x	x	x			x			
MX5001	Diavik	x	x	x	x			x			
MX5002	Diavik	x	x			x		x			spinel in symplectite
MX5003	Diavik	x	x	x	x			x			kimberlite infiltration
MX5004	Diavik	x	x	x	x				x		
MX5005	Diavik	x	x	x	x	x		x			websterite -- spinel in symplectites
MX5006	Diavik	x	x	x	x				x		kimberlite infiltration
MX5007	Diavik	x	x		x	x		x			spinel in symplectite with clinopyroxene
MX5008	Diavik	x	x	x	x					x	
MX5009	Diavik	x	x	x	x					x	kimberlite infiltration
MX5010	Diavik	x	x		x			x			kimberlite infiltration
MX5011	Diavik	x	x	x	x		x				kimberlite infiltration
MX5012	Diavik	x	x	x	x				x		kimberlite infiltration
MX5014	Diavik	x	x	x	x		x				
MX5016	Diavik	x	x	x	x				x		
MX5017	Diavik	x	x	x	x		x				websterite -- exsolution in px